Graphene Oxide and Graphene in Membrane Applications: A Molecular Dynamics Simulation Study

by

Abhijit Gogoi
Roll No. 156103020

Submitted in partial fulfillment of the requirements for the degree of
Doctor of Philosophy
under the supervision of

Dr. Pranab Kumar Mondal and Dr. K. Anki Reddy

Department of Mechanical Engineering
Indian Institute of Technology Guwahati
India
781039
December, 2020

Abstract

The applicability of graphene oxide (GO) and graphene for separation and purification applications is investigated using non-equilibrium molecular dynamics (MD) simulations. The effect of internal structure of the layered GO membrane on its performance as a forward osmosis (FO) membrane for sea water desalination and dehydration of acetic acid is studied. For this layered GO membrane with different pore offset distance (**W**) and interlayer distance (**H**) are constructed. The pore offset distance (**W**) is a measure of the lateral dimension of the constituting GO nanosheets of the layered GO membranes. GO membranes composed of nanosheets of smaller lateral dimensions found to have higher water permeance than GO membranes composed of nanosheets of larger lateral dimensions. On the other hand salt rejection of layered GO membrane increases with the increase in size of the constituting GO nanosheets. One of the reason for this could be the blockage of permeate pathways through the layered GO membrane due to the movement of the GO nanosheets. This becomes more prominent with increasing **W**. Increasing **W** also leads to increase in distance traversed by the permeating water molecule through the layered GO membrane. The ion permeability is also affected by the parameter **W**, type and magnitude of charge the ion possesses and the intensity of interaction between water molecules and the ions. The performance of layered GO membrane is also dependent on its interlayer distance. The water permeance increases and the draw solute rejection decreases as the interlayer spacing between the GO layers increases to a optimum value, after that, with further increase in the interlayer spacing the water permeance decreases and the salt rejection of the membrane increases. With the increase in draw solution concentration the water permeance through the membrane increases but the corresponding variation in the draw solute rejection is very less (< 2.0 %).

The presence of the cations can also significantly influence the performance of layered GO membranes both in FO and reverse osmosis (RO) processes. For the same interlayer spacings, the cation intercalated layered GO membranes have higher water flux as compared to corresponding pristine layered GO membranes. In the presence of the cations, the water molecules inside the interlayer gallery get more compactly packed. The presence of the cations also increases the stability of the hydrogen bond network among the water molecules inside the membrane. This can be attributed to the slow water reorientation dynamics inside the interlayer gallery in the presence of the cations. The synergistic effect of all these changes is that the water permeability through cation intercalated layered GO membranes is higher as compared to corresponding pristine layered GO membranes. On the other hand, the intercalation of the cations (K^+, Mg^{2+}) lead to higher rejection of Na^+ ions whereas the rejection of Cl^- ions slightly decreases.

In this present study, the electro-osmotic flow behaviour through a graphene nanochannel with surfaces having striped charge distribution are also discussed in detail using non-equilibrium molecular dynamics simulations. The velocity of the water molecules and the water permeance through the nanochannel increases with the increase in surface charge density from 0.005 Cm^{-2} to 0.025 Cm^{-2}. With further increase in the surface charge density beyond 0.025 Cm^{-2}, the velocity of the water

molecules and the water permeance through the nanochannel gradually decreases. At a lower value of surface charge density, the interaction between the wall of the nanochannel and the water molecules is dominated by the van der Waals interaction. On the other hand, at a higher surface charge density the interaction between the wall surface and the water molecules is dominated by the electrostatic interaction. These interactions along with the density distribution of the ion species dictate the charge density profile along the nanochannel.

Declaration

I, Sri Abhijit Gogoi, would like to declare that the thesis titled "Graphene Oxide and Graphene in Membrane Applications: A Molecular Dynamics Simulation Study" submitted to "Indian Institute of Technology Guwahati" for the degree of "Doctor of Philosophy " is a work of pure authenticity carried out under the close supervision of Dr. Pranab Kumar Mondal and Dr. K. Anki Reddy. To the best of my knowledge, the content of this thesis have not been submitted to any other institute for awarding any degree. The content of this thesis are free from any act of plagiarism. The investigations and observations reported in this thesis are carried out in the Department of Mechanical Engineering, Indian Institute of Technology Guwahati, during the period July 2015 to May 2020.

Signed:

Abhijit Gogoi
Department of Mechanical Engineering
Indian Institute of Technology Guwahati
Guwahati-781039, Assam, India.

Date:

Certificate

This is to certify that the thesis titled "Graphene Oxide and Graphene in Membrane Applications: A Molecular Dynamics Simulation Study" submitted by Sri Abhijit Gogoi to Indian Institute of Technology Guwahati for the award of the degree of "Doctor of Philosophy" is a record of original research work carried out by him under my close supervision and guidance. The content of this thesis, in part or in full, have not been submitted previously to any institute for awarding any degree or diploma. The thesis has fulfilled all the criteria as per the guidelines of the institute and has reached the standard needed for submission.

Signed:

Supervisor: Dr. Pranab Kumar Mondal
Department of Mechanical Engineering
Indian Institute of Technology Guwahati
Guwahati-781039, Assam, India

Date:

Signed:

Co-Supervisor: Dr. K. Anki Reddy
Department of Chemical Engineering
Indian Institute of Technology Guwahati
Guwahati-781039, Assam, India

Date:

Acknowledgements

My sincere gratitude to my supervisors, Dr. Pranab Kumar Mondal and Dr. K. Anki Reddy for their continuous support, motivation and guidance throughout my PhD thesis work. I am also grateful to Dr. Kalyan Raidongia from the Department of Chemistry and Dr. S. Senthilmurugan from the Department of Chemical Engineering for their valuable insights and suggestions on graphene oxide membrane and forward osmosis process. I am thankful to the respected members of the Doctoral Committee for their valuable suggestions on the improvement of my PhD dissertation work. I sincerely thank to all our group members and my lab-mates for their valuable suggestions and support throughout my PhD journey. Finally, I am grateful to all my family members for their unconditional love and support which keep me moving.

भारतीय प्रौद्योगिकी संस्थान गुवाहाटी
Indian Institute of Technology Guwahati

Nomenclature

σ	Surface charge density
$\boldsymbol{N_{Na}}$	Number of Na^+ ions permeating through the nanochannel in an electro-osmotic flow
$\boldsymbol{N_w}$	Number of water molecules permeating through the nanochannel in an electro-osmotic flow
$\mathbf{C_e}$	Dipole relaxation function
$\mathbf{C(t)}$	H bond autocorrelation function
$\boldsymbol{N_d}$	Number of water molecules in the draw solution
$\boldsymbol{N_m}$	Number of water molecules inside the layered GO membrane
$\mathbf{C_C(t)}$	Continuous H bond autocorrelation function
$\mathbf{C_I(t)}$	Intermittent H bond autocorrelation function
C	Draw solution concentration
D	Pore width of layered GO membrane
E	External electric field applied in an electro-osmotic flow
H	Interlayer distance of layered GO membrane
Lx	X dimension of a rectangular nanochannel
Ly	Y dimension of a rectangular nanochannel

Lz Z dimension of a rectangular nanochannel

W Pore offset distance of layered GO membrane

Contents

1 Introduction **1**

2 Simulation Methodology **15**

2.1 Essence of Computational Modeling 15

2.2 Molecular Dynamics 16

2.2.1 Force Field 17

2.2.2 Integration of Equation of Motion 20

2.2.3 Boundary Conditions 21

2.2.4 Validation of the Force Field 22

3 Literature Review and Objectives **25**

3.1 Literature Review 25

3.1.1 Graphene Based Nano Materials for Membrane Applications . 26

3.1.2 Forward Osmosis (FO) 33

3.1.3 Dehydration of Acetic Acid 34

3.1.4 Electro-Osmotic Flow (EOF) 36

3.2 Objectives 41

4 Multilayer Graphene Oxide Membrane in Forward Osmosis: Molecular Insights **43**

4.1 Introduction 43

4.2 Methodology 44

4.2.1 Model Construction 44

4.2.2 Simulation System 45
4.2.3 Simulation Methodology 47
4.3 Results and Discussion 49
4.3.1 Water Dynamics 49
4.3.2 Ion Dynamics 55
4.3.3 Membrane Performance 59
4.4 Conclusions 64

5 Dehydration of Acetic Acid using Layered Graphene Oxide (GO) Membrane through Forward Osmosis (FO) Process: A Molecular Dynamics Study 67
5.1 Introduction 67
5.2 Methodology 68
5.3 Results and Discussion 73
5.4 Conclusions 81

6 Influence of the Presence of the Cations on the Water and Salt Dynamics Inside Layered Graphene Oxide (GO) Membranes 83
6.1 Introduction 83
6.2 Methodology 86
6.3 Results and Discussion 89
6.4 Conclusions 101

7 Electroosmotic Flow through Nanochannel with Patterned Surface Charge Distribution: A Molecular Dynamics Study 103
7.1 Introduction 103
7.2 Methodology 104
7.3 Results and Discussion 107
7.4 Conclusions 123

8 Conclusions and Future Scope 125
8.1 Conclusions 125

8.2 Scope for Future Investigations 128

Bibliography **131**

List of Publications **163**

भारतीय प्रौद्योगिकी संस्थान गुवाहाटी
Indian Institute of Technology Guwahati

List of Figures

1-1 GO dispersed in water (3 $mgmL^{-1}$) [1]. 8

1-2 Schematic Diagram of the RO Process [2]. 11

1-3 Schematic of the FO process [3]. 12

1-4 An illustration of forward osmosis desalination [3]. 13

2-1 Periodic Boundary Conditions; illustration in two dimension. The simulation box is highlighted at the center, and is surrounded by periodic images of itself [4]. 21

2-2 (a) Distance between two GO nanosheets and (b) number of hydrogen bonds between two GO nanosheets during the aggregation process obtained through our force field parameters. 22

2-3 Distance between two GO nanosheets and number of hydrogen bonds between two GO nanosheets during the aggregation process as reported by Tang *et al.* [5]. 23

4-1 The three membrane configurations (a) Configuration-1 (b) Configuration-2 (c) Configuration-3. The green color is for hydrogen atoms, the red color is for oxygen atoms and the cyan color is for carbon atoms. . . . 46

4-2 (a) Hydrated membrane (configuration-3) (b) Feed solution (c) Draw solution (d) Simulation setup. The green color is for hydrogen atoms, the red color is for oxygen atoms, the cyan color is for carbon atoms, the blue color is for Cl^- ions, the magenta color is for Na^+ ions, the orange color is for Mg^{2+} ions, the black color is for Al^{3+} ions, the yellow color is for sulfur atoms. 47

4-3 Variation of the number of water molecules in the draw solution box (N_d) with time. 49

4-4 (a) Trajectory of the water molecule inside the layered GO membrane of configuration-1. (b) The number of water molecules in the hydration shell of water at various positions while permeating through the membrane. The permeated water molecule is shown in violet color. Red color is for oxygen atoms, green color is for hydrogen atoms and cyan color is for carbon atoms. 50

4-5 (a)Trajectory of the water molecule inside the layered GO membrane of configuration-2. (b) The number of water molecules in the hydration shell of water at various positions while permeating through the membrane. The permeated water molecule is shown in violet color. Red color is for oxygen atoms, green color is for hydrogen atoms and cyan color is for carbon atoms. 50

4-6 (a) Trajectory of the water molecule inside the layered GO membrane of configuration-3. (b) The number of water molecules in the hydration shell of water at various positions while permeating through the membrane. The permeated water molecule is shown in violet color. Red color is for oxygen atoms, green color is for hydrogen atoms and cyan color is for carbon atoms. 51

4-7 Radial distribution function between oxygen atoms of the functional groups present in GO and oxygen atoms of water. O1 is oxygen atom of hydroxyl group (-OH), O2 is the oxygen atom of epoxy group (-O-), O3 is the oxygen atom of the carboxyl group which is bonded to only C atom (-C=O), O4 is the oxygen atom of carboxyl group which is bonded to H and C atom (C-O-H) and OW is the oxygen atom of water. 51

4-8 Density of water molecules along the Z direction. (a) configuration-1 (b) configuration-2 (c) configuration-3. The positions of the two membranes are shown by two pair of dotted green lines. 52

4-9 Distribution of distance traversed (a) configuration-1 (b) configuration-2 (c) configuration-3, residence time (d) configuration-1 (e) configuration-2 (f) configuration-3 and velocity (g) configuration-1 (h) configuration-2 (i) configuration-3, of the water molecules while permeating through the layered GO membranes. 55

4-10 Density of ions along the Z direction. (a) configuration-1 (b) configuration-2 (c) configuration-3. The positions of the two membranes are shown by two pair of dotted green lines. Please note that simulation time for configuration-1 and configuration-2 is 25 ns, while it is 64 ns for configuration-3. 56

4-11 (a) Trajectory of Mg^{2+} ion inside the layered GO membrane of configuration-3. (b) Number of water molecules in the hydration shell of Mg^{2+} ion at various locations while permeating through the membrane. Red color is for oxygen atoms, green color is for hydrogen atoms, cyan color is for carbon atoms and mauve color is for Mg^{2+} ion. 56

4-12 (a) Trajectory of Na^{+} ion inside the layered GO membrane of configuration-3. (b) Number of water molecules in the hydration shell of Na^{+} ion at various locations while permeating through the membrane. Red color is for oxygen atoms, green color is for hydrogen atoms, cyan color is for carbon atoms and yellow color is for Na^{+} ion. 57

4-13 (a) Trajectory of Cl^{-} ion inside the layered GO membrane of configuration-3. (b) Number of water molecules in the hydration shell of Cl^{-} ion at various locations while permeating through the membrane. Red color is for oxygen atoms, green color is for hydrogen atoms, cyan color is for carbon atoms and blue color is for Cl^{-} ion. 57

4-14 Radial distribution function between the ions and oxygen atoms of water inside the layered GO membrane of configuration-3. 58

4-15 (a) Thickness of the layered GO membrane and (b) Number of water molecules ($\boldsymbol{N_m}$) inside the layered GO membrane during the course of simulation. 60

4-16 Intercalation of ions inside layered GO membrane (a) configuration-1 (b) configuration-2 (c) configuration-3. The green color is for hydrogen atoms, the red color is for oxygen atoms, the cyan color is for carbon atoms, the blue color is for Cl^- ions, the magenta color is for Na^+ ions, the orange color is for Mg^{2+} ions, the black color is for Al^{3+} ions, the yellow color is for sulfur atoms. 61

4-17 Internal structure of the membranes during simulations. The blockage of the water and salt passages are shown in black circles. (a) configuration-1 (b) configuration-2 (c) configuration-3. Red color is for oxygen atoms, green color is for hydrogen atoms and cyan color is for carbon atoms. 62

4-18 Water permeability of the three layered GO membrane configurations. 62

5-1 (a) A GO nanosheet. (b) The distribution of functional groups on GO nanosheet. (c) Structure of an acetic acid molecule. (d) Layered GO membrane with **D**=7 Å, **W**=8 Å and **H**= 10 Å. The green color is for hydrogen atoms, the black color is for oxygen atoms and the cyan color is for carbon atoms. 69

5-2 (a) Hydrated layered GO membrane. (b) Aqueous acetic acid solution (feed solution). (c) Draw solution. The green color is for hydrogen atoms, the black color is for oxygen atoms, the cyan color is for carbon atoms, the blue color is for Cl^- ions, the orange color is for Mg^{2+} ions, the magenta color is for Al^{3+} ions, the yellow color is for sulfur atoms. 70

5-3 Simulation setup. The green color is for hydrogen atoms, the black color is for oxygen atoms, the cyan color is for carbon atoms, the blue color is for Cl^- ions, the orange color is for Mg^{2+} ions, the magenta color is for Al^{3+} ions, the yellow color is for sulfur atoms. 70

5-4 Variation of water permeance through layered GO membranes with different values of **W**. 74

5-5 Distribution of acetic acid density for (a) D7-W0-H10 membrane system and (b) D7-W24-H10 membrane system. Distribution of water density for (c) D7-W0-H10 membrane system and (d) D7-W24-H10 membrane system. In the membrane, the green color is for hydrogen atoms, the black color is for oxygen atoms and the cyan color is for carbon atoms. The scale bar is in the unit of $atoms\times$ Å^{-3}. 75

5-6 Distribution of number density of various components in the simulation system along the permeate direction (Z direction) (a) D7-W0-H10 and (b) D7-W24-H10. The entry and exit points of the membrane are shown with a pair of dotted green line. 76

5-7 Potential of mean force along the permeating direction of layered GO membrane. The entry and exit points of the membrane in terms of reaction coordinate are shown with a pair of dotted green line. 76

5-8 (a) Variation of water permeance through layered GO membranes with different values of **H**. (b) Variation of water permeance through layered GO membranes with different values of draw solution concentration (**C**). 77

5-9 Distribution of number density of water molecules along the permeating direction (Z direction) for the membrane configuration (a) D7-W0-H8, (b) D7-W0-H10, (c) D7-W0-H12, (d) D7-W0-H14 and (e) D7-W0-H18. The boundaries of the layered GO membrane are shown with a pair of dotted green lines. 78

5-10 Draw solute rejection by layered GO membranes with (a) different **W** (b) different **H** (c) different **C**. 78

6-1 (a) GO nanosheet. (b) Layered GO membrane. (c) Simulation setup (for RO). Green color is for hydrogen atoms, black color is for oxygen atoms, cyan color is for carbon atoms, blue color is for Cl^- ions, magenta color is for Na^+ ions, orange color is for K^+ ions. 86

6-2 Simulation setup forward osmosis (FO). Green color is for hydrogen atoms, black color is for oxygen atoms, cyan color is for carbon atoms, blue color is for Cl^- ions, magenta color is for Na^+ ions, orange color is for K^+ ions. 88

6-3 Variation of number of water molecules in the permeate side ($\boldsymbol{N_P}$) with time for RO. 90

6-4 Water flux through layered GO membranes for (a) RO and (b) FO. . . 91

6-5 Intermittent H bond autocorrelation function between (a) water molecules and (b) water and GO. (c) Water reorientation dynamics inside the interlayer gallery of layered GO membranes. 92

6-6 Continuous H bond autocorrelation function between (a) water molecules (b) water and GO. 93

6-7 Radial distribution function ($g(r)$) between the oxygen atoms of water inside the layered GO membranes (a) K-GO-11.4 and P-GO-11.4 and (b) M-GO-13.6 and P-GO-13.6. 94

6-8 Permeability of Na^+ and Cl^- ions through layered GO membranes. (a) Distribution of Cl^- ions at the end of the simulation for K-GO-11.4 membrane system. (b) Spatial distribution of Cl^- ions for K-GO-11.4 membrane system. (c) Distribution of Cl^- ions at the end of the simulation for P-GO-11.4 membrane system. (d) Spatial distribution of Cl^- ions for P-GO-11.4 membrane system. (e) Distribution of Na^+ ions at the end of the simulation for K-GO-11.4 membrane system. (f) Spatial distribution of Na^+ ions for K-GO-11.4 membrane system. (g) Distribution of Na^+ ions at the end of the simulation for P-GO-11.4 membrane system. (h) Spatial distribution of Na^+ ions for P-GO-11.4 membrane system. 95

6-9 (a) Distribution of Cl^- ions at the end of the simulation for M-GO-13.6 membrane system. (b) Spatial distribution function of Cl^- ions for M-GO-13.6 membrane system. (c) Distribution of Cl^- ions at the end of the simulation for P-GO-13.6 membrane system. (d) Spatial distribution function of Cl^- ions for P-GO-13.6 membrane system. (e) Distribution of Na^+ ions at the end of the simulation for M-GO-13.6 membrane system. (f) Spatial distribution function of Na^+ ions for M-GO-13.6 membrane system. (g) Distribution of Na^+ ions at the end of the simulation for P-GO-13.6 membrane system. (h) Spatial distribution function of Na^+ ions for P-GO-13.6 membrane system. . 97

6-10 (a) GO laminates considered for PMF calculations. (b) Representative trajectory of a permeating molecule for which PMF is being calculated. (c) PMF for K-GO-11.4 membrane system. (d) PMF for P-GO-11.4 membrane system. The entry and exit points of the permeating species through the GO laminates are shown with a pair of dotted green lines. 98

6-11 Comparison of PMF between K-GO-11.4 and P-GO-11.4 membrane systems for (a) Water, (b) Na^+ ions and (c) Cl^- ions. The entry and exit points of the permeating species through the GO laminates are shown with a pair of dotted green lines. 98

6-12 (a) PMF for M-GO-13.6 membrane system. (b) PMF for P-GO-13.6 membrane system. The entry and exit points of the permeating species through the GO laminates are shown with a pair of dotted green lines. 99

6-13 Comparison of PMF between M-GO-13.6 and P-GO-13.6 membrane system for (a) Water, (b) Na^+ ions and (c) Cl^- ions. The entry and exit points of the permeating species through the GO laminates are shown with a pair of dotted green lines. 100

7-1 Graphene sheet with charged stripes. The orange color is for charged atoms, cyan color is for neutral atoms. 105

7-2 Simulation setup. (a) Front view. (b) Top view. The green color is for hydrogen atoms, black color is for oxygen atoms, blue color is for Cl^- ions, magenta color is for Na^+ ions. On the graphene sheet orange color is for charged atoms and cyan color is for neutral atoms. 105

7-3 (a) Water permeation events through nano-channels. (b) Number distribution of the velocities of the permeating water molecules through the nano-channel. 107

7-4 Charge distribution along the Z direction for nanochannel with different σ. 108

7-5 Interaction Energy between the wall and the Na^+ ions. (a) Electrostatic interactions. (b) van der Waals interactions. (c) Total interactions. 108

7-6 Interaction Energy between the wall and water. (a) Electrostatic interactions. (b) van der Waals interactions. (c) Total interactions. . . 108

7-7 Distribution of velocity of the counterions (Na^+ ions) for systems with different σ. 109

7-8 Charge density and corresponding ion density profile for $P_{0.025}$ system. (a) Charge density profile. (b) Ion density profile. 109

7-9 Charge density and corresponding ion density profile for $P_{0.05}$ system. (a) Charge density profile. (b) Ion density profile. 110

7-10 Charge density and corresponding ion density profile for $P_{0.005}$ system. (a) Charge density profile. (b) Ion density profile. 111

7-11 Charge density and corresponding ion density profile for $P_{0.01}$ system. (a) Charge density profile. (b) Ion density profile. 112

7-12 Charge density and corresponding ion density profile for $P_{0.1}$ system. (a) Charge density profile. (b) Ion density profile. 113

7-13 Charge density and corresponding ion density profile for $P_{0.2}$ system. (a) Charge density profile. (b) Ion density profile. 114

7-14 Interaction of Na^+ and Cl^- ions with the wall for $P_{0.025}$ system. (a) Electrostatic interaction. (b) van der Waals interaction. 114

7-15 Interaction of Na^+ and Cl^- ions with the wall for $P_{0.05}$ system. (a) Electrostatic interaction. (b) van der Waals interaction. 115

7-16 Interaction of Na^+ and Cl^- ions with the wall for $P_{0.005}$ system. (a) Electrostatic interaction. (b) van der Waals interaction. 116

7-17 Interaction of Na^+ and Cl^- ions with the wall for $P_{0.01}$ system. (a) Electrostatic interaction. (b) van der Waals interaction. 117

7-18 Interaction of Na^+ and Cl^- ions with the wall for $P_{0.1}$ system. (a) Electrostatic interaction. (b) van der Waals interaction. 118

7-19 Interaction of Na^+ and Cl^- ions with the wall for $P_{0.2}$ system. (a) Electrostatic interaction. (b) van der Waals interaction. 119

7-20 Interaction between water molecules and charged striped and neutral striped portion of the wall for $P_{0.025}$ system. (a) Electrostatic interaction. (b) vdW interaction. (c) Total interaction. 119

7-21 Interaction between water molecules and charged striped and neutral striped portion of the wall for $P_{0.05}$ system. (a) Electrostatic interaction. (b) vdW interaction. (c) Total interaction. 120

7-22 Interaction between water molecules and charged striped and neutral striped portion of the wall for $P_{0.005}$ system. (a) Electrostatic interaction. (b) vdW interaction. (c) Total interaction. 120

7-23 Interaction between water molecules and charged striped and neutral striped portion of the wall for $P_{0.01}$ system. (a) Electrostatic interaction. (b) vdW interaction. (c) Total interaction. 121

7-24 Interaction between water molecules and charged striped and neutral striped portion of the wall for $P_{0.1}$ system. (a) Electrostatic interaction. (b) vdW interaction. (c) Total interaction. 121

7-25 Interaction between water molecules and charged striped and neutral striped portion of the wall for $P_{0.2}$ system. (a) Electrostatic interaction. (b) vdW interaction. (c) Total interaction. 122

7-26 Water velocity profile along Z direction. (a) $\sigma = 0.005\ C/m^2$. (b) $\sigma = 0.01\ C/m^2$. (c) $\sigma = 0.025\ C/m^2$. (d) $\sigma = 0.05\ C/m^2$. (e) $\sigma = 0.1\ C/m^2$. (f) $\sigma = 0.2\ C/m^2$. 122

List of Tables

5.1 Values of geometric parameters of layered GO membranes and corresponding membrane abbreviations 69

5.2 Diffusion coefficient of water molecules inside the layered GO membranes for different value of **H**. 75

6.1 Configurations of the layered GO membranes considered in the present study and their corresponding abbreviations 87

7.1 Surface charge density considered in this present study and corresponding abbreviations 106

7.2 Thickness of the diffuse layer and distance of the stern layer from the wall for systems with different σ 112

Chapter 1

Introduction

Each year March 22 is observed as "World Water Day". This is an initiative started by United Nations (UN) back in 1993 to create awareness among the people regarding water crisis around the world. In the words of UN chief António Guterres "This yearâĂŹs World Water Day focuses on water and climate change. With 2020 a make-or-break year for climate action, this focus is timely". Water is one of the most essential element to sustain life in our planet earth. Nearly 60% of human body is water. Apart from this water is essential for irrigation, various micro and nanodevices, cooking, cleaning and washing and for keeping our environment healthy. Around 70% of our planet earth is covered with water. However, only 2.5% of it is fresh water. Again, only 1% of the freshwater is accessible to mankind and the remaining portion is trapped in glaciers and snowfields. So, merely 0.007% of our planet's water is available to mankind. The amount of freshwater on our planet is always the same over the years. However, the explosive growth of population and rapid industrialization cause the severe water scarcity around the globe. In many parts of the world people are struggling to get clean water. One third of the world population has to deal with severe water crisis at least a month each year. Around 785 million people around the world (which is roughly 1 in every 9 person) has no access to clean usable water. By the year 2050, at least 1 in 4 people of the world population will live in a state of chronic or recurring fresh-water shortages unless appropriate measures were taken. The World Economic Forum identify water crisis as the fourth global risk, in terms

of impact on the society. Unsafe water kills more people around the globe than war and violence. In every 37 seconds one person dies from water borne diseases. This also includes the 800 children under the age five who lost their lives each day from diseases caused by unsafe water and poor sanitization. Water crisis also has severe impact on the growth and development of children and women. Children are more vulnerable to waterborne diseases. Each day women and girls around the world spend around 200 million hours carrying water for their families. In Africa, on an average, women walks around 6 kilometers to fetch 40 pounds of water each day.

"WASH in Healthcare Facilities", a publication by the World Health Organization and UNICEF, raises the issue of health and safety concerns surrounding the COVID-19 pandemic. During the Ebola outbreak in 2014, the health care personnels did not have adequate access to clean water in places like Liberia. Now, similar scenario arises amidst COVID-19 outbreak in many parts of the world.

According to the World Resources Institute, a US-based organization working on sustainable development, India ranks 13 among the 17 worst affected countries across the globe. India ranks 120 out of 122 countries across the globe in global water quality index with nearly 70% of country's water contaminated. In many parts of the country sewage, chemicals and effluents are often directly released into the water bodies. Groundwater, which makes up 40% of India's water supply is gradually depleting over the years. As per the report of country's Central Water Commission on June 2019, around two third of the India's water reservoir are running below normal water levels. As per the report of National Institution for Transforming India (NITI Aayog), currently 600 million Indians are facing "high to extreme water stress"and by the year 2030 India's water demand likely to be doubled. About 40% of Indians will have no access to potable water by 2030. Over 21% of our country's diseases are waterborne diseases. Around 200,000 Indians are dying every year having no access to clean and safe water. They also added that major cities like Delhi, Bengaluru, Chennai, Hyderabad etc. will run out of ground water by 2020 which will severely affect 100 million Indians. India's sixth largest city Chennai, is facing severe water crisis in recent years to the extent that offices, hotels, restaurants and hostels were

closed temporarily to fight against the water shortage.

Union budget of India 2020 also puts concern over the growing water crisis in the country and announces some critical measures to neutralize the same. One of them is Jal Shakti Abhiyan campagian which focuses on rain water harvesting and water conservation. Other include renovating the traditional water bodies and tanks, afforestation, reuse of water, watershed development etc. Similarly, Jal Jeevan Mission focuses on providing the potable water to the rural areas by 2024.

Easy availability of clean usable water also has great impact on country's overall development. If proper counter measures are not implemented, India will likely to loss 6% in is gross domestic product (GDP) as reported by NITI Aayog. Easy accessibility to clean water leads to better hygiene and sanitation. As a consequence overall health issues among the people reduces. Children are less likely to miss schools due to waterborne diseases. Similarly parents are less worried about fetching clean water and waterborne diseases. Instead, they can be more focused on various productive activities (eg. growing crops, attending offices on regular basis, various social activities). In other words, easy availability of clean water leads to smooth running to the education and learning, growing economic prosperity and improve overall public health.

Without water there would be no life on our planet. It is the duty of every human being to act responsibly and use judiciously the water resources in this desperate time. It also urges the research community to search for alternative water resources (e.g. sea water desalination, waste water purification) and innovative and efficient water purification technologies. Considering the environmental impacts of these emerging methods, the methods that produce and conserve water and energy without causing any pollution and exhaustion of energy sources are more suitable for sustainable development of human civilization. The effectiveness of these processes can also be enhanced by utilization of waste and abundant, low value water and energy resources as inputs in these processes. In that aspect membrane separation technologies emerges as one of the efficient water purification (or separation) methods. In olden days processes like coagulation and flocculation, granular media filtration,

sand filters etc. were widely used for water filtration and purifications. From early 1990, membrane filtration started to take over these process for water filtration. With the rapid growth in the material science and membrane manufacturing processes, it becomes the mainstream technology for water purification and desalination applications. Apart from this membrane processes find their applicability in a wide range of applications. Separation, concentration and purification of molecular mixtures are integral parts of most of the industrial processes. Today hardly any industry is there that does not require membrane application. Starting from food and biotechnology industries, metal industries, leather and textile, pulp and paper industries, chemical process industries, health-pharmaceutical-and medical industries, waste treatment industries; everywhere membrane applications play a vital role. Membrane processes have potential applicability in "zerowaste" processes where the rejected streams can be reused for various processes. In the metal industry, NaOH or H_2SO_4 are used as solvents during metal treatment which generates waste streams consisting of acids or bases with metal wastes. These streams can be fed to a membrane system before releasing them to the environment.

The word membrane is derived from the Latin word “membrana” which means skin. Typically a membrane resembles a selective boundary between two phases and has a semi-permeable nature. A membrane (liquid or solid) selectively separates substances when a driving force is applied across the membrane. The membrane separation process is rarely spontaneous and usually require a net driving potential across the membrane. The driving potential can be supplied in terms of mechanical potential gradient (e.g. hydraulic pressure), electric potential gradient, chemical potential gradients (concentration or osmotic pressure or vapor pressure), temperature gradient or heat.

Over the years membrane technologies become a vibrant field of research and innovative membrane materials and processes are being emerged frequently. Membrane processes are simple, easy to operate and require less maintenance as compared to most of the separation processes. The easy availability of a large range of materials (various polymers and inorganic materials) for membrane applications imparts mem-

brane separation processes with greater controllability over separation selectivities. With the rapid progress in nanoengineering, membrane with very high selectivity can be produced for specific separation applications. The typical value of these selectivities are much higher as compared to relative volatility for distillation operations. Membrane processes can separate species at molecular scales up to a practically visible scale. Because of this, it is possible to obtain large number of separations through membrane separation process.

Membranes are integral part of all living systems. Apart from their extensive use in water purification, desalination, industrial separation; all biological cells that composes a living organism are surrounded with membranes. The history of synthetic membrane began in 1748 when French Abble Nollet demonstrated the semipermeability of animal bladder for water over wine. However, the first person to prepare and study an artificial semi-permeable membrane is Adolf Fick. He prepared an artificial membrane from an ether-alcohol solution of cellulose called "collodion". Interestingly the phenomenon he proposed which is popularly known as "Fick's law of diffusion" is still in use as a first order description of diffusion through membranes. The first industrial scale membrane was prepared by Sartorius Werke GmbH (Germany) in 1950 which was a micro-filtration membrane. After that in a major breakthrough, in late 1950, Loeb and Sourirajan prepared asymmetric thin reverse osmosis membrane.

Membranes are typically prepared through methods like sintering, stretching, track-etching, phase inversion, coating etc. Depending on the constituting materials membranes are classified as polymeric membrane, liquid membrane, solid (ceramics) membrane and ion exchange membrane. Based on their physical configurations, membranes could be classified as flat (sheet) membrane, spiral wound, tubular, and emulsion. Similarly, depending on their use membranes are classified as fine filtration (micro-filtration/MF, ultrafiltration/UF, nanofiltration/NF, and reverse osmosis/RO), dialysis, electrodialysis (ED), gas separation (GS), carried-mediated transport, control release, membrane electrode, and pervaporation (PV). The main advantages of membrane processes as compared to other separation processes are energy consumption, simplicity and environmental friendliness. In membrane separation

processes there is no need for extractor or adsorber to carry forward the separation process. The separation is primarily initiated by the difference in rate of transfer of the substances through the membrane. That is why membrane separation is a clean "Technology" in which no additive materials (which could be potential pollutants) are required. Except pervaporation, typical membrane processes do not require phase change for separation of impurities. So, energy requirement in membrane processes are less. They can be carried out at normal conditions which make them energy efficient from other separation processes e.g. thermal distillation. The membrane processes can extract the component from a solvent with less than 10% energy consumption as compared to the energy requirement in evaporation and distillation processes. Membranes modules are easy to design, compact and can be operated with minimum of effort.

Membranes, which are used for water treatment in general include micro-filtration (MF), ultrafiltration (UF), reverse osmosis (RO), and nanofiltration (NF) membranes. Out of these, MF membranes have the largest pore size and can rejects large particles and various microorganisms. UF membranes have smaller pores than MF membranes. So, along with large particles and microorganisms they also can rejects bacteria and soluble macromolecules such as proteins. RO membranes are effectively non-porous in nature. Their rejection ability is higher than MF and UF membranes and can even rejects salt ions, organic dies etc. NF membranes are relatively new and sometime referred to as "loose RO" membranes. The pores of NF membranes are of the order of angstrom and their performance falls between RO and UF membranes.

Membranes are broadly classified into two categories: isotropic membranes and anisotropic membranes. Isotropic membranes have uniform composition. The physical nature of the membrane is also uniform across the cross-section of the membrane. Anisotropic membranes are non-uniform in nature over the membrane cross-section. Anisotropic membranes are consist of layers which can vary in structure and chemical compositions. Most of the presently available membranes are made up of synthetic polymers. MF and UF are generally made up of same membrane materials, but they are prepared through different procedures which results in different pore sizes. Some

of the MF and UF membrane materials are poly(vinylidene fluoride), polysulfone, poly(acrylonitrile), poly(acrylonitrile)-poly(vinyl chloride) copolymers etc. [6]. RO membranes are in general either cellulose acetate or polysulfone coated with aromatic polyamides [6]. Similarly, NF membranes are made of cellulose acetate blends, polyamide composites or sulfonated polysulfone [7]. Ceramics and metals can also be used as membrane materials. Ceramic membranes are generally used for microfiltration and often attributed as thermally and chemically stable [6]. However, high production and maintenance cost and mechanical fragility of ceramic membranes hindered their wide-spread applicability. Metallic membranes are typically made up of stainless steel and are very finely porous. They are primarily used for gas separation but can also be used for high temperature water filtration or as membrane support.

Most of the presently available commercial membranes are polyamide, ceramic and zeolite based membranes [8]. Although, extensive investigations were carried out over the past few decades these membranes are still prone to severe functional drawbacks. The polymeric membranes have less resistance to strong acidic environment and organic solvents. Their performance also hindered by the lack of high temperature stability. Ceramic membranes are limited by the large scale applications and zeolite membranes are suffered from very low water flux.

In general, if someone attempts to increase the flux of a membrane based separation process it results in decrease in selectivity at the same time. But, the desirable scenario is to increase both flux and selectivity of the membrane. That is why membrane based separation processes are suitable for highly selective applications where flux is not important such as that carried out in pharmaceutical industries. The dependability problem associated with the membranes is mainly due to difference in characteristics from one membrane to another. So, a direct scale up of membrane processes is not possible. It is important to access the performance and the physical/chemical properties of a membrane in the pilot scale or in laboratory before going for industrial scale production and application of the same. Another major issue with membrane separation process is membrane fouling. Fouling causes a decline in membrane performances. The solutions to these problems may lie in the hydrody-

namic of the processes, pretreatment of the upstream flows and innovative membrane materials.

In the recent years, nanoporous two-dimensional (2D) material such as graphene, graphene oxide (GO), molybdenum disulfide (MoS_2) gain considerable research interest for highly selective separation applications [9, 10, 11, 12, 13, 14, 15]. GO is a chemical derivative of graphite which is rich in oxygen containing functional groups (hydroxyl, epoxy, carboxyl etc.) has extensively been studied in recent years for membrane based separation applications [16, 17, 18, 19, 20, 21, 22, 23]. It exhibits exceptional electrochemical, mechanical, and optoelectronic properties, which makes it a promising candidate in batteries, field-effect transistors, nanocomposites, biomedical, and drug delivery applications.

GO was first synthesized in 1859 by Sir 2^{nd} Baronet Benjamin Collins Brodie, via oxidation of bulk graphite with potassium chlorate and nitric acid, but its chemical and structural nature has been studied only after more than a century by Lerf and Klinowsky [24] through a careful analysis of solid-state C_{13} nuclear magnetic resonance (NMR) spectra.

Figure 1-1: GO dispersed in water (3 $mgmL^{-1}$) [1].

Because of its hydrophilicity, graphite oxide is easily dispersed in water, where it breaks up into macroscopic atomically thin flakes, leading to solutions/suspensions of single layer GO. A typical GO solution has a brownish appearance, whose transparency and âĂŸstrengthâĂŹ is tuned by varying the solute concentration (Figure 1-1). GO membranes preferentially have a laminate structure with nanometer scale interlayer distance [25, 26, 27]. The spacing inside the interlayer gallery of these

GO laminates acts as nanocapillary through which water and other molecules/ions can selectively permeate through [28, 29, 30]. The functional groups and interlayer separations of a layered GO membrane can aptly be tuned for specific separation applications [31, 32, 33, 34].

The conventional method for preparation of GO is to oxidize graphite flakes using strong oxidants such as $KMnO_4$, $KClO_3$ or $NaNO_2$ in the presence of strong acids such as concentrated sulphuric acid or nitric acid [17]. The most widely used method for synthesizing GO is modified Hummers' method [29, 34, 35, 36, 37, 38]. The individual GO sheets are then exfoliated by ultrasonication. The C/O ratio in GO sheets indicates the degree of oxidation and can be quantified by elemental analysis or X-ray photoelectron spectroscopy (XPS). The typical C/O ratio for GO reported in the literature is $2.0 - 4.0$ [20, 39, 40]. Because of their single atomic thickness GO nanosheets are easily stackable [29]. The strong interlayer hydrogen bond between the GO nanosheets hold them together as a freestanding membrane with sufficient mechanical strength [41]. Layered GO membranes can be prepared from GO suspensions using methods such as vacuum filtration method [17, 25, 34, 36] vacuum suction method [29], spin or spray coating of GO aqueous colloids [17].

Despite the experimental efforts, the potential of GO has not yet been extensively explored by molecular modeling. This is mainly due to the lack of an atomistic GO model for theoretical calculations. Formed by treating graphene with very strong oxidizing agents (e.g., $KClO_3/HNO_3$), the chemistry of GO depends strongly on the synthesis process and the level of oxidation. As a result, the amorphous feature of GO structure imposes challenges in determining a unique atomic model. Considerable efforts have been undertaken in the past decade to determine atomistic GO structures. Different models have been proposed and have gained success to some extent in explaining experimental and theoretical observations [42]. The understanding of GO structures includes the possible functional groups and the range of their concentrations. For instance, it is accepted that the hydroxyl and epoxy groups are distributed on the basal plane, while the carboxyl and alkyl groups are normally located at the edges [19]. Despite these findings, other key information, such as the combination of

the type, concentration and the distribution of functional groups, remains unclear. Previous theoretical studies of GO usually focus on the local structure where only one or two types of functional groups are considered and a handful of basal carbon atoms are investigated. This is inadequate to understand the structure-property relationship of GO and can hinder the design and optimization of GO material towards different applications.

With a limited fresh water resources of our planet, sea water desalination has a huge potential for long term solution to our water scarcity. Among all the currently available techniques for sea water desalination, the most efficient one is the reverse osmosis (RO). Reverse Osmosis (RO) is a process that uses semipermeable membranes to separate and remove dissolved solids, organic, pyrogens, submicron colloidal matter, color, nitrate and bacteria from water. Feed water is delivered under pressure through the semi permeable membrane, where water permeates the minute pores of the membrane and is delivered as purified water called permeate water. Impurities in the water are concentrated in the reject stream and flushed to the drain is called reject water. These membranes are semi-permeable and reject the salt ions while letting the water molecules pass. The materials used for RO membranes are made of cellulose acetate, polyamides and other polymers. The membrane consists of hollow-fiber, spiral-wound; depending on the feed water composition and the operation parameters of the plant.

The RO process is simple in design consisting of feed, permeate and reject stream. For feed water it is necessary to provide pretreatment in order to remove inorganic solids and suspended solid and using high pressure, pump the given feed through semipermeable membrane. Depending upon the permeate where it is used necessary post treatment is given. A schematic diagram of the RO process is shown in Figure 1-2.

An RO desalination plant essentially consists of four major systems:

- Pretreatment system.
- High-pressure pumps.

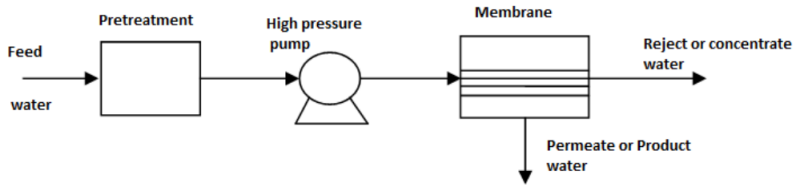

Figure 1-2: Schematic Diagram of the RO Process [2].

- Membrane systems.
- Post-treatment.

Pre-treatment system is provided to remove all suspended solids so that salt precipitation or microbial growth does not occur on the membranes. High-pressure pumps supply the pressure needed to enable the water to pass through the membrane and have the salt rejected. The pressure ranges from 17 to 27 bar for brackish water, and from 52 to 69 bar for seawater [2]. Membrane systems consist of a pressure vessel and a semi-permeable membrane inside that permits the feed water to pass through it. RO membranes for desalination generally come in two types: Spiral wound and Hollow fiber. Depending upon water quality of permeate and use of permeate; post treatment may consists of adjusting the pH and disinfection.

However our main focus is on the membrane materials. Membranes, which are used in an osmosis (either RO or FO) should have the following characteristics.

- The membrane should be inexpensive, have longer and stable life.
- Membrane should be easily manufactured with good salt rejection i.e. slightly permeable to salt.
- They should have high water flux i.e highly permeable to water. They should permit the flow of large amounts of water through the membrane relative to the volume they occupy.
- They should be less susceptible to fouling. The membrane should chemically, physically and thermally stable in saline waters. They need to be strong enough to withstand high pressures and variable feed water quality.

In the past four decades, membrane development has occurred based on the demand in pressure driven processes. However, in the last decade, the interest in osmotically driven processes, such as forward osmosis (FO) and pressure retarded osmosis (PRO), has increased. National Geographic [43] in an article in March 2010 cited FO as one of the three most promising new desalination technologies. The process, just like reverse osmosis (RO), requires a selectively permeable membrane separating two fluids with different osmotic pressures (Figure 1-3) and was first observed by Albert Nollet in 1748. The process exploits the natural process of osmosis, which is how plants and trees take up water from the soil-a low energy, natural process. It works by having two solutions with different concentrations (or more correctly different osmotic pressures) separated by a selectively permeable membrane, in the case of the plants and trees their cell walls, and "pure" water flows from less concentrated solution across the membrane to dilute the more concentrated solution, leaving the salts behind. The process in its pure form takes place at atmospheric pressure, with variations such as pressure enhanced osmosis (or reverse osmosis) and pressure retarded osmosis. Figure 1-4 shows a schematic of a FO plant for sea water desalination. The process is inher-

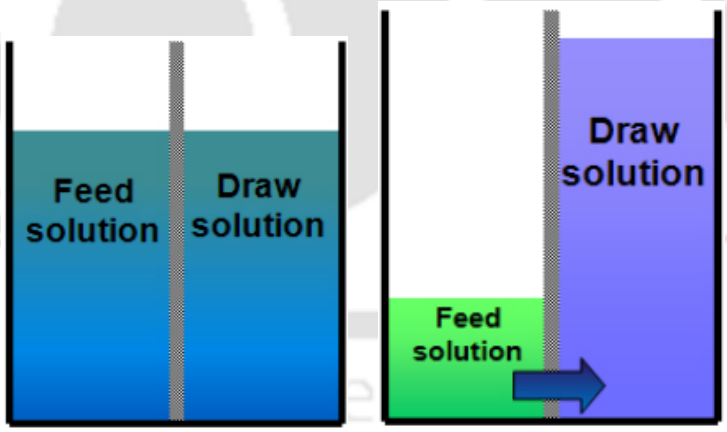

(a) Osmotic equilibrium. (b) FO ($\Delta P = 0$).

Figure 1-3: Schematic of the FO process [3].

ently less prone to fouling than pressure driven membrane processes and depending on how and if the osmotic agent/draw solution is recovered, has a direct affect on the energy consumption of the overall process when it is fully integrated. The process has

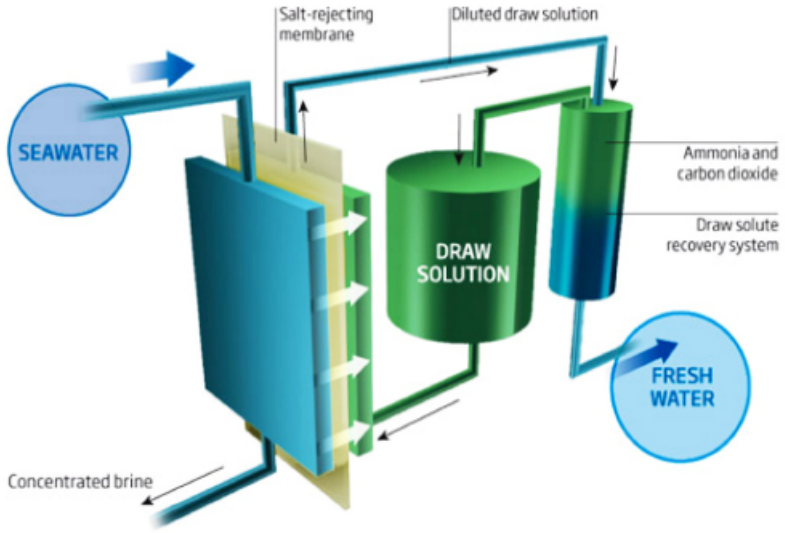

Figure 1-4: An illustration of forward osmosis desalination [3].

considerable potential across a wide variety of applications; emergency drinks, power generation, enhanced oil recovery, fluid concentration and desalination. However only a few of these applications have been currently commercialized.

In this present study, the applicability of 2D membrane materials are studied using non-equilibrium molecular dynamics (MD) simulations. The 2D materials considered in this study are graphene and graphene oxide. The thesis is distributed in the following chapters:

- Chapter 2 describes briefly about the essence of computational modeling and brief description of MD simulations.
- Chapter 3 is the Literature review which provides an insight into the previous relevant works.
- Chapter 4 discusses the applicability of layered GO membrane for sea water desalination using FO process.
- Chapter 5 discusses the dehydration of acetic acid using layered GO membrane through FO process.

- Chapter 6 discusses the effect of cation intercalation on the performance of layered GO membrane.
- Chapter 7 discusses the electro-osmotic flow through a rectangular nanochannel with surfaces having striped patterned charge distribution.
- Chapter 8 discusses the conclusions from the present study and the scope for future investigations.

Chapter 2

Simulation Methodology

2.1 Essence of Computational Modeling

While experiments form the core of scientific research, all experimental methods have intrinsic and practical limitations in e.g. spatial and temporal resolution. In some cases experiment is

1. impossible: e.g. Inside of stars, Weather forecast.
2. too dangerous: e.g. Flight simulation, Explosion simulation.
3. expensive: e.g. High pressure simulation, Windchannel simulation.
4. blind: i.e. Some properties cannot be observed on very short time-scales and very small space-scales.

On the other hand, an analytical solution to given certain problem may be too difficult or impractical (e.g. solution to the classical 3-body problem). The computation is not merely intended to generate an expected result, it is rather a virtual laboratory in which the behavior of a system can be described and predicted. In this respect, computer simulation represents an intermediate level between experiment and theory.

Simulation is a useful complement, because it can:

- provoke experiment.

- explain experiment.

- aid in establishing intellectual property.

In other words computer simulation is a powerful and modern tool for solving scientific problems as numerical experiments can be performed for new materials without synthesizing them. One of the aims of computer simulation is to reproduce experiment to elucidate the invisible microscopic details and further explain experiments. On the other hand, simulation can also be used as a useful predictive tool. The most widely used simulation methods for molecular systems are Monte Carlo, Brownian dynamics and molecular dynamics.

2.2 Molecular Dynamics

Molecular dynamics (MD) is a computational methodology aimed at the solution of the N body problem, based on the classical analytical mechanics of Hamilton and Lagrange. A system of N interacting atoms is studied by solving the Newtonian equations of motion. The first molecular dynamics simulations were carried out by B.J. Alder and T.E. Wainwright [44]. They investigated a solid-fluid transition in a system composed of hard spheres interacting by instantaneous collisions. Some years later the interaction of a set of Lennard-Jones molecules was studied, and the name "molecular dynamics" was coined.

In classical MD the system under study is entirely classical, this means the quantum nature of atomic and molecular degrees of freedom is neglected. Therefore, classical molecular dynamics can be applied only to describe phenomena where quantum effects are not relevant or can be included as semi-classical corrections. Also relativistic effects are not taken into account, which means that the speed of light is infinite and all interactions are instantaneously propagated. However, we can go for much larger system and longer timescale as compared to quantum mechanics/quantum MD using classical MD simulation.

MD is a sampling method. But there are other sampling methods like Monte

Carlo (MC). However MD gives us "DYNAMICS" of the system. MD has advantage over MC method with regard to non-equilibrium processes and dynamic properties. In long time limit, and for equilibrium properties, the results of MC correspond to results obtained by MD. However, MD can model processes that are characterized by extreme driving forces and that are non-equilibrium processes, MC can not, eg. fracture.

The need of atomistic simulations:

- For understanding experimental observations.
- For obtaining molecular level information that can't be found experimentally.
- For checking theoretical results.
- For study conditions which are not accessible experimentally.

As with any computational method, in molecular dynamics one needs to find a good compromise between accuracy, scale of the system studied and (real) time used. Hence, it is difficult to state what is the maximum number of atoms, or length of simulation in contemporary molecular dynamics. Typically MD simulations feature 10^2-10^8 atoms over times of 10 ps to 100 ns.

During an MD simulation, starting from arbitrary initial conditions, a trajectory in phase space is generated by numerically integrating the equations of motion. Each point in phase space represents a set of positions and velocities of all N degrees of freedom forming the molecular system. The dynamic trajectory is a sequence of points generated at following time steps that entirely describes the motion of the molecular system. Time is the discrete independent variable used in the integration of the equations of motion.

2.2.1 Force Field

The heart of any molecular dynamics scheme is the force field used to analytically describe the atomistic interactions. Regardless of the merits of the other algorithms in the simulation code (integrators, pressure and temperature controls etc.), whether

or not the simulation produces realistic results depends ultimately on the force field. Force calculations are also the computationally most intensive parts of a molecular dynamics simulation code, taking up to 95% of the total simulation time. Force fields are obtained either empirically (classical MD) or from QM approximations (*ab* initio MD).In this study the OPLS-AA force field is considered for the MD simulations.

OPLS-AA Force Field

In OPLS-AA force field [45] the following bonded interactions are considered.

- Bond Stretching

$$V_b\left(r_{ij}\right) = k_{ij}^b\left(r_{ij} - b_0\right)^2 \tag{2.1}$$

The bond stretching interaction between atoms i, j is given by $V_b\left(r_{ij}\right)$ which is modeled through Eq. 2.1. Here b_0 is the equilibrium bond distance between atoms i,j and r_{ij} is the instantaneous bond distance between them. k_{ij}^b is the spring constant of the bond between i and j.

- Bond-angle Bending

$$V_a\left(\theta_{ijk}\right) = k_{i,j,k}^{\theta}\left(\theta_{ijk} - \theta_{ijk}^0\right)^2 \tag{2.2}$$

The bond-angle bending interaction $V_a\left(\theta_{ijk}\right)$ between the three atoms i, j and k which are bonded through two bonds is given by Eq. 2.2. θ_{ijk} is the instantaneous bond angle between i, j, k with j being the central atom. θ_{ijk}^0 is the equilibrium bond angle and $k_{i,j,k}^{\theta}$ is the corresponding force constant.

- Torsional Interaction

$$V_d\left(\phi_{ijkl}\right) = \frac{V_1}{2}\left[1+\cos(\phi+f_1)\right] + \frac{V_2}{2}\left[1-\cos(2\phi+f_2)\right] + \frac{V_3}{2}\left[1+\cos(3\phi+f_3)\right] \tag{2.3}$$

The torsional interaction $V_d\left(\phi_{ijkl}\right)$ due to the torsional angle ϕ_{ijkl} between the planes containing the atoms with indices i, j, k and j, k, l is given by Eq. 2.3 where V_i, $(i = i, 2, 3...)$ is the corresponding Fourier coefficients for torsional energy functions.

The non-bonded interactions in the present simulation are van der Waals interaction and Coulomb interaction.

- van der Waals Interaction

$$V_{\mathrm{LJ}}\left(r_{ij}\right) = \frac{C_{ij}^{(12)}}{r_{ij}^{(12)}} - \frac{C_{ij}^{(6)}}{r_{ij}^{(6)}} \tag{2.4}$$

In this present work the van der Waals interaction is modeled through Lennard-Jones (LJ) potential given by Eq. 2.4. The parameters $C_{ij}^{(12)} = 4\epsilon_{ij}\sigma_{ij}^{(12)}$ and $C_{ij}^{(6)} = 4\epsilon_{ij}\sigma_{ij}^{(6)}$ depend on the pair of atom types. For the interactions with different atom types the following combination rules are applied

$$C_{ij}^{(6)} = \left(C_{ii}^{(6)}C_{jj}^{(6)}\right)^{1/2} \tag{2.5}$$

$$C_{ij}^{(12)} = \left(C_{ii}^{(12)}C_{jj}^{(12)}\right)^{1/2} \tag{2.6}$$

$$\epsilon_{ij} = \left(\epsilon_{ii}\epsilon_{jj}\right)^{1/2} \tag{2.7}$$

$$\sigma_{ij} = \left(\sigma_{ii}\sigma_{jj}\right)^{1/2} \tag{2.8}$$

In the above expression ϵ_{ij} is the potential well depth and σ_{ij} is the distance where potential equals zero.

- Coulomb Interaction

$$V_C\left(r_{ij}\right) = \frac{1}{4\pi\epsilon_0}\frac{q_i q_j}{\epsilon_r r_{ij}} \tag{2.9}$$

Here ϵ_0 and ϵ_r are the vacuum and relative dielectric permittivity, respectively.

2.2.2 Integration of Equation of Motion

Under the influence of a continuous potential energy function, the atoms moving according to a dynamics simulation give rise to a many-body problem that cannot be solved analytically. Therefore the equations of motion are integrated numerically using a finite difference method. The basic idea is that the integration is broken down into many small stages, each separated in time by a fixed time step δt. The total force on each atom in the configuration at time t is calculated as sum of all interactions with other atoms. Using the Newtonian equation, the acceleration is obtained from the force. Then, combining it with the positions and velocities at time t, the new positions and velocities at the subsequent time step $t + \delta t$ are computed, forces are also calculated and the procedure is repeated to get new values at time $t + 2\delta t$. The force is assumed to be constant during each time step.

There are different algorithms for integrating the equations of motion. Some of them assume that positions and dynamical quantities can be expressed as Taylor series expansions:

$$\overrightarrow{r}\left(t+\delta t\right) = \overrightarrow{r}\left(t\right) + \delta t\overrightarrow{v}\left(t\right) + \frac{1}{2}\delta t^2\overrightarrow{a}\left(t\right) + ... \tag{2.10}$$

$$\overrightarrow{v}\left(t+\delta t\right) = \overrightarrow{v}\left(t\right) + \delta t\overrightarrow{a}\left(t\right) + \frac{1}{2}\delta t^2\overrightarrow{b}\left(t\right) + ... \tag{2.11}$$

$$\overrightarrow{a}\left(t+\delta t\right) = \overrightarrow{a}\left(t\right) + \delta t\overrightarrow{b}\left(t\right) + ... \tag{2.12}$$

where $\overrightarrow{r}(t)$, $\overrightarrow{v}(t)$, $\overrightarrow{a}(t)$ and $\overrightarrow{b}(t)$ indicate respectively position, velocity, acceleration and first derivative of the acceleration, all evaluated at time t. Acceleration is obtained at all times by means of the NewtonâĂŹs equation. In a system of N interacting atoms described by the potential energy function $U\left(\left\{r^{\vec{N}}\right\}\right)$, the acceleration of i-th atom with mass m_i can be evaluated from the following equation

$$m_i \overrightarrow{a}_i = -\nabla U\left(\left\{\overrightarrow{r^N}\right\}\right) \tag{2.13}$$

2.2.3 Boundary Conditions

Boundary effects can play an important role in MD simulations especially in case of small numbers of atoms, with a large ratio between surface and volume parts. The correct treatment of boundaries is crucial to MD simulations because it enables the calculation of bulk properties, which characterize a macroscopic molecular system. In this present study periodic boundary conditions (PBC) are used.

Periodic Boundary Conditions

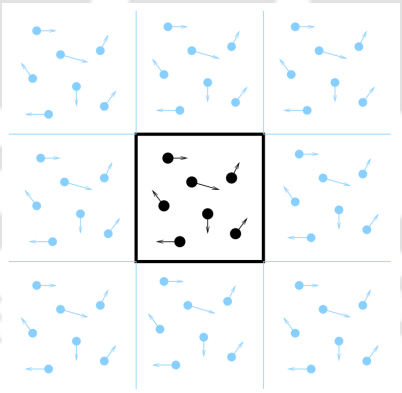

Figure 2-1: Periodic Boundary Conditions; illustration in two dimension. The simulation box is highlighted at the center, and is surrounded by periodic images of itself [4].

Frequently one is confronted with the need to study a system, periodic or not, which contains large numbers of atoms or molecules, where large means of the order of N_A, Avogadro's number. Naturally, we cannot deal with such large numbers, so

we must resort to some computational tricks in order to emulate a system in these conditions. The trick used in this case is referred to as periodic boundary conditions (PBC), and consists of assuming that the simulation box (i.e. the box containing the atoms in the simulation) is surrounded by identical copies of itself in all directions.

The periodic boundary condition (PBC) consists in putting the molecular system into a box, usually of cubic shape, and then generating a number of identical copies or images of the system adjacent to each face of the central box. The central molecular system evolves according to the Newtonian equations and interacts with the images, whose motion is a replica of the central dynamics. Moreover, the number of atoms in the central box is conserved, since for each particle leaving the box on one side the corresponding image enters the same box on the opposite side. One can easily see that the surface effects are thus virtually eliminated and the position of the box boundaries plays no role.

2.2.4 Validation of the Force Field

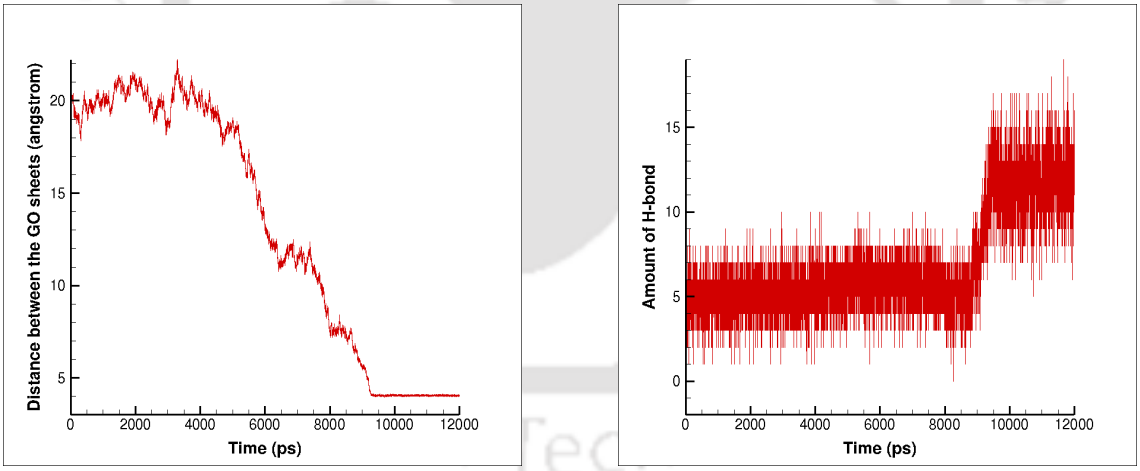

(a) (b)

Figure 2-2: (a) Distance between two GO nanosheets and (b) number of hydrogen bonds between two GO nanosheets during the aggregation process obtained through our force field parameters.

The partial charges and the OPLS-AA parameters of the GO nanosheets considered in this present study are similar to the one used by Shih *et al.* [46]. We have

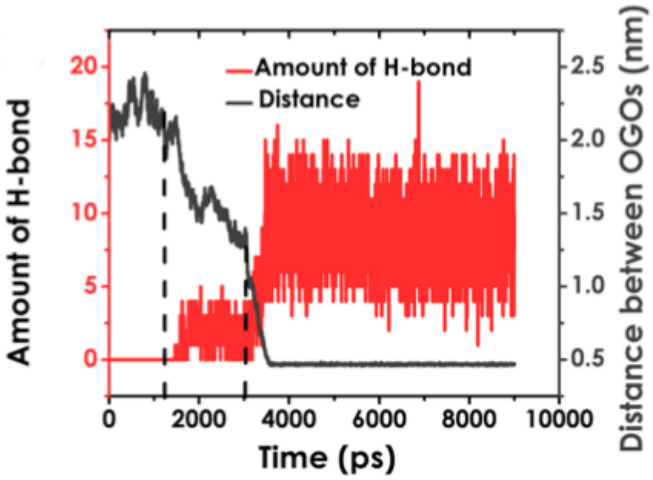

Figure 2-3: Distance between two GO nanosheets and number of hydrogen bonds between two GO nanosheets during the aggregation process as reported by Tang *et al.* [5].

requested Prof. Shangchao Lin to provide us the partial charges and the force field parameters for GO and we are grateful to him for being kind enough to provide us the same.

Before employing these parameters to investigate the performance of layered GO membranes, they have extensively been examined to reproduce the works available in the existing literature. For example, the OPLS-AA parameters of GO has been verified by reproducing the work of Tang *et al.* [5]. Tang *et al.* [5] studied the aggregation process of GO in water and we are able to reproduce their work with the force field parameters used in the present work as shown in Fig. 2-2a and 2-2b. The observations reported by Tang *et al.* [5] is shown in Fig. 2-3 and we have reproduced their observations as shown in Fig. 2-2. (The trend of plots in Fig. 2-2 and 2-3 are same although there is quantitative difference in the time axis i.e. X axis. This is usual depending on the initial configurations of the MD simulation as Tang *et al.* [5] themselves reported in their study.)

भारतीय प्रौद्योगिकी संस्थान गुवाहाटी
Indian Institute of Technology Guwahati

Chapter 3

Literature Review and Objectives

3.1 Literature Review

Previous studies points serious concern about the present global water crisis and in the days to come [47, 48, 49, 50, 51]. Water scarcity around the globe due to rapidly rising water demand and climate change is a major concern for global economy too [49]. As such, there is an urgent need of awareness among all the stakeholders starting from private sector initiatives to governmental regulation and common people to plan and execute sustainable use of water. In particular there should be some serious effort to improve the global water productivity [50]. Seckler *et al.* reported that at least quarter of the population in the developing countries will face severe water crisis if proper preventive measures are not initiated. They express particular concern for the semi-arid regions of Asia and Middle East.

As reported in Chapter 1, the gradually depleting usable water resources and the increasing consumption urges for energy efficient, environmentally sustainable water treatment technologies [52, 53]. Among the membrane processes for sea water desalination and waste water treatment the most widely used ones are nano-filtration (NF), reverse osmosis (RO) and recently emerging forward osmosis process [54, 55]. All of these processes involve a semipermeable membrane and the most widely used one till date are the thin-film composite (TFC) polyamide membranes due to their good selectivity and wide pH tolerance. However, TFC membranes have certain

prevailing limitations, e.g., low permeation resistance to chlorine [56, 57] low fouling resistance [58, 59, 60, 61] and low energy efficiency [62]. Another drawback with TFC membrane is, it is difficult to produce TFC membrane with thinner, more hydrophilic and more porous support layer which are among the important factors for obtaining efficient FO membrane [63]. Considering these factors, significant attention on the searching of new membrane material and corresponding synthesis methodology is highly desirable in the present day scenario.

3.1.1 Graphene Based Nano Materials for Membrane Applications

Graphene-based nano materials draw significant attention from the research community over the years because of their many inherent interesting properties such as adsorption of metal and organic dyes, antimicrobial capability, and photo-catalytic degradation of organic molecules [64, 65, 66, 67, 68, 69]. Suk *et al.* [70] and Tanugi *et al.* [15] performed MD simulations on utilization of graphene-based nanomaterials for water purification membrane. They simulated nanopores on graphene monolayers through which water can permeate but selectively reject other substances. They reported that monolayer nanoporous graphene is a potential candidate for sea water desalination membrane with water permeability several times higher than that for current RO membranes. The water permeability can effectively be controlled through appropriate selection of pore sizes and functional groups. Recently an experimental study on porous graphene membranes was reported, where ultraviolet-induced oxidative etching was used to generate nanopores on graphene sheets and the membrane selectivity for gas separation was tested. Similarly, Koenig *et al.* [71] reported the membrane selectivity of nanoporous graphene. They generated the nanopores on the graphene sheets through ultraviolet-induced oxidative etching.

Another important graphene based material is graphene oxide (GO). GO nanosheets can be easily prepared through chemical oxidization and ultrasonic exfoliation of graphite [72, 73] which imparts it with significantly low material manufacturing cost

and promotes scale-up commercial membrane synthesis process. GO layers are highly stable in acidic medium as they are prepared by deep chemical oxidation of graphite using strong acid as oxidants [74]. Due to the presence of oxygen containing functional groups in the GO membrane such as hydroxyl, epoxide, carboxyl, carbonyl, GO membrane shows preferential water adsorption and fast water diffusivity [25, 29, 39]. Particularly, in recent years GO has emerged as a novel 2-D membrane material for water purification and desalination applications because of its hydrophilic nature and ease of formation of compact membrane structure [75, 76, 77, 78, 79, 80]. The single atom thickness of GO nanosheet bestows it with high aspect ratio which makes it easily stackable and self-assemblable [41, 81, 82, 83]. The presence of functional groups on the GO nanosheets, in particular carboxyl functional group, provide convenient sites for adding various functional groups to the GO nanosheets which can greatly affects the chemical and mechanical properties of the GO based membranes [84, 85, 86, 87, 88, 89]. This imparts GO with huge potential for making functional nanocomposite materials pertaining high chemical stability, strong hydrophilicity, and excellent antifouling properties and many more [39, 41, 90]. These exceptional properties make GO a potential candidate for high-performance membrane material for desalination and waste water treatment and it has been attributed with intriguing separation performance along with superior mechanical strength [13, 27, 39, 91, 92, 93, 94].

In a layered GO membrane, the interlayer spacing between two neighboring GO nanosheets provides routes for water permeation and also selectively rejects salts and other unwanted solutes depending on the size of this spacing [95, 96, 97]. The sizes of these interlayer spacings of layered GO membranes play an important role in determining the applicability and performance of the membranes in specific separation applications [29, 98, 99]. In graphite, the interlayer distance between the successive graphene sheets is around 3.4 Å. In GO membrane the interlayer distance between the GO nanosheet is larger than this because of the presence of the oxygen containing functional groups [17]. In dry conditions this interlayer distance is 7-9 Å. As the humidity increases the water molecules diffuse in to the interlayer space of the GO nanosheet of the layered GO membrane and accordingly the interlayer spacing

increases. When the layered GO membrane is immersed in water and completely wetted this interlayer spacing increases upto 12-13 Å [18, 19].

The highly selective nature of the GO membrane is mainly attributed to its structure [20]. The selectivity of the GO membrane is achieved by the size exclusion from the interlayer spacing, electrostatic interactions between the ions and the negatively charged GO nanosheets, cation-π interaction, metal coordination of the GO nanosheet and among others. Based on the selectivity pertained to the size exclusion from the interlayer spacing in the layered GO membrane, molecules and ions can be separated according to their hydrated radius[100]. Joshi *et. al.* [25] studied the penetration properties of molecules and ions of various sizes using a 5μ thick GO membrane.

In some of the previous studies [13, 100] the interlayer spacing between the GO nanosheet in hydrated GO membrane is reported as 9-10 Å. Because of this interlayer spacing, ions with a hydrated radius $>$ 4.5 Å are not able to permeate through GO membranes. Along with the hydrated radius of the anions/cations, their charge and its interaction with the GO nanosheets also play an crucial role in determining their permeability through the GO membrane. Sun *et al.* [101] reported the permeability of different anions through GO membrane in the following order NaOH $>$ $NaHSO_4$ $>$ NaCl $>$ $NaHCO_3$. For NaOH solution, the OH^- ions interact with the carboxyl and hydroxyl functional group of the GO nanosheets which makes the GO nanosheet highly ionize. Due to this, the electrostatic repulsion between the GO nanosheet increases which in turn increases the interlayer spacing between the GO nanosheets. With the increase in this interlayer distance the Na^+ ions and the OH^- ions can permeate through the GO membrane with relative ease. For $NaHSO_4$ solution the H^+ ion in the solution prohibits the ionization of carboxyl and hydroxyl functional group due to which the interlayer spacing between the GO nanosheet become relatively smaller leading to slow permeation of the ions. For $NaHCO_3$ solution the reaction between HCO_3^- and carboxyl group of the GO nanosheet produces CO_2 which greatly hinder the permeation of the ions through the membrane.

GO membrane is also been used to filter iron based electrolyte containing $FeCl_3$ and HCl [102]. This is based on the difference in the hydration radius of Fe^{3+} ion

and H^+ ion (hydration radius of Fe^{3+} ion is 4.57 Å and that for H^+ ion is 2.82 Å) and coordination interactions between Fe^{3+} ions and GO nanosheets. They reported that the permeation of H^+ ions is 2 times higher than that for Fe^{3+} ions through the GO membrane. They have also reported that the Fe^{3+} ions are completely blocked by the GO membrane when the concentration of $FeCl_3$ in the electrolyte is < 0.01 mol/L.

Due to the interactions between the cations and GO nanosheets small amount of metal cations remain trapped inside the GO membrane after the permeation operation (FO or RO) is over which is also detected experimentally. On the contrary the anions were not detected within the GO membrane after the completion of the permeation process because of the repulsive forces between the anions and negatively charged GO nanosheets (because of the presence of oxygen containing functional groups such as hydroxyl, epoxy, carboxyl etc.) [101, 103].

The water permeability and salt rejection performance of a GO membrane can aptly be tuned by choosing appropriate sizes of the GO nanosheets constituting the GO membrane. *Sun et al.* [102, 103] reported this using two types of GO membrane: one composed of nanosized GO sheets and the other one is composed of microsized GO sheets. The permeability of the ions and molecules are more through the GO membrane composed of nanosized GO sheets as compared to the GO membrane composed of microsized GO sheets. This is because, in the GO membrane composed of nanosized GO sheets, there are more gaps exist between the edges of noninterlocked neighboring GO sheets than in the GO membrane composed of microsized GO sheets. A larger number of gap means more diffusion of the ions and molecules through the GO membrane in the direction vertical to the GO sheets.

The separation performance of GO membrane also depends on the degree of ionization of the carboxyl and hydroxyl group of the GO sheets. The ionization of these functional groups makes the GO sheets more negatively charged which in turn affect the interactions of the GO sheets with ions and molecules. The degree of ionization can be controlled by choosing appropriate pH of water, and hence the separation performance of the GO membrane. *Huang et al.* [104] controlled the water permeability

and rejection rate of Evans Blue ($C_{34}H_{24}N_6Na_4O_{14}S_4$) through the GO membrane by adjusting the pH of water by adding sodium hydroxide and hydrochloric acid. They reported that with the increase in pH from 2 to 6 the zeta potential of the GO sheets decreases because of the increased degree of ionization of the carboxyl and hydroxyl groups. Due to this the electrostatic repulsion between the GO sheets increases, which in turn increases the interlayer separation between the GO sheets. With the increase in interlayer distance the water flux through the GO membrane increases and its salt rejection decreases. When the pH is in the range of $6-8$, there is very little variation of the zeta potential of the GO sheets. Thus there is no significant variation in the corresponding water permeability and salt rejection of the GO membrane. When the pH increased from 8 to 12 there is slight change in the zeta potential of the GO nanosheets. However, as the concentration of the Na^+ ions increases in the solution because of the addition of NaOH, the electrical double layer screening effect become more dominant. As a consequence, the interlayer distance between the GO nanosheets decreases which leads to a decrease in water permeability and increase in salt rejection rate through the GO membrane.

The interlayer distance of the GO sheets decreases with its reduction as it eliminates oxygen containing functional groups from the sheets. With the decrease in this interlayer distance, the selectivity of the GO membrane increases but at the cost of water permeability. *Nair et al.* [13] reduced the interlayer space of the GO membrane from 10 Å to 4 Å by reducing the GO sheets. They reduced the GO sheets by annealing it at 250 ^{0}C in a hydrogen-argon environment. They reported that with the decrease in this interlayer distance, the GO membrane become impermeable to water vapor.

Su et al. [105] prepared three different types of reduced GO membrane abbreviated as T-RGO (reduced the GO sheets through thermal reduction), VC-RO (reduced the GO sheets with vitamin C solution) and HI-RGO (reduced the GO sheets with HI acid vapor). For T-RGO and VC-RGO the interlayer spaces decreases up to 4 Å and for HI-RGO the interlayer space decreases up to 3.6 Å which is close to the interlayer space in graphite. Due to this decrease in interlayer spacing between the GO sheets,

the water permeation through T-RGO and VC-RGO membranes decreases to 3 and 5 order of magnitude, respectively, as compared to the original (one which is not reduced) GO membrane. For HI-RGO membrane no water permeation was detected due to the increasing barrier of the GO membrane resulted from decrease in interlayer spacing between the GO sheets.

Hu *et al.* [32] prepared a GO membrane through layer-by-layer deposition of GO nanosheets and cross-linking these GO nanosheets by 1,3,5-benzenetricarbonyl trichloride on a polydopamine-coated polysulfone support. This cross-linking provide stability to the stacked GO nanosheets as it reduces the inherent dispersibility of the GO nanosheets in aqueous environment. Along with this, it also fine-tuned the charge, functionality and spacing of the GO nanosheets. Heng *et al.* [34] reported the construction of GO membrane which exhibit extraordinary stability in water, acid and base solutions. They also reported regularly controllable lamellar spacing of layered GO membrane by doping lamellar nanostructure of GO membranes with partially reduced GO sheets. Joshi *et al.* [25] reported a interlayer distance of $9.0 - 10.0$ Å for a GO membrane of thickness 1.0 μm. Their experiment showed a water flux of 0.2 $Lm^{-2}h^{-1}$ to 1.0 M sucrose solution (osmotic pressure $\approx$ 25.0 bar) from a deionized water container. Jin *et al.* [37] reported the synthesis and application of polyamide cross-linked graphene oxide (PA-GO) membrane for forward osmosis applications. Their study suggested that as compared to the traditional ployamide (PA) membranes, PA-GO membrane shows reduced internal concentration polarization (ICP) which improves the separation performance of PA-GO membrane in FO applications. Soroush *et al.* [106] functionalized thin film composite (TFC) polyamide (PA) membranes with silver-decorated GO nanosheets for forward osmosis applications. They reported a synergistic effect of the combination of GO nanosheets and silver nanoparticles in the inactivation of bacteria without any adverse effects on membrane transport properties. Addition of GO nanosheets also imparts hydrophilicity to the PA TFC membranes.

Chen *et al.* [107] performed pressure-driven flow simulations to investigate the nature of interlayer flow between the GO sheets. They found that flow rate is neg-

atively correlated with oxide concentration and hydrogen interactions below a oxide concentration of 10.0 %. However, the flow rate is consistent at variable oxide concentration of high values. The effect of staggered nanoslits of layered GO membrane on desalination properties also been studied through MD simulations and hydrodynamic modelization on pressure-driven flow by Chen *et al.* [108]. They reported a parabolic relation between water flow rate with pore width through their MD simulations. They also reported ion permeability through GO membrane in the following order $K^+ > Na^+ > Mg^{2+} > Ca^{2+}$. Their study suggested that with the increase in pore offset distance and decrease in interlayer spacing the salt rejection ability of the layered GO membranes considerably increases. Dai *et al.* [109] performed MD simulations with layer-by-layer stacked GO membrane where the multilayer nanofluidic channels are almost parallel to the flow direction. Their study suggested that the interlayer distance between GO nanosheets varies from 5.5 Å to 12.4 Å depending on the water content. GO nanosheets with larger degree of oxidation shows more swelling of interlayer spacing. Their study showed a water permeability of around 850 L $m^{-2}h^{-1}bar^{-1}$ with a interlayer spacing of 12.4 Å. Chen *et al.* [110] also investigated the mechanism of water flow confined in GO laminations with different oxide concentrations. There is a logarithmic increase of the diffuse reflection coefficient with the change in oxide concentration. With the increase in oxide concentration water molecules tend to be absorbed on the GO surfaces resulting in the shrinkage of the effective passageway of water flow. Ban *et al.* [111] proposed an all-atom model of GO with agglomerated hydroxyl/epoxy groups which is in line with density functional theory (DFT) data and experimental characterization of GO surfaces. In the interlayer gallery of GO laminates, they have identified three types of water species: bonded water that binds tightly to oxygen functionalities at low humidity, confined water with movement obstructed by bonded water clusters and free water well-separated from oxidized surfaces of expanded GO. They also reported the increase in water diffusivity with the increase in interlayer distance between the GO sheets. Wei *et al.* [112] reported that the fast flow of water across graphene-derived membranes attributed mainly to the porous microstructures (e.g., expanded interlayer gallery, wide channels formed

at wrinkles, holes, and interedge spaces) followed by less significant enhancement by boundary slip.

3.1.2 Forward Osmosis (FO)

Considering the present scenario of water scarcity around the globe, desalination of sea water could be one of the ways we can look forward to meet the future demands of usable water. Currently, reverse osmosis (RO) is the most widely used method for seawater desalination. Several RO plants have already been established in some parts of the world for sea water desalination to address the scarcity of usable water. Even though the two decades of research and innovation, resulted in the significant reduction of the energy requirements of RO process, it is still associated with high operational energy consumption and irreversible membrane fouling [113]. Another proposed solution (as an alternative to RO) to the sea water desalination/waste water treatment is the forward osmosis (FO) process. While RO is hydraulically driven, FO is osmotically driven which could make FO an environment friendly and energy efficient process depending on the nature of feed to be treated and the technology of draw solute regeneration.

In FO, the net driving potential for water molecules through the semipermeable membrane is the osmotic pressure difference between the draw solution and the feed solution. The water molecules permeated through the membrane from the feed solution to the draw solution as the draw solution osmotic pressure is higher than the feed solution. Nevertheless, though FO bears a huge potential as a green and sustainable technology for global water crisis, its industrial application is still limited by the lack of optimal membrane and draw solutions [114]. However from the past decade FO has been gaining a tremendous research interest. The use of FO membrane for concentrating dilute wastewater has already been demonstrated on a pilot-scale [115]. Saren *et. al* [116] investigated the performance of layer by layer structure of a polyelectrolyte membrane for FO applications. Similarly microporous inorganic silica membrane showed efficient water permeation and good selectivity toward NaCl at ambient temperature [117]. Qi *et. al* [118] investigated the performance of porous

ultrafiltration-like membrane in FO applications. Membrane fouling is an another important issue for FO membrane [119]. Bell *et. al* [120] investigated the performance and fouling mechanisms of commercial cellulose triacetate membrane and polyamide thin film composite membrane in a FO process . The performance of cellulose triacetate membrane was found to be much higher as compared to polyamide thin film composite membrane. Liang *et. al* [121] used vertically oriented porous substrates (VOPSs) as supports for reducing the internal concentration polarization of thin film composite membrane for FO applications. This method showed higher water permeability as compared to the conventional phase inversion method. It is also observed that some of the commercially available FO membranes are prone to membrane fouling due to relatively hydrophobic nature of the membrane material. There is also an issue of low water flux with these membranes due to unfavorable membrane structure [113].

GO could be a suitable membrane material for FO applications. As GO is highly hydrophilic in nature due to the presence of carboxylic groups, it has been used as a coating material to improve the fouling resistance and permeability of the FO membrane. Increasing the hydrophilicity of the substrate also enhances the water transport and antifouling behavior of the membrane [122]. Since layered GO membrane can be produced in large scale with a lower production cost they have a huge potential in the application of water treatment [104, 123], water desalination, anti-corrosion, chemical resistance, controlled release coating [17], gas separation [13], pervaporation [29] and so on.

3.1.3 Dehydration of Acetic Acid

Layered GO membrane also has potential applicability in various process plants and industrial separation activities. One of the crucial separation process in various industrial plants is acetic acid separation. The processes/methodologies which are extensively studied or being used for the separation of acetic acid can be broadly classified into two categories: conventional distillation and membrane based separation. The conventional distillation processes are very energy intensive, although

new methodologies and techniques have been adapted (such as azeotropic distillation, extractive distillation) to reduce the energy consumption in these processes [124, 125, 126, 127, 128].

On the other hand the membrane based separation processes for acetic acid dehydration can be classified into two categories:

- Thermally driven membrane separation processes which includes pervaporation (PV), membrane distillation etc.
- Pressure driven membrane separation processes which includes nanofiltration (NF), reverse osmosis (RO) etc.

Zhang *et al.* [129] prepared a composite membrane by casting sodium alginate (NaAlg) solution onto a microporous polypropylene membrane (MPPM) for dehydration of acetic acid. Sano *et al.* [130] investigated the performance of polycrystalline silicalite membranes for dehydration of acetic acid through pervaporation process. They considered the concentration of feed acetic acid within the range of 5 to 40 vol.%. Grzenia *et al.* [131] had used hollow fibre-based liquid extraction to remove acetic acid from lignocellulosic hydrolysates after pretreatment of the same with dilute sulphuric acid. Polyaniline membranes and Polyphenylsulphone based polymeric membranes also been investigated for the dehydration of acetic acid [132, 133, 134, 135]. Alghezawi *et al.* [136] investigated the pervaporation separation of acetic acid-water mixture over a range of $10 - 90$ $wt.\%$ acetic acid using acrylonitrile (AN) grafted poly(vinyl alcohol) (PVA) membranes. Wang *et al.* [137] evaluate the potential use of a composite membrane of polyacrylic acid (PAA) dip-coated asymmetric poly(4-methyl-1-pentene) (TPX) membrane for the separation of water-acetic acid mixtures through pervaporation. They reported that the water concentration of permeate approach to 100 $wt.\%$ and a permeation rate of 960 g/m^2h with a 3 $wt.\%$ feed acetic acid concentration at 25 ^{0}C. Chen *et al.* [138] demonstrate the use of mordenite zeolite membrane for dehydration of acetic acid through pervaporation. They show that functional defect-patching can improve the pervaporation performance of mordenite zeolite membrane. Afonso [139] investigated the performances NF and RO

membranes for the concentration of acetic acid, where he reported 89 % retention of acetic acid with a flux of about 28 $kgm^{-2}h^{-1}$. Teella *et al.* [140] studied the feasibility of NF and RO membranes in removing small organic acids from the aqueous fraction of fast pyrolysis bio-oils with a feed concentrations, ranging as high as 34 $wt.\%$.

Over the years, research community is looking for separation and purification processes which are more energy efficient and less deleterious to the environment. Recently forward osmosis (FO) process has been emerging as an eco-friendly and less energy intensive alternative for purification and separation applications. The membrane used in the dehydration process of acetic acid (or any organic acid) should be compatible with the acidic environment. In that aspect GO can be a suitable candidate considering the fact that GO has inherent stability in acidic medium [34, 141, 142]. On the other hand its inherent hydrophilicity due to the presence of carboxyl functional groups gives GO membrane another edge in terms of membrane fouling resistance and antimicrobial activity [20]. These properties accentuated the potential use of GO as FO membrane for dehydration of acetic acid (or carboxylic acids). Xu *et al.* [142] deposited graphene oxide (GO) layer as an acid resisting barrier on zeolite LTA membrane for dehydration of acetic acid through pervaporation. Lecaros *et al.* [141] tuned the interlayer spacing of graphene oxide membrane by the intercalation of Poly(vinyl alcohol) (PVA). They reported an outstanding pervaporation performance of their membrane at 80.0 ^{0}C with a permeation flux of 463.9 $gm^{-2}h^{-1}$ and water concentration in the permeate of 97.7 %. Ruprakobkit *et al.* [143] used 10 mM acetic acid as the feed solution and 1 M NH_4Cl as the draw solution for their experimental modeling and simulation of dehydration of carboxylic acid through FO process. They have used thin-film composite (TFC) membrane and embedded polyester screen support (TFC-ES Membrane) in their study.

3.1.4 Electro-Osmotic Flow (EOF)

Apart from osmotic pressure gradient (e.g. FO) and hydraulic pressure gradient (e.g. RO), flow in the micro and nanoscale regime can also be induced by applying an external electric field. The motion of an electrolytic solution (or ionized solution)

along a stationary charged surface under the influence of an external electric field is termed as electro-osmotic flow (EOF). Typically it is a nanoscale induced transport phenomena. In the micro and nano scale regime, it is easier to control electrokinetic transport and also it scales more favourably as compared to other fluidic transport mechanism in that small scale regime [144, 145]. In an EOF, the volumetric flow rate between two parallel plates varies linearly with the channel height. On the other hand in a pressure driven flow, the volumetric flow rate scales with the cube of the channel height. As a consequence, in EOF, practical flow rates can be achieved with relatively low electric field instead of applying huge pressure drop across the channel. EOF induced by locally applied electric field eliminates the need of pumps and valves with moving mechanical components. This imparts easy controllability of an EOF in micro and nanochannels [146]. At the same time it is relatively easier to integrate electric and fluid flow circuit in nano and micro scale devices for specific applications. In other words, as compared to other fluidic transport mechanisms, electrokinetic transport provides a relatively easier and efficient mean for regulating the fluid flow in the nano and microscale devices. This controllability in EOF flow makes it possible to develop nanoscale fluidic system for various applications e.g healthcare, drug delivery, microscale cooling system etc. [147, 148].

With the gradual advancements in the nano-biotechnology and lab-on-a-chip devices, electro-osmotic transport has gained a considerable interest from the the research community over the years [147, 149, 150, 151, 152, 153, 154, 155, 156, 157, 158, 159, 160, 161, 162, 163, 164, 165, 166, 167, 168, 169, 170, 171, 172, 173]. A precise understanding of the flow behaviour in electrokinetic transport in miniature sysems is of utmost importance for variety of applications including fuel cell, energy storage devices, separation and purification applications, biological applications and subsurface flow [174, 175, 176, 177, 178, 179, 180, 181, 182, 183, 184, 185, 186, 187, 188, 189, 190]. Apart from these, EOF also finds its potential applicability in various micro and nanofluidic devices for transporting and controlling liquid flows for applications such as drug delivery, micro and nano pumps, geoscience, development of synthetic nanopores as biomolecules sensors, development of thin flims for water purification and desali-

nation applications [145, 147, 160, 164, 165, 169, 191, 192, 193, 194, 195, 196, 197, 198, 199, 200].

The modeling and simulation of electrically modulated fluid transport in the micro and nanoscale regime can aid in the understanding of many critical aspects in the designing and fabrication of micro and nanofluidic devices [148]. Over the years different models and theories have been proposed to describe the ion distribution and flow behaviour in an electro-osmotic transport. The analytical models of EOF are based on Poisson-Boltzmann (PB) and Stokes (S) equations. In these continuum approaches, the ionic solutions are modeled as continuous media with constant viscosity. These approaches often neglect the layerings at the solid-liquid interface, finite sizes of the molecules, exact location of the wall and hydrodynamic slip plane. For instance, in the classical Poisson-Boltzmann equation, ions are considered as infinitesimal species and the various atomic and molecular interactions (e.g. ion-ion, ion-water, ion-wall etc.) are modeled in a mean-field fashion. Also, it does not take account of the fluctuations in the fluid density near the wall boundary. On the same note, Navier-Stokes equations have the critical assumption that the state variables such as density are invariant over intermolecular distances and the shear stress and local strain rate can be related with linear constitutive relationship. But, previous atomistic and experimental investigations reported considerable fluctuations in the fluid density near the solid wall [201, 202].

In any nanoscale fluidic system the surface to volume ratio is very high and its characteristic dimension is comparable to the size of its constituting atoms and molecules. Also, for such system, the thickness of the EDL are of the same order to that of the channel dimensions. So, the finite size effect of the molecules (which is neglected in classical continuum approaches) may play an important role in determining the ion distribution and flow field in a nanochannel. As a consequence, most of the classical models are unable to capture the flow behaviour in a electro-osmotic transport as observed in experimental and atomistic simulation investigations [144, 203, 204, 205, 206, 207, 208, 209, 210, 211, 212, 213, 214]. Although the classical PB equation can capture the flow dynamics of EOF with reasonable accuracy for low

surface charge density [215], it fails to capture the flow dynamics for system with high surface charge density and high ion valency [216]. In the classical continuum theories, EOF is captured as a plug like flow with no-slip boundary condition at the solid surface [217]. However, in practical scenarios, there is hydrodynamic slip at the solid-liquid interface in EOF [218, 219]. As the size of the flow channel reduces to micro/nano scale, hydrodynamic slip at the slid-liquid interface become critical in determining the flow characteristics and can not be neglected trivially [220, 221, 222]. For a wide range of materials, the boundary conditions for the water flow is characterized by the slip length especially on highly hydrophobic surfaces [223, 224, 225, 226]. Previous experimental investigations revealed that the flow rates predicted by using no-slip boundary conditions in hydrophobic microfluidics systems were not in accordance with the experimental observations [227, 228]. This slip on the channel surface leads to significant increase in the electrokinatic transport [162, 223, 229, 230, 231] and it has been reported that a slip length of 50 nm increases the efficiency of nanofluidic devices from 3% to 70% [184, 232].

Moreover, some of the crucial non-trivial phenomena in electrokinetic transport, such as charge inversion are beyond the scope of classical continuum theories [203, 209, 215, 233, 234, 235, 236, 237, 238]. The charge inversion phenomenon comes into picture when an excessive amount of counterions adsorbed at the stern layer to the extent that it exceeds the value of the surface charge. As a consequence, the co-ion charge density becomes higher than the counterion charge density in the diffuse layer [239]. Because of this charge inversion in the diffuse layer, a reverse EOF develops in the channel under the applied electric field [209, 215, 240]. With the increase in surface charge density, the reverse EOF velocity also increases [215]. These observations can not be captured with PB theory [239]. Previous MD simulations also reveal the discrepancies in the ion-distribution between atomistic simulations and PB theory [144]. Although there are attempts to modify the classical theories with new approximations and models, they still may not be complete enough to capture the flow dynamics in electrokinetic systems with complex geometries and surface properties [241]. In that aspect MD simulation can be a suitable tool for studying the flow

dynamics in electrokinetic transport in nanoscale regime. In MD simulations all the atomistic and molecular interactions can be modeled explicitly.

Surface charge plays an important role in determining many flow parameters in EOF [155, 170, 208, 215, 242]. With the increase in the surface charge, the surface wettability increases due to stronger interaction between the wall and the counter ions/water molecules [243]. Because of this, the number of molecules (counter ions/water molecules) near the liquid-solid interface increases [170, 243]. The variation in surface charge also significantly affect the orientation of the water molecules and hydrogen bond dynamics [244, 245, 246, 247, 248, 249, 250]. With the rapid progress of nano-engineering, charged solid-liquid interfaces are observed in variety of applications starting from nano and micro devices to batteries and colloidal systems. It opens up a whole lot of opportunities in the design and fabrication of smart surfaces with specific surface properties for specific applications [251, 252]. These smart surfaces can play a vital role in applications like data storage device, drug delivery system, microelectronics etc. Today's nano-engineering makes it possible to construct cost effective nano-membrane with specific surface properties for water purification and desalination applications [15, 253]. Previous studies reported the control of electrokinetic transport by interplaying the interfacial hydrodynamics through chemical or physical patterning on the surface of the wall [254, 255, 256, 257]. It is also possible to procure surface with patterned surface charge distribution in nano-scale devices to get the desired functionalities [145, 258, 259, 260, 261, 262, 263, 264]. Surfaces with patterned charge distribution have their potential applicability in various fields such as induced charged electro-osmosis, AC-electro-osmosis, thin-film patterning, electrothermal flow actuations etc. [265, 266, 267, 268, 269, 270, 271, 272]. To realize this in practice, adequate understanding of the flow dynamic behaviour is of utmost importance. However, the interactions between the charged surface and the fluid molecules/ionic species are yet to be understood and explored in detail. Similar is the scenario for the dynamics of EDL. The interfacial hydrodynamics in the presence of patterned surface charge density is far from being trivial and the classical continuum approaches may not be sufficient enough to capture the flow dynamics of the electroki-

netic transport. To investigate these issues, MD simulation can be a promising tool, as this in silico approach provides greater temporal and spatial resolutions with better control on the system parameters [144, 162, 167, 205, 234, 273, 274, 275, 276, 277, 278].

3.2 Objectives

The primary objective of this study is to get a detail atomistic insight into the applicability of graphene and graphene oxide (GO) for membrane applications. So, based on the literature survey following problems are formulated and solved as a part of this PhD dissertation work:

- Considering the rapid growth in the global water crisis, sea water desalination could be a suitable long term solution in the days to come. Some of the developed Countries like Israel, United State have already started sea water desalination plant to address the issue of water scarcity. However, most of these plants are RO plants. Considering the inherent energy requirement in a RO process, researchers are looking for alternative less energy intensive processes. In that aspect FO process could be an suitable process for sea water desalination. Apart from this, most of the presently available membranes are polyamide membrane which are susceptible to low fouling resistance, low water permeance etc. Membrane materials are important in determining the process performance. Recently, graphene and graphene oxide (GO) has emerged as a promising membrane material for separation and purification applications. Considering this, the applicability of layered GO membrane for seawater desalination using FO process is investigated with non-equilibrium MD simulations. The methodology and observations of this investigations are reported in Chapter 4.

- Dehydration of acetic acid is one of the major processes in chemical industries and is often energy intensive. Since FO is an osmotically driven process it could be a suitable alternative to the energy intensive conventional dehydration processes of acetic acid. The membranes which are used in the dehydration

process of acetic acid should be stable in acidic medium. Since GO is prepared by the strong oxidation of graphite in acidic medium, it has inherent stability in acidic medium. So, the dehydration process of acetic acid using FO process with layered GO membrane is investigated and is reported in Chapter 5.

- Although GO has huge potential applicability in membrane separation processes, its industrial applications are still far from reality. One of the major issue of layered GO membrane is its undesirable swelling in aqueous environment. Recently, it is proposed that intercalation of cations can impart stability to layered GO membranes in aqueous environment [31, 279, 280]. To get a more detailed insight into the effect of the presence of the cations on the water and ion dynamics inside layered GO membrane, non-equilibrium MD simulations are performed. The detail methodology and observations of this investigations are reported in Chapter 6.

- As reported earlier, in the nanoscale regime, it is easier to control fluid flow through electrokinetic transport as compared to other fluidic transport mechanism. Considering the potential applicability of graphene nanocapillaries in various separation and purification applications, electro-osmotic flow behaviour through a rectangular graphene nanochannel is investigated using non-equilibrium MD simulations. The detail of this electro-osmotic flow simulations and the observations are reported in Chapter 7.

Chapter 4

Multilayer Graphene Oxide Membrane in Forward Osmosis: Molecular Insights[1]

4.1 Introduction

As discussed in Chapter 1, water is one of the most important and essential element for sustaining life on our planet earth. Apart from drinking, it interacts with every other aspect of other life sustaining sub-systems like agriculture and energy. With the rapid progress of human civilization and growing population, the demand of usable fresh water is also increasing. Although almost 70 % of our planet is covered with sea, the availability of usable water is very less (only about 0.3 %). This scenario become even worse, when the increasing environmental pollution around us is taken into account.

Sea water desalination could be a long term solution to the global water crisis and in this chapter the applicability of layered GO membrane for seawater desalination using FO process is investigated with non-equilibrium MD simulations. Previous simulation studies on layered GO membrane were performed mainly in RO mode

[1] A. Gogoi, K. A. Reddy, and P. Mondal. Multilayer graphene oxide membrane in forward osmosis: Molecular insights. *ACS Appl. Nano Mater.*, 1(9):4450-4460, 2018.

and in those simulations only hydroxyl or epoxy functional groups are considered for the modeling of the GO nanosheets [107, 108, 109, 110, 281]. However, along with the hydroxyl and epoxy functional groups, GO nanosheets also contain carboxyl functional groups which are mainly located at the edges of the GO nanosheets [5, 46].

In the present work, we consider carboxylic functional group along with the epoxy and hydroxyl functional groups for the modeling of the GO nanosheets and our study suggested that carboxylic functional group also plays and important role in the dynamics of water molecules and ions while permeating through the layered GO membranes. Although GO nanosheets have previously been employed as a coating material to improve the functionality of thin-film composite (TFC) FO membrane [282], the influence of internal structure of GO on the membrane performance has not been addressed in the FO mode. We aim to address this question with the help of large scale fully atomistic simulations by considering three different membrane configurations where each configuration has a different pore offset distance (**W**). The dynamics of water molecules, pathways of water/ions inside the membrane and membrane performance are discussed in detail to have an atomistic insight of layered GO membrane in FO applications.

4.2 Methodology

4.2.1 Model Construction

Typically there are 3 major components in a FO process: feed solution, a semipermeable membrane and draw solution. The semipermeable membrane separates the feed solution from the draw solution and the osmotic pressure of the draw solution is higher than the feed solution. This difference in osmotic pressure acts as a driving potential for the water molecules to permeate through the semi permeable membrane from the feed solution to the draw solution side. In this present work layered GO nanosheets are considered as a membrane. For this, 4 different sizes of GO nanosheets are constructed using the model proposed by Lerf and Klinowski [24]. The sizes of

the GO nanosheets are as follows:

- 20.0×49.0 Å^2
- 30.0×49.0 Å^2
- 40.0×49.0 Å^2
- 50.0×49.0 Å^2

The epoxy and hydroxyl groups are located on the basal plane of the GO nanosheet, while the carboxylic groups are located on the edges. We did not consider any pore in the GO nanosheet. The chemical composition of this GO nanosheet is $C_{10}O_1(OH)_1(COOH)_{0.5}$ [46, 5]. With these GO nanosheets as the constructing unit, 3 different configurations of GO membranes are modeled as shown in Figure 4-1. In all the three configurations the initial interlayer distance (**H**) and the dimension of the pores (**D**) are 10.0 Å [13, 18] and 7.0×49.0 Å^2 respectively. However these three membrane configurations differ in their pore offset distance (**W**). For configuration-1 **W** = 25.0 Å (Figure 4-1a), for configuration-2 **W** = 8.0 Å (Figure 4-1b) and for configuration-3 **W** = 0 Å (Figure 4-1c). In other words for configuration-3 the pores of the respective GO layers in the membrane are perfectly aligned. Form an experimental point of view configuration-1 can be considered as GO membranes composed of GO nanosheets of very large lateral dimensions, configuration-2 refers to GO membranes composed of GO nanosheets of medium lateral dimensions, whereas configuration-3 resembles GO membranes consisting of GO nanosheets of very small lateral dimensions [35, 102].

4.2.2 Simulation System

After the membranes were constructed they are properly hydrated by solvating them in a water box of size $77.0 \times 49.0 \times 55.0$ Å^3 (Figure 4-2a). All the water molecules within 2.0 Å distance from the GO sheets are removed. The total number of water molecules in this solvating water box are 6500. To mimic the osmotic pressure of seawater (27.0 atm) a 0.56 molar solution of sodium chloride (NaCl) is considered

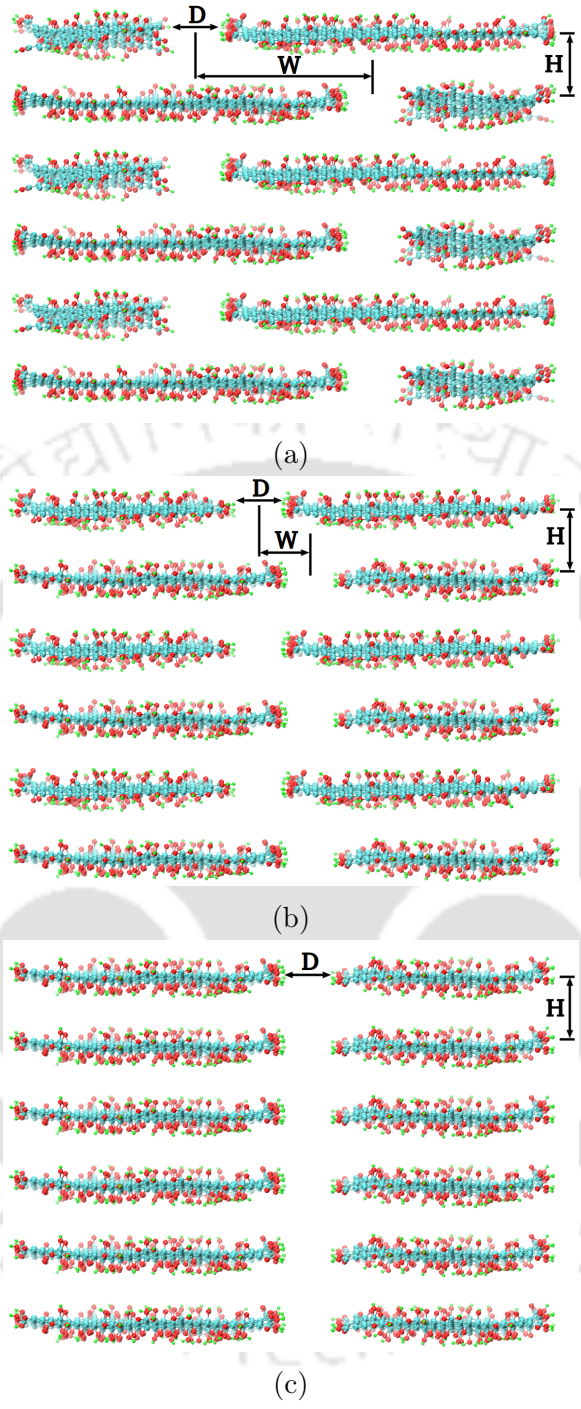

Figure 4-1: The three membrane configurations (a) Configuration-1 (b) Configuration-2 (c) Configuration-3. The green color is for hydrogen atoms, the red color is for oxygen atoms and the cyan color is for carbon atoms.

as the feed solution. This 0.56M NaCl solution contains 10000 water molecules, 108 Na^+ ions and 108 Cl^- ions (Figure 4-2b). A solution of 1.0 M $MgCl_2$ and 0.05

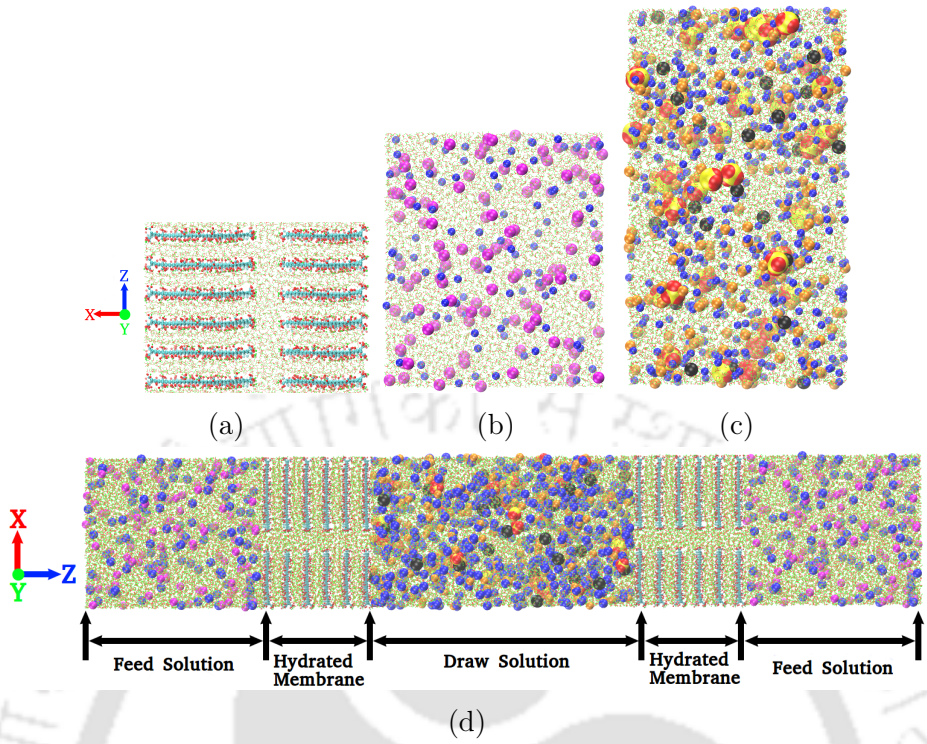

Figure 4-2: (a) Hydrated membrane (configuration-3) (b) Feed solution (c) Draw solution (d) Simulation setup. The green color is for hydrogen atoms, the red color is for oxygen atoms, the cyan color is for carbon atoms, the blue color is for Cl^- ions, the magenta color is for Na^+ ions, the orange color is for Mg^{2+} ions, the black color is for Al^{3+} ions, the yellow color is for sulfur atoms.

M $Al_2(SO_4)_3$ is considered as the draw solution [283]. This draw solution contains 15000 water molecules, 246 Mg^{2+} ions, 492 Cl^- ions, 26 Al^{3+} ions and 39 $(SO_4)^{2-}$ ions (Figure 4-2c). For the simulation system the draw solution box is placed in between the two hydrated membranes and the feed solution boxes are placed ouside the membranes as shown in Figure 4-2d. This type of FO configurations are simulated successfully by Raghunathan and Aluru [284].

4.2.3 Simulation Methodology

We performed all the non-equilibrium MD simulations using NAMD 2.11 [285] employing OPLS-AA force field [45] with a time step of 1.0 fs. For the water molecules TIP3P water model is used [286]. The bond length of the water molecules are con-

strained using SETTLE algorithm [287]. The van der Waals interactions are calculated through Lennard-Jones potential with a cut-off distance of 12.0 Å. For the calculation of the long range electrostatic interactions, Particle mesh Ewald (PME) method is implemented [288].

After the simulation system was constructed, energy minimization was performed to remove any internal stress within the system. After that, the system was equilibrated for 1.0 ns at a temperature of 300.0 K and 1.0 atm pressure. Then the production runs of the non-equilibrium MD simulations were carried out for 25.0 ns in a NPT ensemble with periodic boundary condition (PBC) in all the directions for configuration-1 and configuration-2. However to get a better insight of the water permeability and salt rejection of the membrane, the production run for configuration-3 was carried out for 64.0 ns with the same set of parameters as for configuration-1 and configuration-2 (i.e. NPT ensemble with PBC in all directions). Simulation data were saved at every 20.0 ps. During the simulations the temperature was held constant using Langevin dynamics with a damping factor of 5.0 ps^{-1}. Pressure was kept constant using modified Nosé-Hoover method where barostat oscillation time and damping factors both were set to 0.3 ps.

Previous simulation studies on layered GO membrane were performed mainly in RO mode and in most of those simulations GO sheets are constrained in all the three (X, Y, Z) directions. However, these kind of constrains are not there in an experiment. So, to have a better resemblance to the experiments, in this study we constrained the GO nanosheets only in the XY plane. We did not apply any constrain to the membrane in the Z direction (permeating direction). This allows the GO nanosheets of the membrane to move (or fluctuate) in the Z direction during the course of the simulations. We apply harmonic constrain to all the carbon atoms of the GO membranes in the XY plane, so that the layered structure of the GO membranes are retained throughout the simulations with predefined value of $\mathbf{W}$ for each configurations. This allows us to effectively study the effect of internal structure of the layered GO membrane on is performance. The carbon atoms of the GO membranes are constrained in the XY plane with a force constant of 1.0 $kcal/(mol$ Å$^2)$. For each of the 3 mem-

brane configurations 3 independent simulations are performed with different initial configurations (or initial arrangements of atoms) and the results are averaged over the 3 simulations for each of the membrane configurations.

4.3 Results and Discussion

4.3.1 Water Dynamics

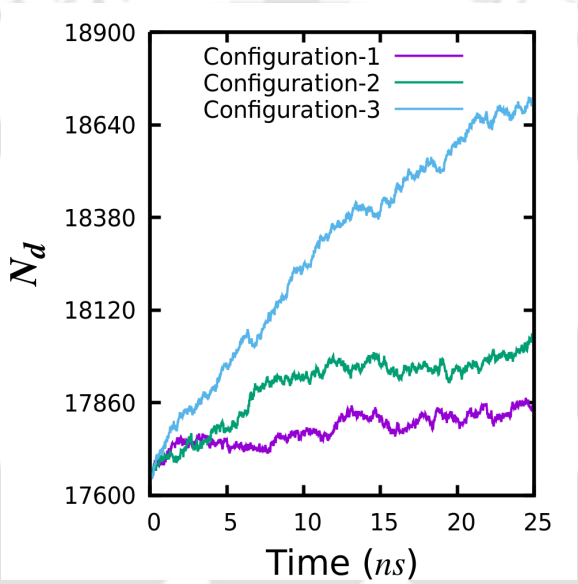

Figure 4-3: Variation of the number of water molecules in the draw solution box ($\boldsymbol{N_d}$) with time.

Using non-equilibrium MD simulations, we computed the number of water molecules permeated through the membranes for each of the three configurations. The draw solution used in the current study (1 M $MgCl_2$ + 0.05 M $Al_2(SO_4)_3$ aqueous solution) has an osmotic pressure of 80.0 atm which is much higher compared to osmotic pressure of sea water (which is equal to osmotic pressure of a 0.56 M NaCl solution or 27.0 atm). Due to this difference in osmotic pressure between the draw solution and the feed solution, there will be a net flow of water molecules ($\boldsymbol{N_p}$) from the feed solution to the draw solution. $\boldsymbol{N_p}$ for configuration-1 is 187, for configuration-2 it is 380 and for configuration-3 it is 1793. Since we are employing same combination of

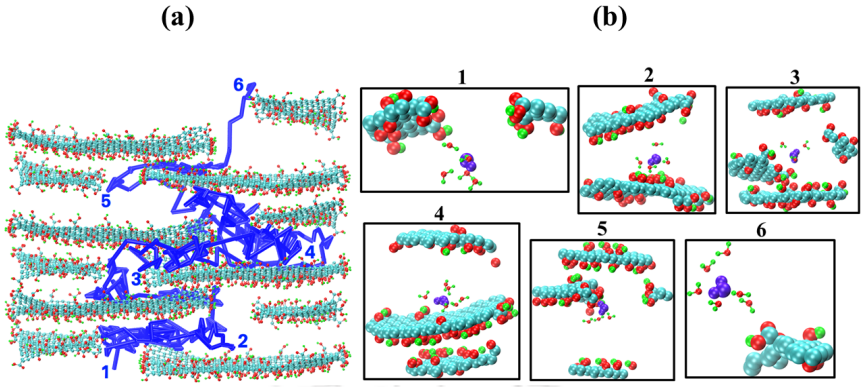

Figure 4-4: (a) Trajectory of the water molecule inside the layered GO membrane of configuration-1. (b) The number of water molecules in the hydration shell of water at various positions while permeating through the membrane. The permeated water molecule is shown in violet color. Red color is for oxygen atoms, green color is for hydrogen atoms and cyan color is for carbon atoms.

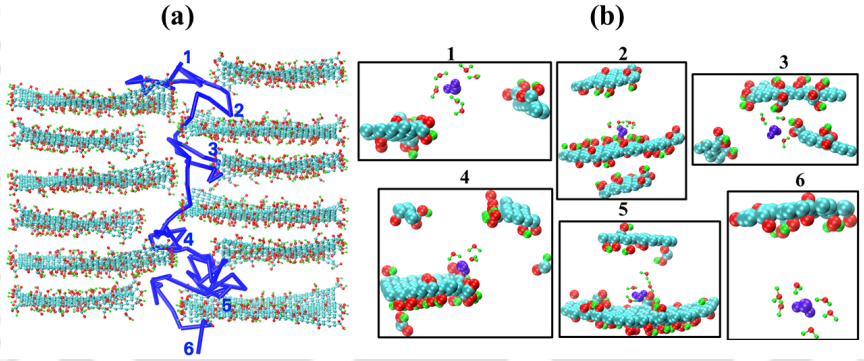

Figure 4-5: (a)Trajectory of the water molecule inside the layered GO membrane of configuration-2. (b) The number of water molecules in the hydration shell of water at various positions while permeating through the membrane. The permeated water molecule is shown in violet color. Red color is for oxygen atoms, green color is for hydrogen atoms and cyan color is for carbon atoms.

draw and feed solution in all the three membrane configurations it is obvious from this observation that the water permeability for configuration-3 is higher followed by configuration-2 and configuration-1.

Figure 4-3 shows the variation of the number of water molecules in the draw solution box, $\boldsymbol{N_d}$ with time. As the simulation progresses the water molecules from the feed solution permeate through the membrane towards the draw solution due to the osmotic pressure difference. As a consequence, the number of water molecules

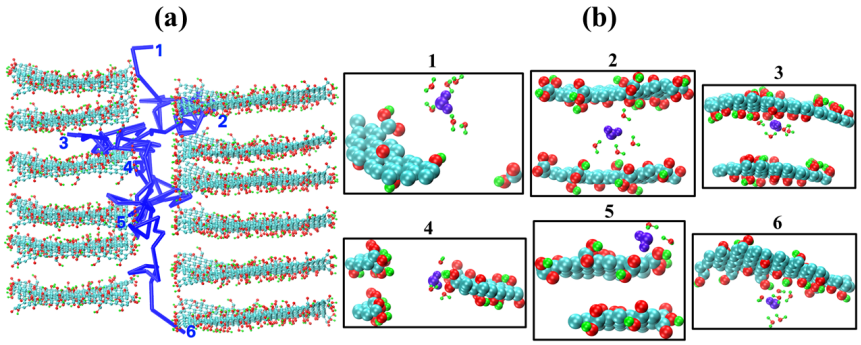

Figure 4-6: (a) Trajectory of the water molecule inside the layered GO membrane of configuration-3. (b) The number of water molecules in the hydration shell of water at various positions while permeating through the membrane. The permeated water molecule is shown in violet color. Red color is for oxygen atoms, green color is for hydrogen atoms and cyan color is for carbon atoms.

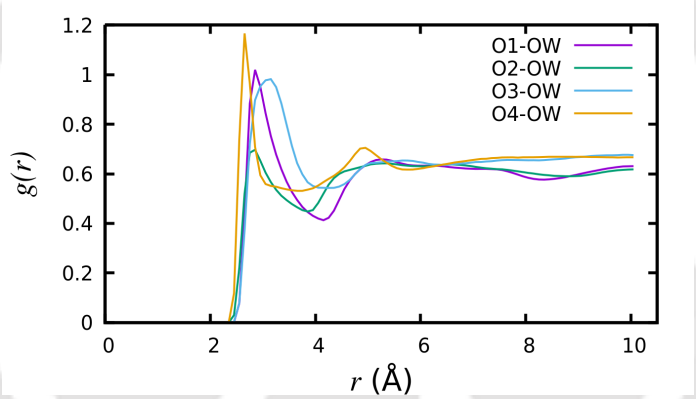

Figure 4-7: Radial distribution function between oxygen atoms of the functional groups present in GO and oxygen atoms of water. O1 is oxygen atom of hydroxyl group (-OH), O2 is the oxygen atom of epoxy group (-O-), O3 is the oxygen atom of the carboxyl group which is bonded to only C atom (-C=O), O4 is the oxygen atom of carboxyl group which is bonded to H and C atom (C-O-H) and OW is the oxygen atom of water.

in the draw solution box increases. However this increase is more for configuration-3 followed by configuration-2 and configuration-1 (Figure 4-3). So this observation also suggests that GO membrane with configuration-3 has higher water permeability followed by configuration-2 and configuration-1. In other words with the increase in **W** the water permeability of the layered GO membrane decreases. In the initial stage of the FO process $\boldsymbol{N_d}$ increases linearly with time. However, as the simulation

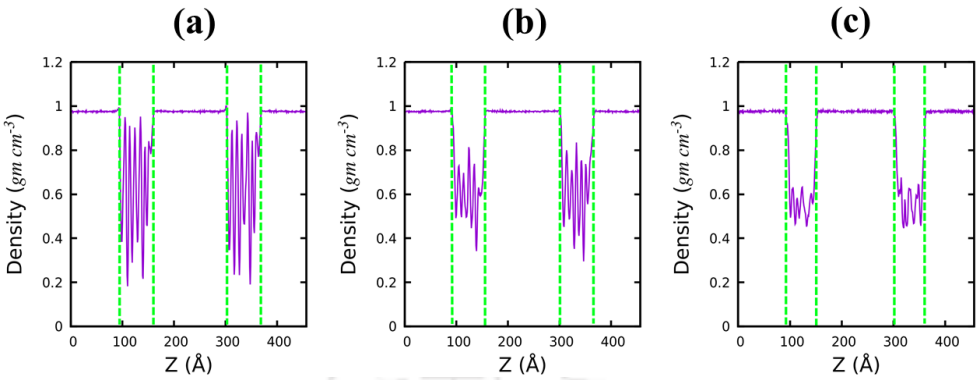

Figure 4-8: Density of water molecules along the Z direction. (a) configuration-1 (b) configuration-2 (c) configuration-3. The positions of the two membranes are shown by two pair of dotted green lines.

progresses this linear relationship gradually vanishes because of the dilution of the draw solution and increase in concentration of feed solution.

Figure 4-4a, Figure 4-5a and Figure 4-6a depict the trajectory of a representative water molecule inside the layered GO membranes for configuration-1, configuration-2 and configuration-3 respectively. The water molecule follows a straighter pathway inside the layered GO membranes for configuration-3 (Figure 4-6a) as compared to configuration-2 (Figure 4-5a) and configuration-1 (Figure 4-4a). So the tortuosity is higher for configuration-1 followed by configuration-2 and configuration-3 as the pathways inside the membranes are more "zig-zag" for configuration-1 followed by configuration-2 and configuration-3. Again in terms of porosity we can consider configuration-1 to be poorly sorted, configuration-2 to be medium sorted and configuration-3 to be well sorted. This is evident from Figure 4-1, where for configuration-3 the GO nanosheets consisting the layered GO membrane are almost similar in size. For configuration-1 there is a considerable difference in size of the GO nanosheets followed by configuration-2. These parameters are very much important for a typical FO membrane. Along with the water trajectory through the membranes, we also compute the number of water molecules inside the hydration shell of a permeating water molecule at various locations during permeation as shown in Figure 4-4b, Figure 4-5b and Figure 4-6b for configuration-1, configuration-2 and configuration-3

respectively. For this analysis the radius of the hydration shell of permeating water molecule is considered as 2.75 Å. Water molecules within 2.75 Å from the center of the permeating water molecule are shown in ball and stick representations (VMD). Atoms of the GO membrane within 12.0 Å from the center of the permeating water molecule are shown in VDW representations (VMD). The number of water molecules in the hydration shell of the permeating water molecule is more outside the membrane i.e. in the bulk solution, (position 1 and 6 in Figure 4-4b, Figure 4-5b and Figure 4-6b for configuration-1, configuration-2 and configuration-3 respectively) as compared to inside the membrane (position 2, 3, 4 and 5 in Figure 4-4b, Figure 4-5b and Figure 4-6b for configuration-1, configuration-2 and configuration-3 respectively). Again inside the membrane, near the edges of the GO nanosheets (position 3 and 5 in Figure 4-4b, position 3 and 4 in Figure 4-5b and position 4 and 5 in Figure 4-6b) the number of water molecules in the hydration shell of the permeating water molecule is less as compared to the positions near the basal plane of the GO nanosheets (position 2 and 4 in Figure 4-4b, position 2 and 5 in Figure 4-5b and position 2 and 3 in Figure 4-6b). This variation of number of water molecules in the hydration shell of the permeating water molecule can be attributed to the interactions between water and the oxygen containing functional groups present in the GO nanosheets. Figure 4-7 shows the radial distribution function between the oxygen atoms of the functional groups present in the GO nanosheets and oxygen atoms of water. Here O1 is oxygen atom of hydroxyl group (-OH), O2 is the oxygen atom of epoxy group (-O-), O3 is the oxygen atom of the carboxyl group which is bonded to only C atom (-C=O), O4 is the oxygen atom of carboxyl group which is bonded to H and C atom (C-O-H) and OW is the oxygen atom of water. As can be seen from Figure 4-7 the height of the first peak for $g(r)$ between O4-OW pair is highest followed by O1-OW, O3-OW and O2-OW pairs. This indicates strong interaction between carboxyl functional group and water. As discussed in the previous sections the carboxyl functional groups are located on the edges of the GO nanosheets and the hydroxyl and epoxy functional groups are located on the basal plane of the GO nanosheets. So, inside the membrane as the permeating water molecules pass by the edges of the GO nanosheets, some of

the water molecules in the hydration shell move away due to the intense interaction between the carboxyl functional groups (located at the edges of the GO nanosheets) and water. As a consequence, at those positions the number of water molecules in the hydration shell of a permeating water molecule reduces. On the other hand the interaction of hydroxyl and epoxy functional group with water is less as compared to the interaction between carboxyl functional group and water. So, inside the membrane, at the positions near the basal plane of the GO nanosheets (where the hydroxyl and epoxy groups are located) the number of water molecules in the hydration shell of permeating water is more as compared to the positions near the edges of the GO nanosheets (where the carboxyl functional groups are located). However, outside the membrane these numbers are always higher than the numbers inside the membrane.

Figure 4-8 shows the density of water molecules along the permeate direction of the membrane (Z direction). The distribution of water molecules inside the layered GO membrane is different from bulk water distribution. For all the three configurations the density inside the membrane is less than the bulk water density. However for configuration-1 (Figure 4-8a) the density drops to a lower value followed by configuration-2 (Figure 4-8b) and configuration-3 (Figure 4-8c). This is in conjunction with the lower water permeability of configuration-1 and configuration-2 as compared to configuration-3. The fluctuation of density inside the membrane is due to the distribution of oxygen containing functional groups and the movement of the GO nanosheets. The fluctuation is more for configuration-1 followed by configuration-2 and configuration-3.

Figure 4-9 shows the distribution of distance traversed, time taken by the water molecules and their corresponding velocity while permeating through the GO membranes. The average distance traveled by the water molecules through the GO membranes while permeating, for configuration-1 is 526.78 nm, for configuration-2 is 463.27 nm and for configuration-3 is 419.82 nm. The average time taken by the water molecules to permeate through the GO membranes for configuration-1 is 16.47 ns, for configuration-2 is 14.03 ns and for configuration-3 is 12.12 ns. The average velocity of the water molecules while permeating through the layered GO

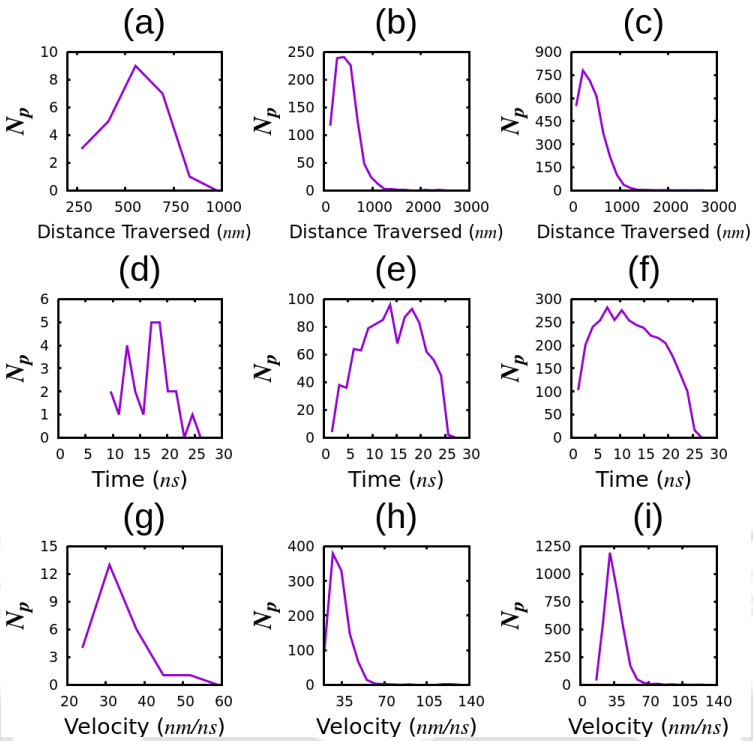

Figure 4-9: Distribution of distance traversed (a) configuration-1 (b) configuration-2 (c) configuration-3, residence time (d) configuration-1 (e) configuration-2 (f) configuration-3 and velocity (g) configuration-1 (h) configuration-2 (i) configuration-3, of the water molecules while permeating through the layered GO membranes.

membranes for configuration-1 is 32.15 nm/ns, for configuration-2 is 33.16 nm/ns and for configuration-3 is 34.76 nm/ns.

4.3.2 Ion Dynamics

In addition to the water permeability we also computed the salt permeability through the layered GO membranes. Density of ions along the Z direction for the 3 membrane configurations are shown in Figure 4-10. For configuration-1 and configuration-2 no salt ion has permeated through the membranes as shown in Figure 4-10a and Figure 4-10b. For configuration-3 (Figure 4-10c) 2 Mg^{2+} ions, 5 Na^{+} ions and 9 Cl^{-} ions are permeated through the membrane from the draw solution to the feed solution and 11 Cl^{-} ions are permeated from the feed solution to the draw solution.

Figure 4-11a, Figure 4-12a and Figure 4-13a respectively depict the trajectory of

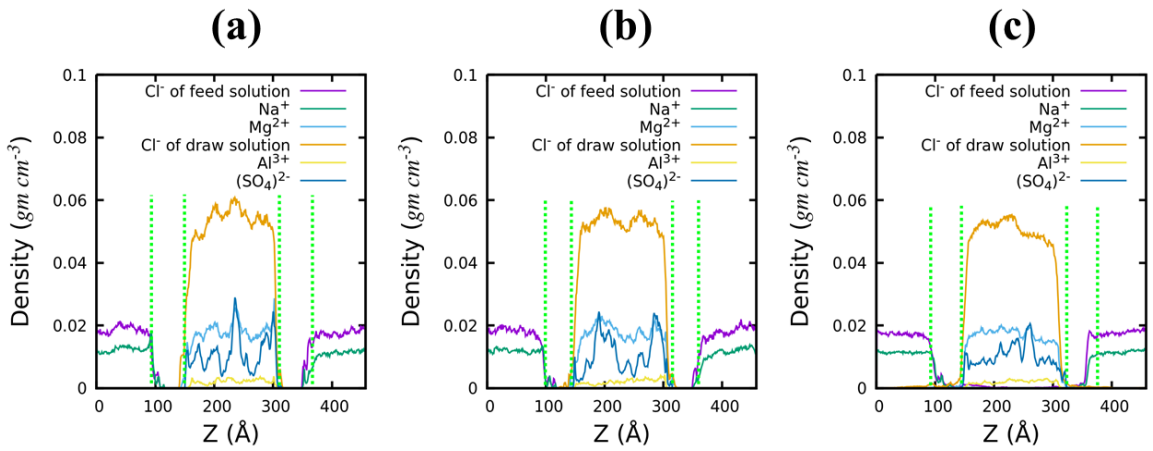

Figure 4-10: Density of ions along the Z direction. (a) configuration-1 (b) configuration-2 (c) configuration-3. The positions of the two membranes are shown by two pair of dotted green lines. Please note that simulation time for configuration-1 and configuration-2 is 25 ns, while it is 64 ns for configuration-3.

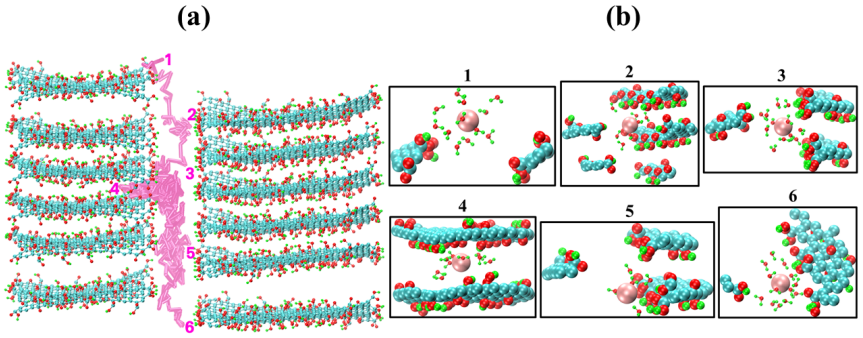

Figure 4-11: (a) Trajectory of Mg^{2+} ion inside the layered GO membrane of configuration-3. (b) Number of water molecules in the hydration shell of Mg^{2+} ion at various locations while permeating through the membrane. Red color is for oxygen atoms, green color is for hydrogen atoms, cyan color is for carbon atoms and mauve color is for Mg^{2+} ion.

the Mg^{2+} ion, Na^{+} ion and Cl^{-} ion inside the layered GO membrane of configuration-3. Along with their trajectory inside the membrane the number of water molecules in their hydration shell is also computed. The radius of the hydration shell of Mg^{2+} ion is 4.25 Å, while for Na^{+} ion and Cl^{-} ion it is 3.15 Å. Figure 4-11b, Figure 4-12b and Figure 4-13b show the number of water molecules in the hydration shell of the Mg^{2+} ion, Na^{+} ion and Cl^{-} ion respectively at various locations while permeating through the layered GO membrane of configuration-3. Water molecules within

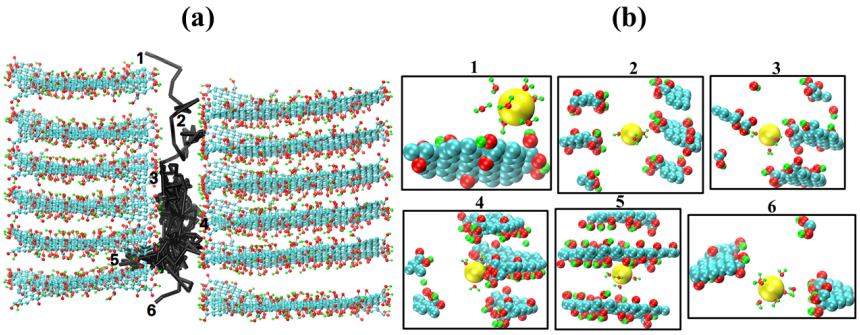

Figure 4-12: (a) Trajectory of Na^+ ion inside the layered GO membrane of configuration-3. (b) Number of water molecules in the hydration shell of Na^+ ion at various locations while permeating through the membrane. Red color is for oxygen atoms, green color is for hydrogen atoms, cyan color is for carbon atoms and yellow color is for Na^+ ion.

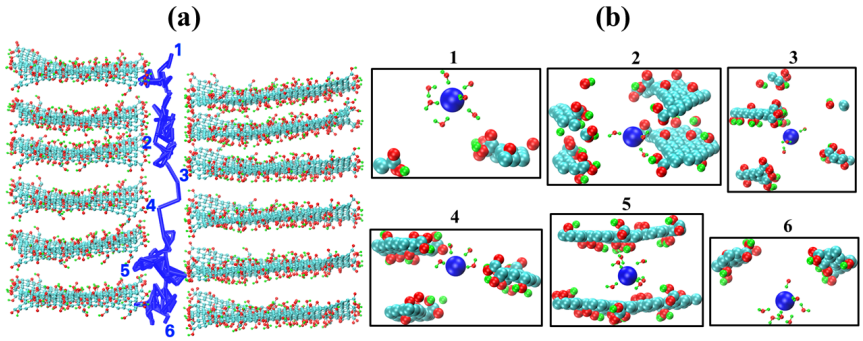

Figure 4-13: (a) Trajectory of Cl^- ion inside the layered GO membrane of configuration-3. (b) Number of water molecules in the hydration shell of Cl^- ion at various locations while permeating through the membrane. Red color is for oxygen atoms, green color is for hydrogen atoms, cyan color is for carbon atoms and blue color is for Cl^- ion.

hydration radius from the center of the permeating ion are shown in ball and stick representations (VMD). Atoms of the GO membrane within 12.0 Å from the center of the permeating ion are shown in VDW representations (VMD). The number of water molecules in the hydration shell of the ions is more outside the membrane (positions 1 and 6 in Figure 4-11, Figure 4-12 and Figure 4-13) as compared to its value inside the membrane (positions 2, 3, 4 and 5 in Figure 4-11, Figure 4-12 and Figure 4-13). However, inside the membrane, at the locations near the edges of the GO nanosheets (positions 2 and 5 in Figure 4-11, positions 2, 3, 4 in Figure 4-12 and Figure 4-13),

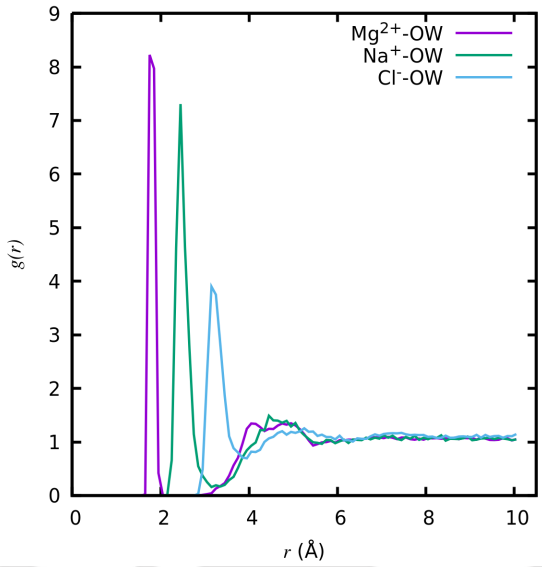

Figure 4-14: Radial distribution function between the ions and oxygen atoms of water inside the layered GO membrane of configuration-3.

the decrease in number of water molecules in the hydration shell of the ions is more prominent as compared to the locations near the basal plane of the GO nanosheets inside the membrane (position 4 in Figure 4-11, position 5 in Figure 4-12 and Figure 4-13). As in the case of water trajectory (Figure 4-4, Figure 4-5 and Figure 4-6) here also the variation of number of water molecules in the hydration shell of ions can be attributed to the interaction between water molecules and the oxygen containing functional groups of the GO nanosheets of the membrane. The carboxyl group has the highest intensity of interaction with the water molecules followed by hydroxyl and epoxy functional group (Figure 4-7). When an ions come closer to the edges of the GO nanosheets during the course of its permeation through the membrane, the carboxyl functional group located at those edges interact strongly with the water molecules in the hydration shell of the ions. As a consequence some water molecules from the hydration shell of the ions shedded away. Similarly, when the permeating ions come closer to the basal plane of the GO nanosheets, the hydroxyl and epoxy functional groups located in the basal plane of the GO nanosheets replaced some of the water molecules in the hydration shell of the ions. But the interaction intensity of hydroxyl and epoxy groups with the water molecules is less as compared to the

interaction intensity between carboxyl functional group and water. As a consequence, the decrease in the number of water molecules in the hydration shell of the ions is more near the edges of the GO nanosheets as compared to the locations near the basal plane of the GO nanosheets.

The functional groups present on the GO nanosheets are negatively charged. When a cation enters inside the layered GO membrane it experiences an attractive interaction from the functional groups. On the other hand when an anion enters inside the layered GO membrane, there is an repulsive interaction between the functional groups and the anion. So the cations are trapped inside the membrane for a longer duration of time as compared to the anions. Higher the magnitude of the charge on the cation, longer it takes to permeate through the membrane. The permeability of the ions through the membrane can also be influenced by its extent of interaction with the water molecules. More intense the interaction of the ion with the water molecules in its hydration shell more difficult for that ion to permeate through the layered GO membrane. Figure 4-14 depicts the radial distribution function between the ions and oxygen atom (OW) of the water molecules. It is evident from Figure 4-14 that the interaction intensity between the ions and the water molecules follows the order $Mg^{2+} > Na^{+} > Cl^{-}$, accordingly the permeation rate of the ions through the layered GO membrane follows the order $Mg^{2+} < Na^{+} < Cl^{-}$.

4.3.3 Membrane Performance

When immersed in polar solvents (e.g. water) swelling of GO membrane is observed due to intercalation of the solvent molecules in the interlayer gallery of the membrane. Several recent studies have addressed this issue encountered by layered GO membrane [23, 31]. Fang *et al.* [31] showed that cations (K^{+}, Na^{+}, Ca^{2+}, Li^{+}, Mg^{2+}) can be effectively used to control the the interlayer spacing (or swelling) of the layered GO membrane. Their study suggested that there is a reduction in the interlayer spacing of the layered GO membrane when immersed in NaCl solution and KCl solution as compared to the interlayer spacing of the layered GO membrane in aqueous solutions. They attributed this reduction in interlayer spacing to the

- Cation-π interactions of the intercalating hydrated cations (K^+ and Na^+) and the aromatic rings of the GO sheets.

- Interaction between the hydrated cations and the oxygen containing functional groups on the GO sheets.

However, they also reported that intercalation of the cations like Ca^{2+}, Li^+ and Mg^{2+} results in increase in interlayer spacing of the layered GO membrane.

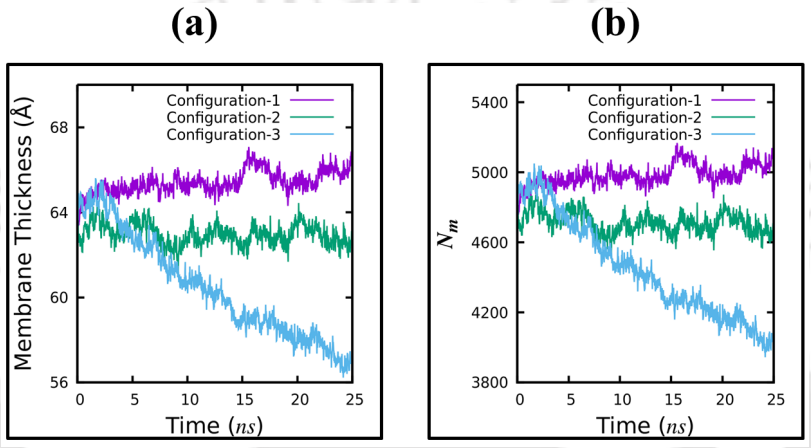

Figure 4-15: (a) Thickness of the layered GO membrane and (b) Number of water molecules ($\boldsymbol{N_m}$) inside the layered GO membrane during the course of simulation.

In the present study, we computed the variation of thickness of the layered GO membrane during the course of the simulation for each of the three membrane configurations as shown in Figure 4-15a. We also computed the corresponding number of water molecules ($\boldsymbol{N_m}$) inside the layered GO membrane as shown in Figure 4-15b. For configuration-1, 363 water molecules are accumulated inside the layered GO membrane (Figure 4-15b) during the course of the simulation and consequently the thickness of the membrane increases by 3.22 Å (Figure 4-15a). So, on an average the interlayer spacing increases by 0.644 Å for configuration-1 in the timescale of the present simulation study. On the contrary, for configuration-2 and configuration-3 there is a decrease in membrane thickness as well as reduction in the number of water molecules inside the layered GO membrane (Figure 4-15a and b). For configuration-2 the membrane thickness is reduced by 0.79 Å and 117 water molecules are squeezed

out from the layered GO membrane. So, on an average the interlayer spacing is reduced by 0.158 Å for configuration-2. Similarly, the thickness of the layered GO membrane for configuration-3 decreases by 7.0 Å and 823 water molecules are squeezed out from the membrane. So, for configuration-3, the average value of decrease in interlayer spacing is 1.4 Å.

This opposite nature of swelling behavior of the configuration-1 with configuration-2 and configuration-3 can be attributed to the intercalation of Na^+ ions with reference to the work of Fang *et al.* [31]. As mentioned earlier their experimental investigations suggested the reduction of interlayer spacing with the intercalation of Na^+ ions in the interlayer gallery of layered GO membrane.

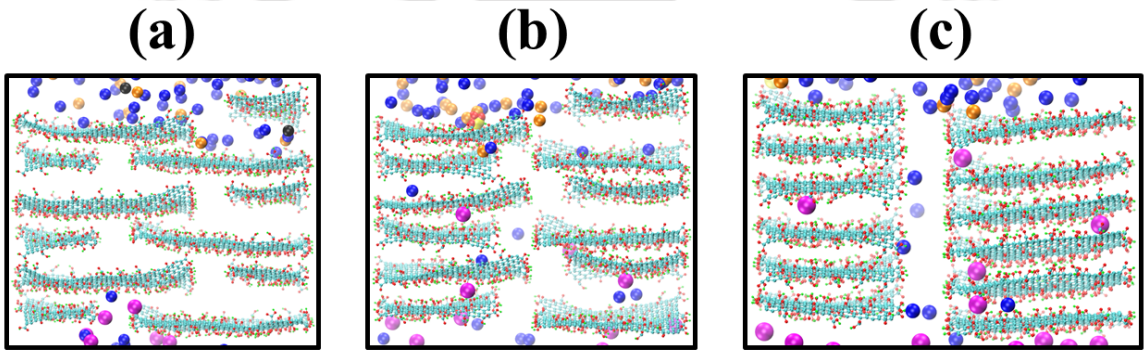

Figure 4-16: Intercalation of ions inside layered GO membrane (a) configuration-1 (b) configuration-2 (c) configuration-3. The green color is for hydrogen atoms, the red color is for oxygen atoms, the cyan color is for carbon atoms, the blue color is for Cl^- ions, the magenta color is for Na^+ ions, the orange color is for Mg^{2+} ions, the black color is for Al^{3+} ions, the yellow color is for sulfur atoms.

As can be seen from Figure 4-16a, no ions were intercalated inside the interlayer gallery for configuration-1 except for few (no Na^+ ions) at the top right corner. For configuration-2 (Figure 4-16b) some ions (Na^+, Cl^+ and Mg^{2+}) were intercalated inside the membrane, majority of which are Cl^- ions. Although Mg^{2+} ions contribute to the swelling of GO membrane the intercalated Na^+ ions counteracts the same, resulting in decrease in interlayer spacing for the layered GO membrane of configuration-2. However, it is important to note that, although ions are intercalating inside the layered GO membrane of configuration-2, no ion has permeated through it in the timescale

of the present simulation study. For configuration-3 also, ions are intercalating inside the layered GO membrane, majority of which are Na^+ ions (Figure 4-16c). Due to these considerable number of intercalating Na^+ ions, there is an effective decrease in the interlayer spacing which is more as compared to configuration-2. This reduction in interlayer spacing for configuration-2 and configuration-3 are in accordance with the experimental observations of Fang *et al.* [31].

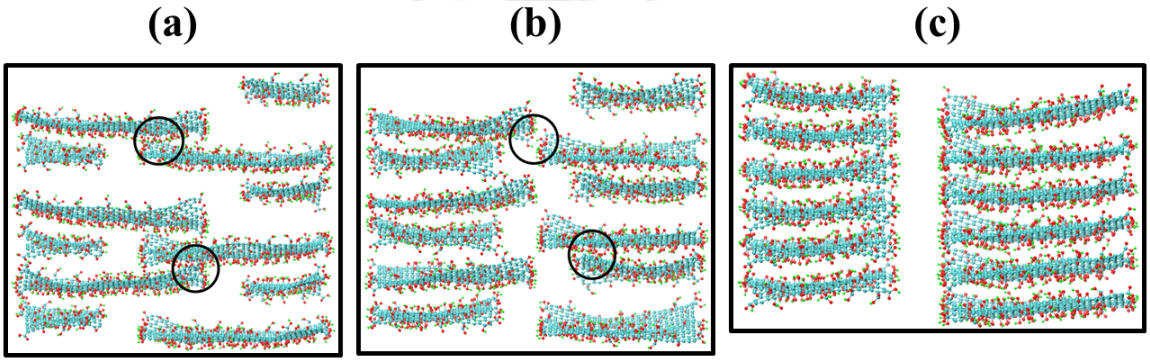

Figure 4-17: Internal structure of the membranes during simulations. The blockage of the water and salt passages are shown in black circles. (a) configuration-1 (b) configuration-2 (c) configuration-3. Red color is for oxygen atoms, green color is for hydrogen atoms and cyan color is for carbon atoms.

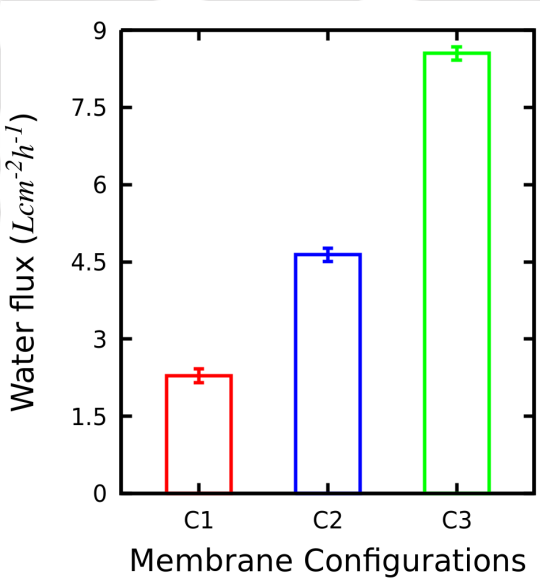

Figure 4-18: Water permeability of the three layered GO membrane configurations.

In the temporal evolution of number of water molecules in the draw solution box (Figure 4-3) there are some fluctuations. These fluctuations could be due to the random thermal motions of the molecules in the system and the movements of the GO nanosheets (along the Z coordinate) of the layered GO membranes, since they are constrained only in the XY plane during the simulations. Due to the movement of the GO nanosheets of the layered GO membranes, at some points during permeation, the pathways for the water molecules (and ions) get blocked for configuration-1 (Figure 4-17a) and configuration-2 (Figure 4-17b). However, this blockage of the permeate pathways is not observed for configuration-3 (Figure 4-17c). This blockage of water (and ions) pathways could also be one of the reason of less water (and ions) permeability of configuration-1 and configuration-2 as compared to configuration-3. For configuration-3, $\mathbf{W}= 0$ i.e. the water pathways for this configuration is straight. So for this configuration the water (and ions) permeation is least affected by the movements of the GO nanosheet of the layered GO membrane. On the other hand for configuration-1 and configuration-2 the water (and ions) pathways are "zig-zag" as for these configurations $\mathbf{W}\neq 0$. So for these two configurations the movement of the GO nanosheets severely affects the water (and ions) permeability through the membranes.

The currently available FO membranes have water flux less than 60.0 $Lm^{-2}h^{-1}$ [117]. Recently, on a lab scale a FO membrane with water flux 93.6 $Lm^{-2}h^{-1}$ is also been reported [121]. Liu *et al.* [289] performed MD simulation on FO process with single layer strained C_2N membrane which showed a water flux as high as 14.36 $Lcm^{-2}h^{-1}$ at a temperature of 338 K. Similarly MD simulations of Gai *et al.* [10] showed a water flux of 28.1 $Lcm^{-2}h^{-1}$ through porous graphene membrane in FO process and this value is 1.8×10^4 times higher than a typical cellulose triacetate membrane. However, in both these [10, 289] cases, a single porous nanosheet is considered as a membrane and Gai *et al.* [10] considered fresh water as the feed solution. In the present study the layered GO membrane of configuration-1 showed a water flux of 2.28 $Lcm^{-2}h^{-1}$, configuration-2 showed a water flux of 4.63 $Lcm^{-2}h^{-1}$ and the water flux for configuration-3 is found to be 8.55 $Lcm^{-2}h^{-1}$ as shown in

Figure 4-18.

On the other hand, the layered GO membranes with configuration-1 and configuration-2 shows 100 % salt rejection as no salt ion was permeating through the GO membranes for these two configurations, at least in the range of time scales of the present simulation. Configuration-3 showed a salt rejection of 96.29 % which is close to the value reported in the existing literature [283]. With this reasonable value of salt rejection and water flux the layered GO membranes may turn out to be a nice potential candidate for FO applications for sea water desalination. On the other hand the inherent hydrophilic nature of the GO nanosheet gives an extra edge to the layered GO membrane over the existing FO membranes which are very much prone to membrane fouling mainly due to their hydrophobic nature. Again, one can judiciously select the lateral dimensions of the GO nanosheets (or vary the pore offset distance **W**) of the layered GO membranes to get the desired water permeability and salt rejection according to specific applications.

4.4 Conclusions

The performance of GO in FO process is evaluated using 3 different layered GO membrane configurations via non-equilibrium MD simulations. These membrane configurations differ in their pore offset distance **W**. With the increase in **W**, the water permeability of the layered GO membrane decreases. Increase in **W** also leads to the blockage of the pathways of the permeate through the layered GO membrane due to the movement of the GO nanosheets. This severely affects the performance of the layered GO membrane during the FO process. However, it is necessary to know that the maximum simulation time for this present work is 64 ns (for configuration-3) and the sizes of the individual GO nanosheets that were used to construct the layered GO membrane are 20.0×49.0 Å^2, 30.0×49.0 Å^2, 40.0×49.0 Å^2 and 50.0×49.0 Å^2. Hence, it could be an interesting future problem to understand the existence and effect of these blockage with higher GO nanosheet dimension and higher simulation time .

The water and ion dynamics inside the GO membrane is affected by the presence of the oxygen containing functional groups on the GO nanosheets. Near the edges of the GO nanosheets inside the layered GO membrane, the number of water molecules in the hydration shell of the permeating waters and ions reduces as compared to its value near the basal plane of the GO nanosheets. This is because of the strong interaction between the water molecules and carboxylic functional groups located at the edges of the GO nanosheets. The permeability of ions through the layered GO membrane follows the order $Mg^{2+} < Na^{+} < Cl^{-}$. The ion permeability through the layered GO membrane is dependent on the type and magnitude of charge the ion possesses and also on the interaction strength between ion and water. Ion permeability also dependent on the geometric parameter **W**, as configuration-1 and configuration-2 show 100 % salt rejection and configuration-3 shows a salt rejection of 96.29 %. Increase in **W** also reduces the velocity of the permeating water molecules through the membrane and increases their permeation time.

Although performance of GO as a membrane in RO process has been tested rigorously using both experimental and theoretical tools, its application in FO has not received much attention. The present study employed large scale MD simulations to reveal interesting insights in the process of using GO as a FO membrane material. To make FO process economical, in addition to the membrane performance, facile regeneration of draw solute is essential. Hence in the future one can test GO membrane with various draw solutions and its anti-fouling nature against the difficult feed environments.

भारतीय प्रौद्योगिकी संस्थान गुवाहाटी
Indian Institute of Technology Guwahati

Chapter 5

Dehydration of Acetic Acid using Layered Graphene Oxide (GO) Membrane through Forward Osmosis (FO) Process: A Molecular Dynamics Study[2]

5.1 Introduction

Acetic acid is one of the major organic chemicals that has been extensively used in various chemical and food industries. It is being used in the production of vinyl acetate, acetic anhydride, terephthalic acid, vitamins and isophthalic acid. Also it is formed as an intermediate in the production of aspirin and in esterification of alcohols [290, 291].

On the other hand in the manufacturing process of acetic acid, often an aqueous intermediate is formed which needs to be dehydrated in order to get pure acetic acid

[2]A. Gogoi, K. A. Reddy, S. Senthilmurugan and P. Mondal. Dehydration of acetic acid using layered graphene oxide (GO) membrane through forward osmosis (FO) process: a molecular dynamics study. *Mol. Simul.*, 46(18):1500-1508, 2020.

[292]. Acetic acid is also a major component in industrial waste of many industrial activities e.g. manufacture of aspirin, camphor, cellulose acetate and explosives. Acetic acid contained (typically 0.1 to 5% by weight) in these waste stream can be extracted and reused which in turn can significantly improve the industrial productivity.

However the applicability of standalone GO membrane for acetic acid dehydration using FO process has not been reported yet. In the present study we have investigated the potential applicability of layered GO membranes for the dehydration of acetic acid with FO process. We consider layered GO membranes with different pore offsets (**W**) and interlayer distances (**H**) to get an insight into the effect of microstructure of the layered GO membrane on its separation performance. Membrane performance has been characterized based on the corresponding water permeance, salt rejection and acetic acid rejection.

5.2 Methodology

The three major components of a FO system are feed solution, a semipermeable membrane and draw solution. The feed and the draw solutions are separated by the semipermeable membrane. The osmotic pressure of the draw solution is higher than the feed solution. Due to this difference in osmotic pressure water molecules from the feed solution permeate through the membrane towards the draw solution. In general a good quality FO membrane allows maximum water flux with minimum reverse solute flux. The quality of a membrane also depends on its resistance against fouling and its adaptability to difficult feed and draw solution environment.

In the present study layered GO membrane is considered as the FO membrane. To construct the GO surface, first a graphene sheet is constructed using "Nanotube Builder" package of VMD [293]. After the construction of the graphene sheet, the oxygen containing functional groups (epoxy, hydroxyl and carboxylic) are added to the graphene sheet using Avogadro [294] to construct the GO surface. The oxygen containing functional groups are added according to the chemical composition $C_{10}O_1(OH)_1(COOH)_{0.5}$ [5, 46]. The epoxy and hydroxyl groups are randomly grafted

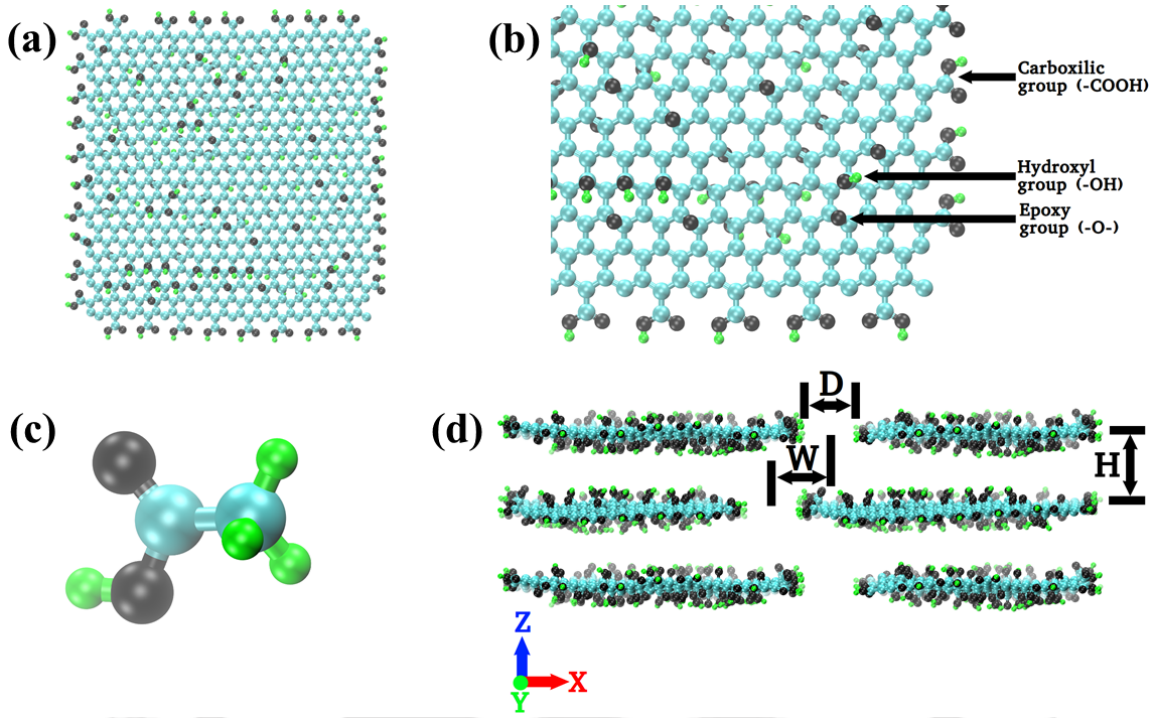

Figure 5-1: (a) A GO nanosheet. (b) The distribution of functional groups on GO nanosheet. (c) Structure of an acetic acid molecule. (d) Layered GO membrane with **D**=7 Å, **W**=8 Å and **H**= 10 Å. The green color is for hydrogen atoms, the black color is for oxygen atoms and the cyan color is for carbon atoms.

Table 5.1: Values of geometric parameters of layered GO membranes and corresponding membrane abbreviations

Geometric Parameters			Membrane abbreviations
D (Å)	**W (Å)**	**H (Å)**	
7.0	0.0	10.0	D7-W0-H10
7.0	8.0	10.0	D7-W8-H10
7.0	16.0	10.0	D7-W16-H10
7.0	24.0	10.0	D7-W24-H10
7.0	0.0	8.0	D7-W0-H8
7.0	0.0	12.0	D7-W0-H12
7.0	0.0	14.0	D7-W0-H14
7.0	0.0	18.0	D7-W0-H18

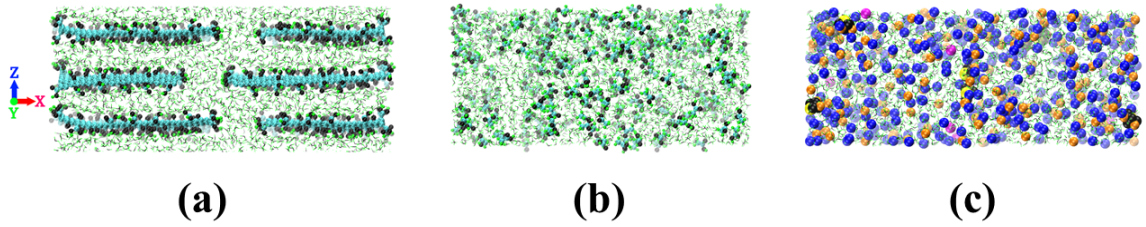

Figure 5-2: (a) Hydrated layered GO membrane. (b) Aqueous acetic acid solution (feed solution). (c) Draw solution. The green color is for hydrogen atoms, the black color is for oxygen atoms, the cyan color is for carbon atoms, the blue color is for Cl^- ions, the orange color is for Mg^{2+} ions, the magenta color is for Al^{3+} ions, the yellow color is for sulfur atoms.

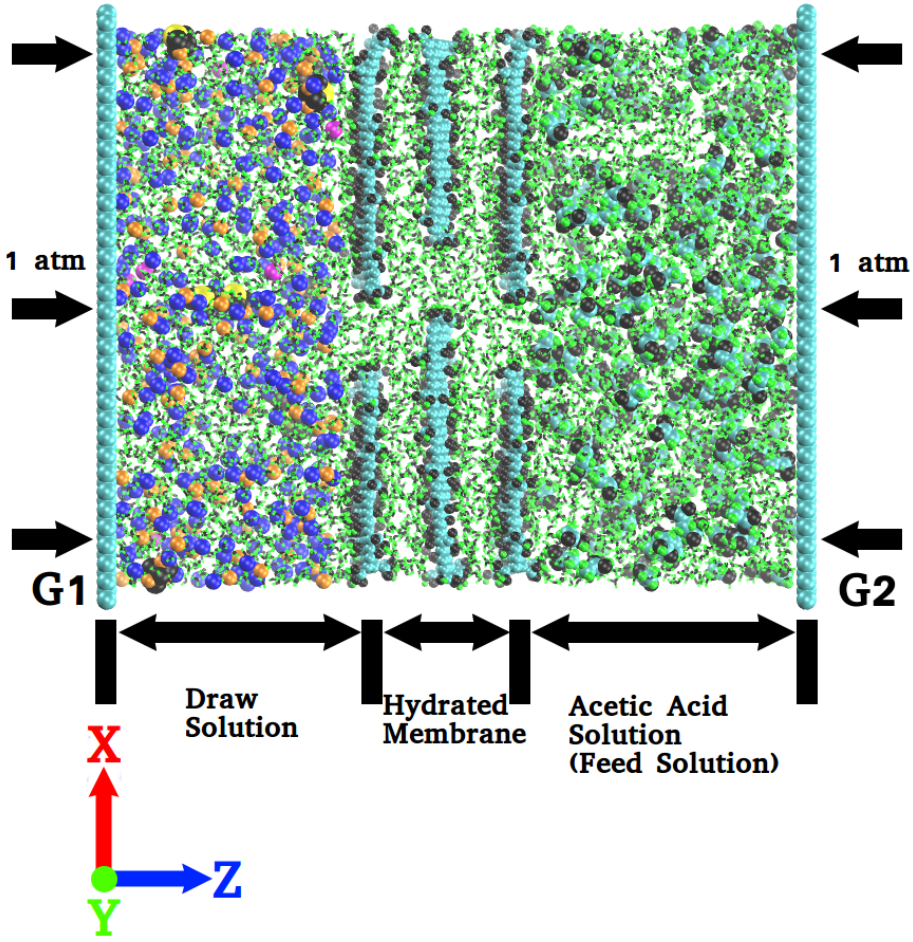

Figure 5-3: Simulation setup. The green color is for hydrogen atoms, the black color is for oxygen atoms, the cyan color is for carbon atoms, the blue color is for Cl^- ions, the orange color is for Mg^{2+} ions, the magenta color is for Al^{3+} ions, the yellow color is for sulfur atoms.

to the carbon atoms on the basal plane of the graphene surface [5, 46]. Carboxylic functional groups are attached randomly to the carbon atoms at the edge of the graphene sheet [5, 46]. After addition of the functional groups on the graphene surface, energy minimization of the GO surface is performed in Avogadro [294]. During energy minimization the functional groups as well as the carbon atoms of the graphene sheet change/adjust their co-ordinates according to minimum potential energy. The atom types on the GO nanosheets and their partial charges are reported in the supporting information (Fig. S1 and Table 1). The structure of the GO nanosheet is shown in Fig. 5-1a and 5-1b. Using these GO nanosheets as the constructing units, different layered GO membrane configurations were constructed. Fig. 5-1d shows a layered GO membrane where the geometric parameters **D**, **W** and **H** are termed as pore width, pore offset distance and interlayer distance respectively.

In graphite, the interlayer distance between the successive graphene sheets is around 3.4 Å [295]. In GO membranes the interlayer distance between the GO nanosheets is greater than this because of the presence of the oxygen containing functional groups [17]. In dry conditions this interlayer distance is 7-9 Å. As the humidity increases the water molecules diffuse into the interlayer space of the GO nanosheets of the layered GO membrane and accordingly the interlayer spacing increases. When the layered GO membrane is immersed in water and completely wetted, this interlayer spacing can increase up to 12-13 Å [18, 19]. In some articles [13, 100] the interlayer spacing between the GO nano-sheets of hydrated GO membrane is reported as 9-10 Å. Based on these informations, the values of the geometric parameters of the layered GO membranes used in the present study and the corresponding abbreviations for the membranes are tabulated in Table 5.1. From an experimental point of view layered GO membrane with large value of pore offset distance (**W**) resembles to membrane composed of GO nanosheets of large lateral dimensions and membrane with smaller value of **W** resembles GO membrane composed of nanosheets of smaller lateral dimensions [35, 102, 296].

After the construction of the membrane, it is hydrated in a water box of size $77 \times 49 \times 32$ Å^3 (Fig. 5-2a). The water molecules within 2 Å of the GO nanosheets

are removed after which the number of water molecules in the hydrated box are 1900. Since the primary objective of this study is to dehydrate acetic acid through FO process we consider a 20 *wt.*% aqueous solution of acetic acid as the feed solution. This acetic acid solution contains 3000 water molecules and 225 acetic acid molecules (Fig. 5-2b). A solution of 3 *M* $MgCl_2$ and 0.05 *M* $Al_2(SO_4)_3$ is considered as the draw solution [283, 297]. It contains 3000 water molecules, 178 Mg^{2+} ions, 356 Cl^- ions, 6 Al^{3+} ions and 9 $(SO_4)^{2-}$ ions (Fig. 5-2c). The simulation system is then constructed by placing the hydrated membrane between the feed and draw solution as shown in Fig. 5-3. A single layer of graphene sheet is placed at the edges of feed and draw solution which acts as piston during the course of the simulation. The graphene sheet at the bottom of the draw solution box is labeled as **G1** and the graphene sheet at the top of the feed solution box is labelled as **G2**. Atmospheric pressure is applied to both the graphene pistons in opposite directions (along *Z* axis) as shown in Fig. 5-3. This kind of atomistic simulation strategy previously been tested for various FO and RO applications [9, 298, 299, 300, 301, 302, 303, 304]. The positions of these pistons and the pressure fluctuations in the system during the course of the simulation are reported in the supporting information (Fig. S4 and S5). As the osmotic pressure of the draw solution is higher than the feed solution, the water molecules from the feed solution permeate through the layered GO membrane towards the draw solution. As mentioned earlier, the feed solution considered in this present study is a 20 wt.% aqueous acetic acid solution. So, as the water molecules from the feed solution permeating through the membrane towards the draw solution, the number of water molecules in the feed solution gradually decreases. Consequently, the aqueous acetic solution gets dehydrated. After the construction of the simulation systems, non-equilibrium molecular dynamics (MD) simulations are carried out using NAMD 2.11 [285]. All the atomic interactions are computed using OPLS-AA force field [45]. The water molecules are modeled using SPC water model [286] and the bond lengths of the water molecules are constrained using SETTLE algorithm [287]. The van der Waals interactions are computed using Lennard-Jones potential with a cut-off distance of 12.0 Å. Particle mesh Ewald (PME) method is used for the

computation of long range electrostatic interactions [288]. The validation of the force field parameters used in this present study is reported in the supporting information (Fig. S2 and S3).

Before the MD simulation, energy minimization was carried out. Then the system was equilibrated for 1 ns at a constant pressure of 1.0 atm and at a temperature of 300 K. Pressure was kept constant using modified Nosé-Hoover method in which Langevin dynamics were used to control fluctuations in the barostat. The barostat oscillation time and damping factors both were set to 0.3 ps. Temperature was controlled by Langevin dynamics with a damping factor of 5 ps^{-1}. Then, the production runs were performed for 15 ns at a constant temperature of 300 K. Periodic boundary conditions were applied along all the directions. An empty space of 50 Å in length is applied along the Z dimension, both at the top and bottom of the simulation system. During the simulations, the corner carbon atoms of the GO nanosheets were fixed to their initial positions [305, 306] to maintain the layered structure of the GO membrane. For each of the simulation systems 3 independent simulations are performed with different initial configurations (or initial arrangements of atoms) and the results are averaged over these independent simulations.

5.3 Results and Discussion

From the non-equilibrium MD simulations, first we computed the water permeance through the layered GO membranes with different pore offset distances (**W**). The water permeance through the membranes is calculated based on the net increase in the number of water molecules in the draw solution (or net water molecules permeated to the draw solution) during the course of the simulation. As can be seen from Figure 5-4 the water permeance through layered GO membranes decreases with the increase in **W**. This signifies that, layered GO membranes composed of GO nanosheets of larger lateral dimensions have lower water permeance as compared to GO membranes composed of GO nanosheets of smaller lateral dimensions.

Figure 5-5a and 5-5b show the distribution of acetic acid density in the simulation

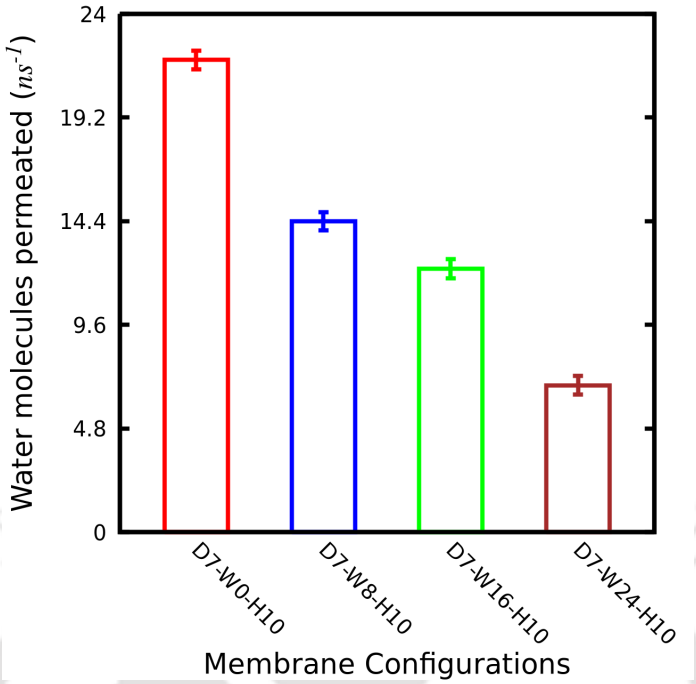

Figure 5-4: Variation of water permeance through layered GO membranes with different values of **W**.

system for D7-W0-H10 and D7-W24-H10 membrane systems respectively. The majority of the acetic acid molecules lie in the feed solution side. However, the density of acetic acid in the feed solution is more for the system with D7-W0-H10 membrane configuration as compared to the system with D7-W24-H10 membrane configuration. This elucidates the higher effectiveness of D7-W0-H10 membrane system in concentrating the acetic acid feed solution as compared to D7-W24-H10 membrane system. The density distributions of water in the simulation system are shown in Figure 5-5c and 5-5d for D7-W0-H10 and D7-W24-H10 membrane systems respectively. For the D7-W0-H10 membrane system, two distinct layers of water can be observed inside the interlayer gallery. This resembles to the ordered structure of water molecules inside the interlayer spacing of GO membranes [281]. However, at a higher value of **W**, the ordered structure of water inside the interlayer gallery of layered GO membrane reduces as can be seen from Figure 5-5d.

The distribution of density of various components of the simulation system along the permeating direction (Z direction in the present study) are shown in Figure 5-

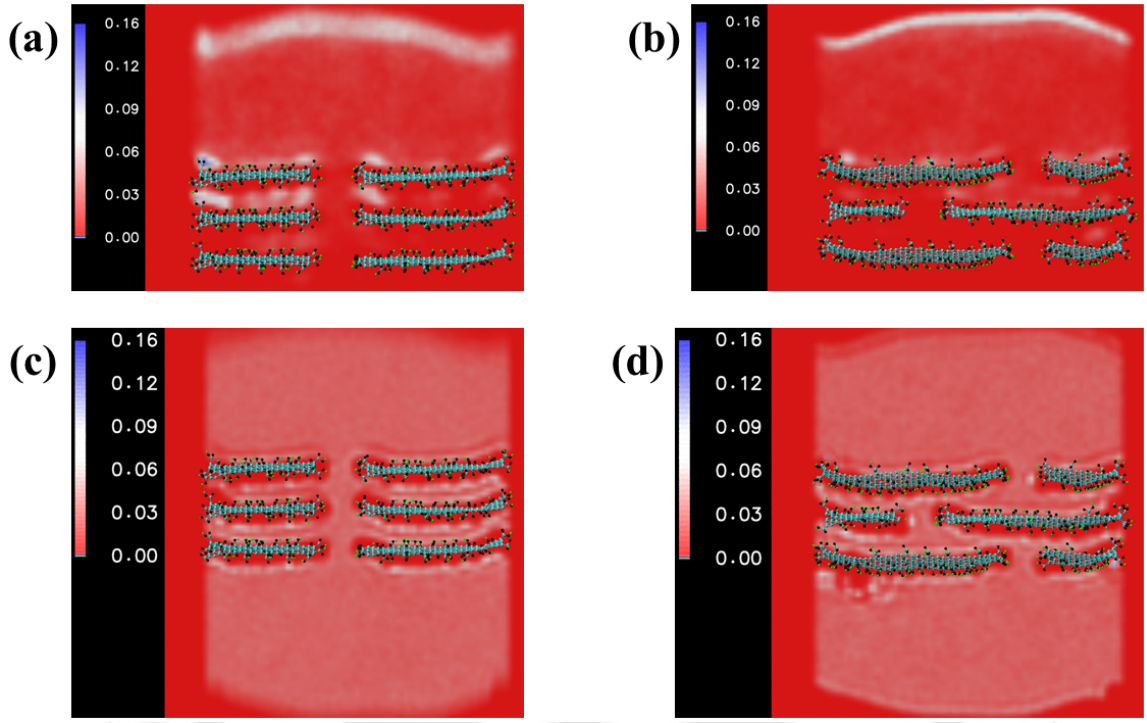

Figure 5-5: Distribution of acetic acid density for (a) D7-W0-H10 membrane system and (b) D7-W24-H10 membrane system. Distribution of water density for (c) D7-W0-H10 membrane system and (d) D7-W24-H10 membrane system. In the membrane, the green color is for hydrogen atoms, the black color is for oxygen atoms and the cyan color is for carbon atoms. The scale bar is in the unit of $atoms\times$ Å^{-3}.

Table 5.2: Diffusion coefficient of water molecules inside the layered GO membranes for different value of **H**.

Membrane abbreviations	Water diffusion coefficient $(cm^2 sec^{-1})$ $\times 10^{-5}$
D7-W0-H8	1.28
D7-W0-H10	1.58
D7-W0-H12	1.74
D7-W0-H14	1.90
D7-W0-H18	2.20

6. The membrane boundaries are shown by a pair of dotted green lines. Inside the membrane, the density distribution of water is "oscillating" in nature. The "valley" of this oscillation refers to the positions of the GO nanosheets of the layered GO

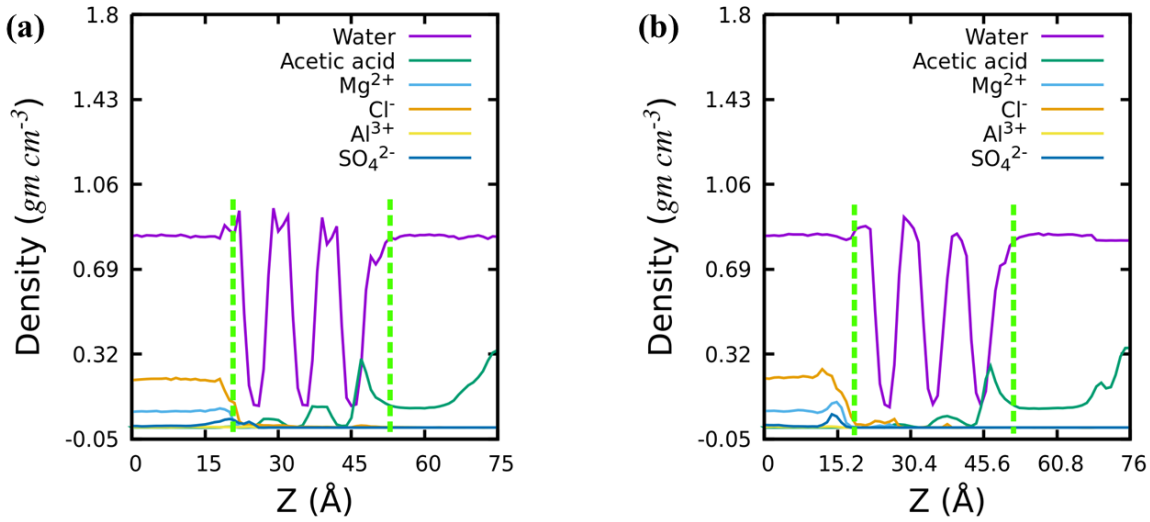

Figure 5-6: Distribution of number density of various components in the simulation system along the permeate direction (Z direction) (a) D7-W0-H10 and (b) D7-W24-H10. The entry and exit points of the membrane are shown with a pair of dotted green line.

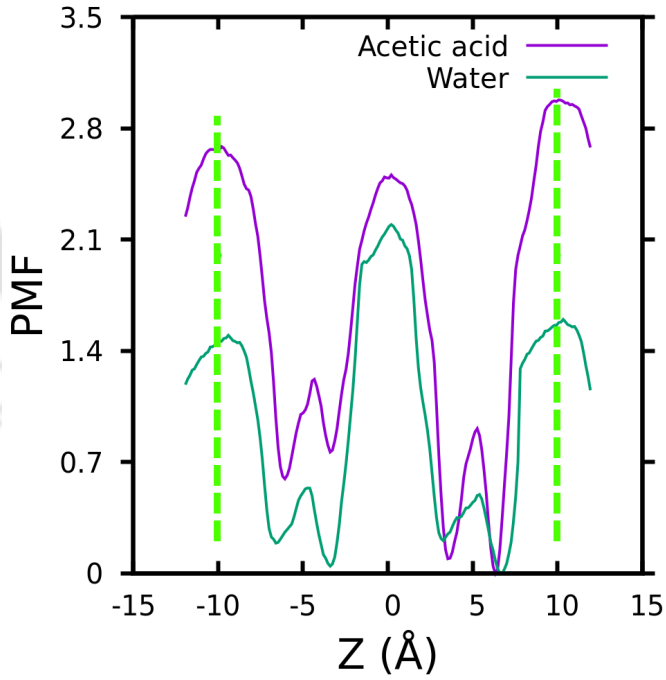

Figure 5-7: Potential of mean force along the permeating direction of layered GO membrane. The entry and exit points of the membrane in terms of reaction coordinate are shown with a pair of dotted green line.

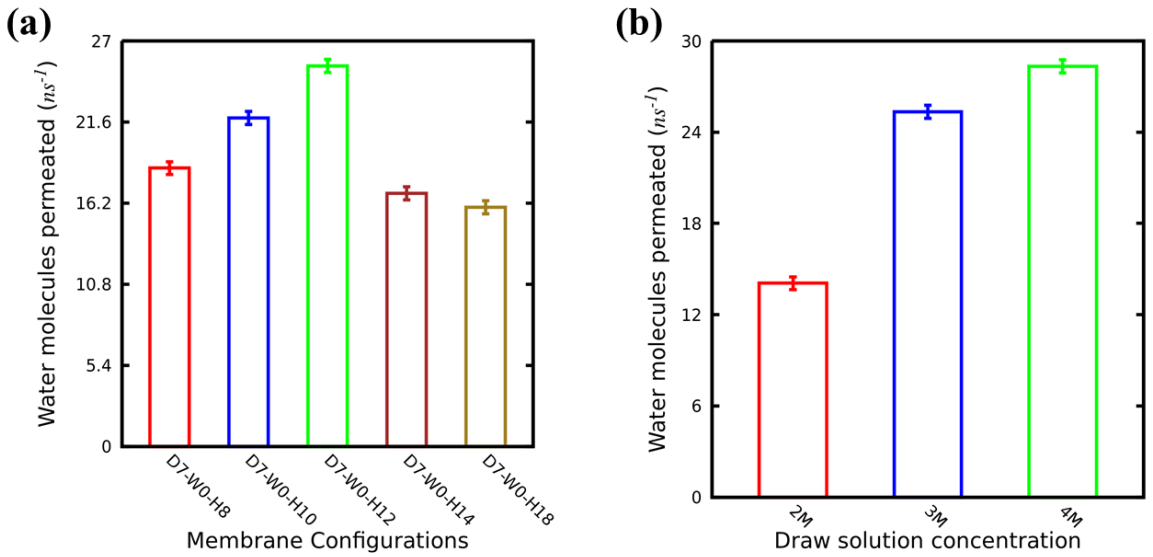

Figure 5-8: (a) Variation of water permeance through layered GO membranes with different values of **H**. (b) Variation of water permeance through layered GO membranes with different values of draw solution concentration (**C**).

membrane. In the "hill" of this distribution, two distinct peaks can be observed for the D7-W0-H10 membrane system (Figure 5-6a). These peaks resemble to the "two layer" structure of water inside the interlayer gallery of the layered GO membrane for D7-W0-H10 membrane system. However, these peaks are not observed for the D7-W24-H10 membrane system (Figure 5-6b) due to the lack of well ordered structure of water inside the interlayer gallery. This difference in water structure may also play an important role in determining the water permeance through the layered GO membranes [9]. The peaks of the acetic acid density distribution inside the layered GO membrane corresponds to the adsorption of the acetic acid molecules on the GO nanosheets of the layered GO membrane. The second and third peaks of the acetic acid density distribution inside the layered GO membrane for D7-W24-H10 membrane system is smaller as compared to D7-W0-H10 membrane system. This signifies the lower permeation of acetic acid from the feed solution to the membrane interior for D7-W24-H10 membrane system as compared to D7-W0-H10 membrane system which is also observed in Figure 5-5a and 5-5b.

To get an insight into the ease of permeation of acetic acid and water through

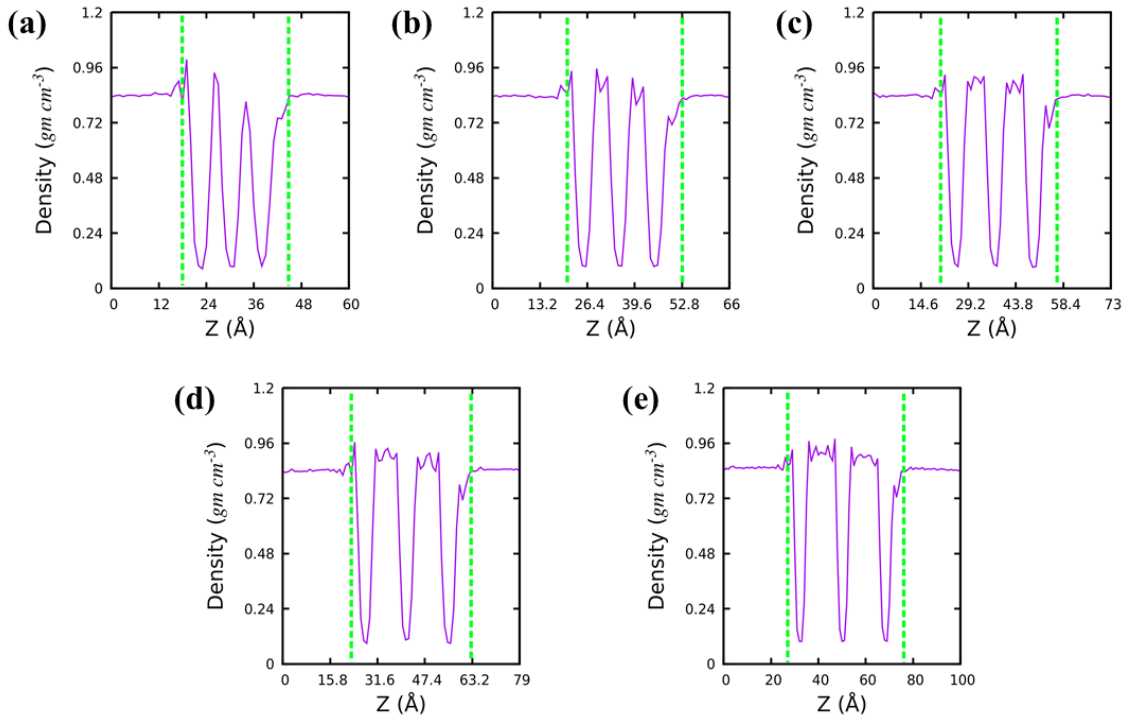

Figure 5-9: Distribution of number density of water molecules along the permeating direction (Z direction) for the membrane configuration (a) D7-W0-H8, (b) D7-W0-H10, (c) D7-W0-H12, (d) D7-W0-H14 and (e) D7-W0-H18. The boundaries of the layered GO membrane are shown with a pair of dotted green lines.

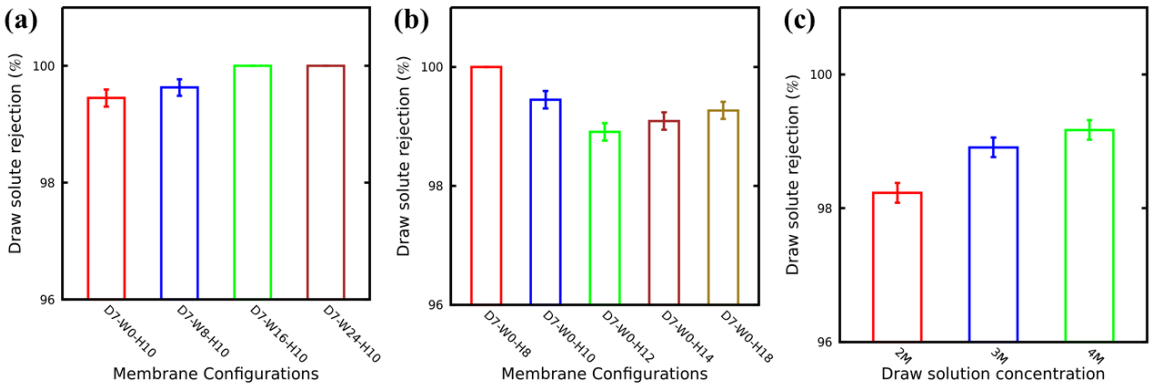

Figure 5-10: Draw solute rejection by layered GO membranes with (a) different **W** (b) different **H** (c) different **C**.

layered GO membranes, potential of mean force (PMF) calculations are performed using umbrella sampling method [307] with replica exchange molecular dynamics

(REMD-US). The relative Z distance between permeating species (water or acetic acid in this case) and the membrane center, along the membrane axis is considered as the reaction coordinate with a width of 1 Å between consecutive umbrella windows. The PMF is generated by analyzing the data via weighted histogram analysis method [308]. Figure 5-7 shows the PMF plots for water and acetic acid molecules through D7-W8-H10 membrane system. As can be seen from Figure 5-7, acetic acid molecules encounter higher barrier to permeate through the membrane as compared to water molecules.

We have also investigated the performance of the layered GO membranes with different values of interlayer distances (**H**). For this, 5 different membrane configurations are considered which are abbreviated as D7-W0-H8, D7-W0-H10, D7-W0-H12, D7-W0-H14 and D7-W0-H18 with the interlayer distances of 8 Å, 10 Å, 12 Å, 14 Å and 18 Å respectively. The corresponding geometric parameters of these five membrane configurations are tabulated in Table 5.1. Figure 5-8a shows the effect of **H** on the water permeance through layered GO membranes. As **H** increases from 8.0 Å to 12.0 Å the water permeance through layered GO membrane increases. But, with further increase in **H**, the water permeance through the membrane decreases. Here, two factors may play an important role in determining the water permeation through the membranes. First one is the distance the water molecules have to traverse to permeate through the membrane which can be termed as "permeation distance". With the increase in permeation distance the water permeance of the membranes decreases. The second one is the diffusivity of water molecules inside the layered GO membranes, the increment in which leads to corresponding increase in water permeance through the membranes. With the increase in **H**, the permeation distance through the layered GO membrane increases. So, with the increase in **H**, the water molecules have to traverse more distance to permeate through the membrane. On the other hand the diffusivity of the water molecules inside the membrane increases with the increase in **H**, as tabulated in Table 5.2. However, the diffusion coefficient of water inside the layered GO membranes is less than its bulk value which is 3.85×10^{-5} $cm^2 sec^{-1}$ [309]. As shown in Figure 5-8a, as **H** increases from 8.0 Å to 12.0 Å, the

water permeance through the layered GO membrane increases. Here the increase in diffusivity of the water molecules inside the layered GO membrane dominates over the the effect of corresponding increase in the permeation distance, resulting in higher water permeance. However with further increase in **H** from 12.0 Å to 18.0 Å there is a gradual decrement in the water permeance (Figure 5-8a). This may be attributed to the increase in permeation distance which suppresses the corresponding effect of increase in diffusivity of the water molecules inside the layered GO membranes.

The structure of water molecules inside the layered GO membrane also plays an important role in determining the water permeance through the membrane as reported in Figure 5-9. The changes in water structure inside the layered GO membrane with the variation in **H** can be observed with the density profile of water along the permeating direction (Z direction) as shown in Figure 5-9. As mentioned earlier (Figure 5-6), the density profile of water inside the layered GO membrane is oscillating in nature. In the "hill" of this oscillation for D7-W0-H10 configuration (Figure 5-9b) two distinct peaks can be observed which resembles to the "two water layers" structure inside the interlayer gallery. For D7-W0-H8 configuration (Figure 5-9a) only a single peak is observed in the "hill" of the density distribution, indicating monolayer structure of water inside the interlayer gallery. Proceeding on the same note, for D7-W0-H12 configuration (Figure 5-9c) three distinct water layers are observed inside the interlayer gallery. However with the further increase in **H** to 14.0 Å and 18.0 Å (Figure 5-9d and 5-9e) these peaks in the "hill" of the water density profile become less steeper and less distinct. This implies the gradual disruption of ordered structure of water inside the interlayer gallery of the layered GO membranes as **H** increases beyond 12.0 Å.

We have also investigated the performance of layered GO membranes with different draw solution concentrations (**C**). For this, three different values of **C** (2.0 M, 3.0 M and 4.0 M) are considered. With these different draw solution concentrations, FO simulations are performed with the D7-W0-H12 membrane configuration with the same feed solution (acetic acid) concentration. With the increase in draw solution concentration the water permeation increases as can be seen from Figure 5-8b. With

the increase in **C**, the osmotic pressure of the draw solution increases which in turn increases the water permeance through the membranes.

Apart from water permeation, the ability of the membrane to reject the draw solute also affect the quality of the acetic acid solution which is being concentrated through FO process. In general to get a better product in the dehydration of acetic acid through FO process, the membrane should have a high water permeance and high draw solute rejection ability. The draw solute rejection of the layered GO membranes in different scenarios are depicted in Figure 5-10. As can be seen from Figure 5-10a, with the increase in **W**, the draw solute rejection of the layered GO membrane increases and with **W**= 16.0 and 24.0 Å, the membrane shows 100 % rejection. The variation of draw solute rejection of layered GO membranes with different values of **H** (Figure 5-10b) follows the opposite trend to that in the variation in water permeance (Figure 5-8a). As **H** increases from 8.0 Å to 12.0 Å, the draw solute rejection decreases. But with further increase in **H**, the draw solute rejection of the membrane increases. Figure 5-10c shows the variation of draw solute rejection of the layered GO membranes with different values of **C** (draw solution concentration). As **C** increases, the corresponding draw solute rejection of the membrane also slightly increases.

5.4 Conclusions

The potential application of layered GO membrane in dehydration of acetic acid through FO process is investigated using non-equilibrium MD simulations. Layered GO membranes composed of GO nanosheets of smaller lateral dimensions (or with smaller value of **W**) found to have higher water permeance and lower salt rejection as compared to GO membranes composed of nanosheets of larger lateral dimensions. However, the variation of water permeance and salt rejection with interlayer distance (**H**) is not unidirectional in nature. For the layered GO membrane the water permeance increases and salt rejection decreases as the value of **H** increases from 8.0 Å to 12.0 Å. However, with further increase in **H** from 12.0 Å to 18.0 Å, the water per-

meance decreases and salt rejection increases. Here, factors like permeation distance through the membrane, diffusivity of water inside the membrane and water structure inside the membrane play an important role in determining the performance of the membrane. With the increase in draw solution concentration (for the same feed solution concentration) the water permeance through the layered GO membranes increases because of the increase in the transmembrane osmotic pressure. However, the effect of draw solution concentration on the draw solute rejection is much less; which shows a variation of < 2.0 % in the present simulation study.

With the appropriate tuning of the sizes of the GO nanosheets and interlayer spacings, the layered GO membrane could be a suitable candidate for acetic acid dehydration through forward osmosis process. However, the feed solution considered in the present simulation study is 20.0 $wt.\%$ aqueous acetic acid solution. But there are many practical scenarios where the concentration of acetic acid can be much higher. It will be interesting to investigate the performance of layered GO membranes in those scenarios provided suitable draw solutions with very high osmotic pressure are available. Similarly, the effect of the presence of various functional groups on the FO performance of layered GO membranes could also be investigated in the future. We believe that the observations reported in the present study would be helpful for future studies and investigations on the applicability of layered GO membranes in various FO applications.

Chapter 6

Influence of the Presence of the Cations on the Water and Salt Dynamics Inside Layered Graphene Oxide (GO) Membranes[3]

6.1 Introduction

With the rapid growth of human population and industrialization, the demand for usable water is continuously increasing. Considering the fact that only 0.3 % of water available on our planet can be accessed and used, there is an urgency in the research community to look for alternative water resources (e.g. sea water desalination, waste water purification) and innovative and efficient water purification technologies. In that aspect membrane separation technology emerges as one of the efficient water purification (or separation) methods. In the past few decades a variety of membrane materials were extensively been investigated for desalination and water purification applications e.g. polyamide membrane [310, 311, 312], ceramic and zeolite based membranes [8], covalent organic framework (COF) [313, 314, 315, 316, 317, 318],

[3]A. Gogoi, K. A. Reddy, and P. Mondal. Influence of the presence of cations on the water and salt dynamics inside layered graphene oxide (GO) membranes. *Nanoscale*, 12(13):7273-7283, 2020.

nanoporous two-dimensional (2D) material such as graphene, graphene oxide (GO), molybdenum disulfide (MoS_2) [9, 10, 11, 12, 13, 14, 15] etc. Out of these membrane materials, GO has extensively been studied for various separation and transport applications owing to its ultrathin 2-D structure and controllable surface chemistry [15, 25, 32, 319, 320, 321, 322, 323, 324, 325, 326, 327, 328].

Although previous experimental and numerical investigations reported excellent separation ability of GO membrane, its stability in aqueous environment is still a challenging issue for practical applications. One of the reasons for this is the undesirable swelling of layered GO membrane in aqueous environment [329, 330, 331, 332]. When freestanding GO laminates are immersed in aqueous environment the hydration effect breaks the hydrogen bonding between the GO nanosheets and consequently the interlayer spacing between the GO nanosheets increases leading to membrane swelling. The intercalation of water molecules inside the interlayer spacings of GO nanosheets can increase the interlayer spacings of layered GO membrane up to 1.4-7.0 nm [19, 23, 333, 334, 335]. This can severely affects the performance of the membrane. So, increasing the stability of GO laminates is one of the important aspects in the construction of layered GO membranes [336, 337, 338]. The typical pore size of a nanofiltration membrane is around 1 nm which effectively rejects divalent salts and organic molecules present in water stream [339, 340]. On the other hand, although layered GO membrane can effectively rejects large organic molecules [341, 342], its rejection towards slat ions is less as compared to nanofiltration membranes [123, 343, 344]. More specifically its rejection ability towards small ions viz; Na^+, K^+, Li^+, is not up to the desired requirement because of undesirable membrane swelling [28, 345].

In recent years a number of strategies have been proposed to arrest the swelling of GO laminates in aqueous environment or to tune the interlayer spacing of layered GO membrane for specific separation applications. These include intercalation of large nanomaterials [28, 346], cross-linking large and rigid molecules [32, 279, 329, 344, 347, 348, 349, 350, 351, 352, 353, 354], reduction of the GO nanosheets [93, 105, 355, 356, 357, 358, 359], physical confinement of the GO laminates [16, 360], electrochemical

oxidation of graphite to produce GO [361]. Along with these, other strategies like chemical modification of GO nanosheets and external pressure regulations were also been investigated to address the issue of undesirable swelling of layered GO membrane [322, 342, 362, 363, 364, 365, 366, 367, 368].

However, the long term industrial scale applicability of these methods are still sceptical primarily due to scalability issue. Apart from this a fully cross-linked GO laminates can suffers from significantly lower water flux [344] and the interlayer spacing of cross-linked layered GO membrane may not be small enough to rejects salt ions efficiently [20, 369, 370]. The reduction of the GO nanosheets may lead to significant decrease in the water flux along with the decrement in surface hydrophilicity and antifouling properties [370]. Inevitably, to reduce the interlayer spacing of GO laminates to the extent for the rejection of small ions (e.g. Na^+, Li^+, K^+ etc.) is still a topic of great interest among the research community[31, 93].

One of the interesting ways to impart stability to layered GO membranes in aqueous environment is the intercalation of cations in the GO laminates [31, 279, 280]. Chen *et al.* [31] demonstrated that cations (K^+ Na^+, Ca^{2+}, Li^+ and Mg^{2+}) can be used to fix the interlayer spacing of freestanding layered GO membranes by intercalating them inside the interlayer gallery of GO laminates. This is an interesting and, at the same time encouraging observation considering the fact that there are abundance of these ions (K^+ Na^+, Ca^{2+}, Li^+ and Mg^{2+}) in sea water. If the intercalation of these ions imparts stability to GO laminates and tunes the interlayer spacings then layered GO membrane could be an efficacious candidate for sea water desalination.

However, the effect of these ions on the water dynamics through layered GO membrane is still not been addressed yet. The intercalation of cations tune the interlayer spacings of GO laminates and thereby can increase/decrease the water flux [31, 280]. But apart from this, the presence of the cation itself can effect the dynamics of the water through the GO laminates. Water being a polar solvent, the intercalated cations can play an important role in determining the water dynamics inside the interlayer gallery apart from just tuning the interlayer spacings of layered GO membrane. So, in this present study we investigated the effect of intercalated cations on the water dy-

namics through layered GO membranes using molecular dynamics (MD) simulations. The layered GO membranes are intercalated with K^+ and Mg^{2+} ions separately and the performance of these membranes are compared with their corresponding pristine layered GO membranes (not intercalated with cations).

6.2 Methodology

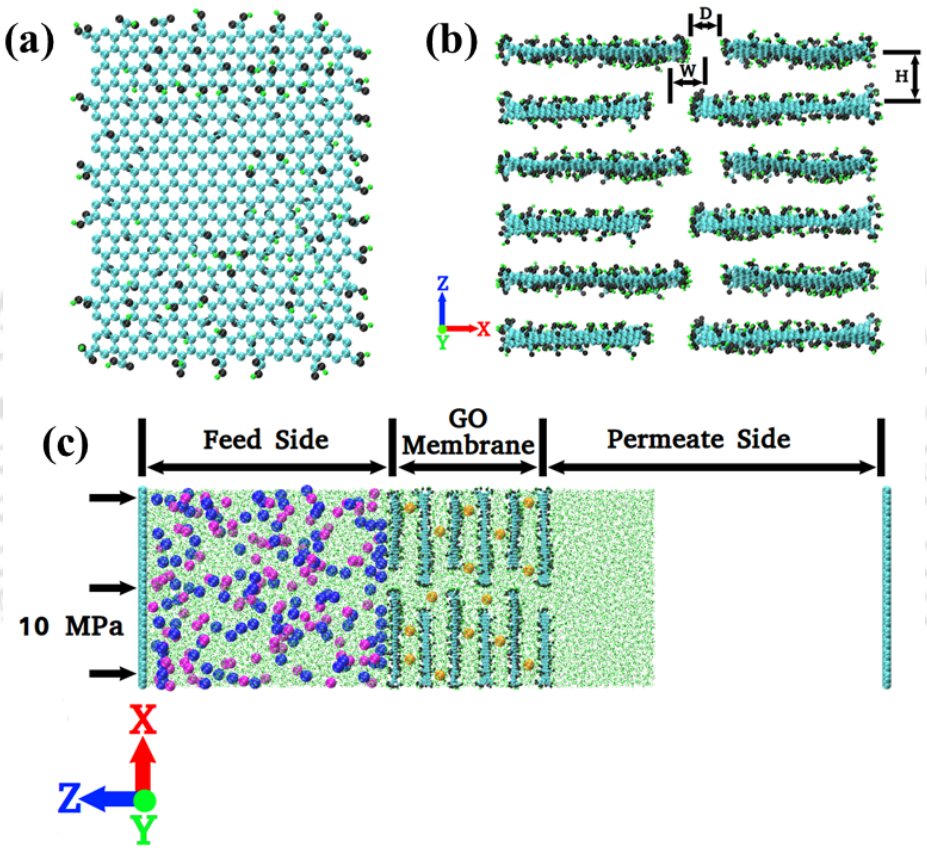

Figure 6-1: (a) GO nanosheet. (b) Layered GO membrane. (c) Simulation setup (for RO). Green color is for hydrogen atoms, black color is for oxygen atoms, cyan color is for carbon atoms, blue color is for Cl^- ions, magenta color is for Na^+ ions, orange color is for K^+ ions.

In this present study, cation (K^+ or Mg^{2+}) intercalated layered GO membrane is tested both in reverse osmosis (RO) and forward osmosis (FO) mode to investigate the effect of the presence of the cations on water dynamics through layered GO membrane. To prepare the membranes for the simulations, first GO nanosheets are

constructed using Visual Molecular Dynamics (VMD) [293] and Avogadro [294]. The GO nanosheet is modeled by considering hydroxyl and epoxy functional groups on the basal plane and carboxyl functional groups at the edges [5, 46]. The chemical composition of the GO nanosheet is $C_{10}O_1(OH)_1(COOH)_{0.5}$ [35, 5, 46, 296, 371]. A representative image of the GO nanosheet is shown in Figure 6-1a. The sizes of the GO nanosheets are 39×48 Å^2 and 31×48 Å^2. With these GO nanosheets, layered GO membrane is constructed as shown in Figure 6-1b.

The parameters **D**, **W** and **H** are the geometric parameters of the membrane which are pore width, pore offset distance and interlayer distance respectively. In this present study the values of **D** and **W** are 7 Å and 8 Å respectively. For **H**, two values are considered based on the experimental observations of Chen *et al.* [31]. For K^+ intercalated layered GO membrane, the value of the parameter **H** is 11.4 Å. On the other hand, for GO membrane intercalated with Mg^{2+} ions, the value of **H** is 13.6 Å. The performance of these two cation intercalated membranes are compared with their corresponding pristine GO membranes to get an insight into the effect of the presence of these cations on the water dynamics through GO laminates.

Table 6.1: Configurations of the layered GO membranes considered in the present study and their corresponding abbreviations

Geometric Parameters			Ion Intercalated	Membrane abbreviations
D (Å)	**W (Å)**	**H (Å)**		
7.0	8.0	11.4	-	P-GO-11.4
7.0	8.0	11.4	K^+	K-GO-11.4
7.0	8.0	13.6	-	P-GO-13.6
7.0	8.0	13.6	Mg^{2+}	M-GO-13.6

After the construction of the membrane, it is hydrated with a equilibrated water box. For cation intercalated membranes, 15 cations (K^+ or Mg^{2+}) are placed randomly inside the interlayer gallery of the layered GO membranes before hydration. A 0.56 M aqueous NaCl solution is considered as the feed solution to mimic the osmotic pressure of sea water (27 atm). It contains 108 Na^+ ions and 108 Cl^- ions in 10000

water molecules. The simulation setup for RO process in shown in Figure 6-1c. In most of the previous atomistic simulations for RO processes, transmembrane pressures which are almost two order magnitude higher (200 MPa - 600 MPa) than that for practical applications, were used [15, 305, 372, 373, 374]. However, to get an meticulous insight into the salt rejection and water flux through cation intercalated layered GO membranes, a transmembrane pressure of 10 MPa is applied in the present study for RO process. A graphene piston is used for applying this transmembrane pressure on the feed solution (NaCl solution) as shown in Figure 6-1c. The simulation setup for FO process is shown in Figure 6-2. In the FO process, a solution of 3 M $MgCl_2$ and 0.05 M $Al_2(SO_4)_3$ is used as the draw solution [283, 297]. It contains 594 Mg^{2+} ions, 1188 Cl^- ions, 20 Al^{3+} ions and 30 SO_4^{2-} ions.

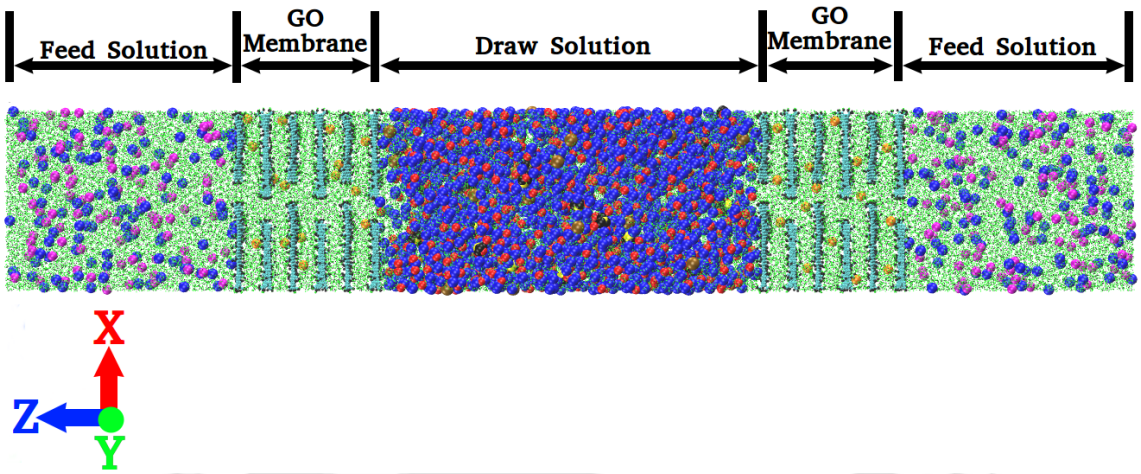

Figure 6-2: Simulation setup forward osmosis (FO). Green color is for hydrogen atoms, black color is for oxygen atoms, cyan color is for carbon atoms, blue color is for Cl^- ions, magenta color is for Na^+ ions, orange color is for K^+ ions.

In this present study, all the MD simulations are performed using NAMD 2.11 [285] with OPLS-AA force field [45] and SPC water model [286]. The bond length of the water molecules are constraint using SETTLE algorithm [287]. For computing the van der Waals interactions, Lennard-Jones potential is used with a cut-off distance of 12.0 Å. The long range electrostatic interactions are computed using Particle mesh Ewald (PME) method [288].

After the construction of the simulation system, it is energy minimized to remove

any internal stress within the system. The system is then equilibrated for 1 ns at a temperature of 300 K and 1 atm pressure. Pressure is controlled using modified Nosé-Hoover method with a barostat oscillation time and damping factor of 0.3 ps. For controlling the temperature, Langevin dynamics is used with a damping factor of 5 ps^{-1}. After equilibration, the production runs are performed for 20 ns at a constant temperature of 300 K. The carbon atoms at the corner of the GO nanosheets were fixed during the simulations to [305, 306] to maintain a layered structure of the membrane. For the simulations of RO processes, periodic boundary conditions (PBC) are applied along X and Y dimensions. Along the Z dimension, an empty space of 30 Å in length is applied both at the top and bottom of the simulation system. On the other hand, for the simulation of FO processes, PBC are applied in all the directions. For each of the simulation systems, 3 independent simulations are performed with different initial configurations and the results are averaged over these independent simulations.

6.3 Results and Discussion

In this present work we made a comparative study on the performance of ion intercalated layered GO membranes and pristine GO membranes in RO and FO processes for separation applications. The membrane performance is based on the water flux through the membrane and its ability to reject salt and unwanted species present in the feed water.

As described in the previous section, in this present work a transmembrane pressure of 10 MPa (which is of the same order of the transmembrane pressure typically used in a RO plant) is applied for the RO process to get a more realistic insight into the water permeation dynamics through the cation intercalated and pristine layered GO membranes. Due to the application of lower simulation transmembrane pressure some fluctuations are observed in the kinetic permeation curves (Figure 6-3). The kinetic permeation curves (Figure 6-3) show the variation in the number of water molecules in the permeate side ($\boldsymbol{N_P}$) with simulation time. It is observed that

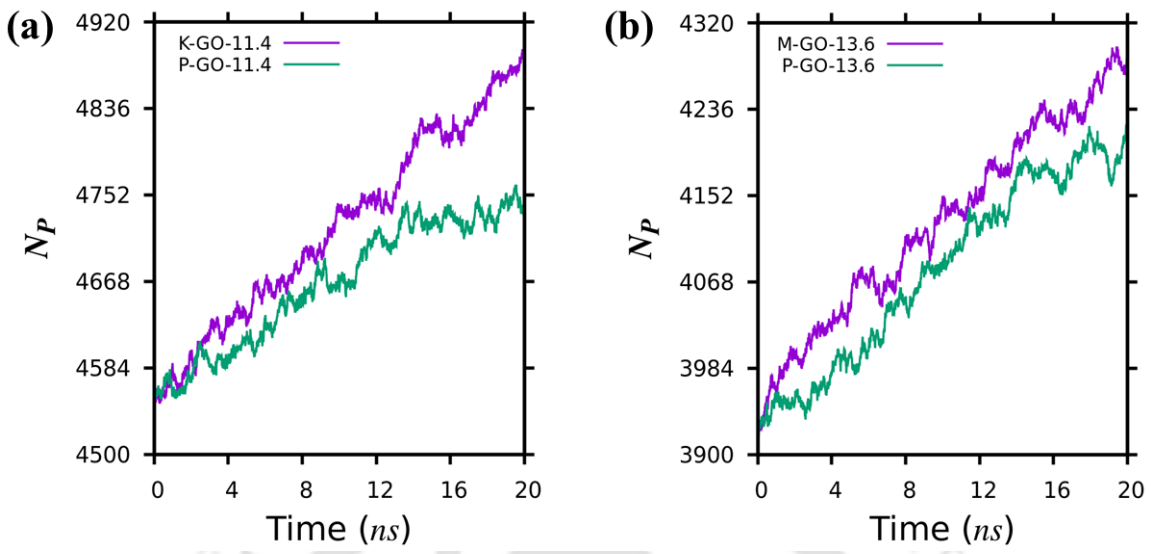

Figure 6-3: Variation of number of water molecules in the permeate side ($\boldsymbol{N_P}$) with time for RO.

$\boldsymbol{N_P}$ is more for cation intercalated layered GO membranes (K-GO-11.4/M-GO-13.6) as compared to pristine layered GO membranes (P-GO-11.4/P-GO-13.6) within the specified simulation time of 20 ns in this present study.

Figure 6-4a and 6-4b show the water flux through layered GO membranes in RO and FO separation processes respectively. Interestingly, in both the processes it is observed that for the same interlayer distance, the cation (K^+ or Mg^{2+}) intercalated layered GO membranes (K-GO-11.4 and M-GO-13.6) show higher water flux than the corresponding pristine layered GO membrane (P-GO-11.4 and P-GO-13.6). The water flux reported in Figure 6-4a and 6-4b is very high as compared to experimental observations. Typically the water flux reported in atomistic simulations [10, 289, 296, 375] are much higher (up to a few order of magnitude) as compared to those reported in experimental investigations [32, 104]. This difference in water flux can be attributed to the difference in thickness of the membranes used in simulations to those used in experiments [371, 376]. In atomistic simulations the thickness of the membranes are of the order of few nm, whereas in experimental investigations the thickness of the membrane ranges from hundreds of nm to few μm. With the increase in thickness of the membrane, its water flux decreases [104, 371, 376]. That is why

the water flux obtained through atomistic simulations are very high as compared to experimental observations. However, in this present study we are less concerned about this difference and more interested in the relative performance of the cation intercalated layered GO membranes and their corresponding pristine GO membranes.

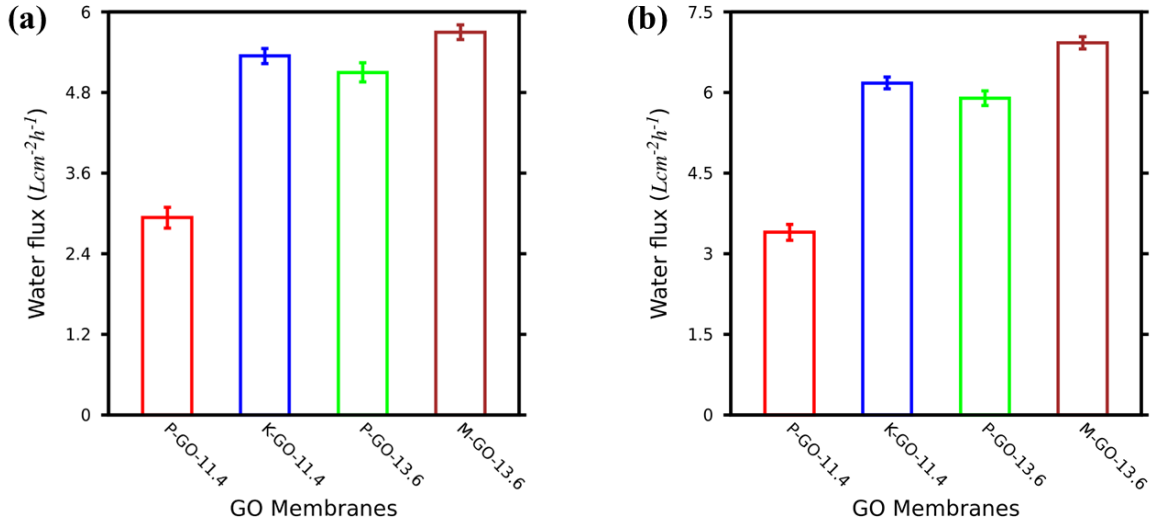

Figure 6-4: Water flux through layered GO membranes for (a) RO and (b) FO.

The dynamics of the hydrogen bond network inside the layered GO membranes, play an important role in determining the water flux through the membranes. In this present study, the dynamics of the hydrogen bond network inside the layered GO membrane is investigated by calculating the survival probability or lifetime of hydrogen bond from the long time decay of following autocorrelation functions [377, 378, 379, 380]:

$$\mathbf{C(t)} = \frac{< \eta_{ij}(t)\,\eta_{ij}(0) >}{\eta_{ij}(0)^{2}} \cong exp\{-\frac{t}{\tau_{\mathrm{HB}}}\} \tag{6.1}$$

where

$$\eta_{ij}(t) = \begin{cases} 1 & \text{If there is a H bond between molecules i and j at times 0 and } t \text{ and the bond has not been broken for any period longer than } t^* \\ 0 & \text{Otherwise} \end{cases}$$

The limiting cases $t^* = 0$ and $t^* = \infty$ correspond to continuous ($\mathbf{C_C(t)}$) and intermittent ($\mathbf{C_I(t)}$) H bond autocorrelation functions respectively.

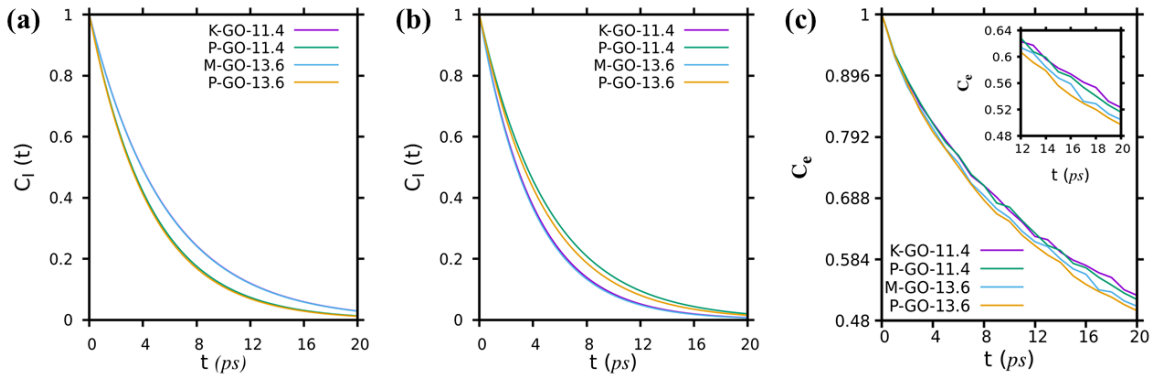

Figure 6-5: Intermittent H bond autocorrelation function between (a) water molecules and (b) water and GO. (c) Water reorientation dynamics inside the interlayer gallery of layered GO membranes.

Figure 6-5a and 6-5b show the plots for $\mathbf{C_I(t)}$ for hydrogen bond network between water molecules and between water and GO, inside the interlayer gallery of layered GO membranes, respectively. The dynamics of water-water H bond is slower inside the interlayer gallery of cation intercalated layered GO membrane as compared to pristine one as shown in Figure 6-5a. This suggests that the H bond network between water molecules is more stable for cation intercalated layered GO membrane than the corresponding pristine one. This stable H bond network between water molecules leads to increase in water permeation through the cation intercalated layered GO membrane as compared to the pristine one as observed in Figure 6-4a and 6-4b. This

observation is in accordance with the observations reported by Suk and Aluru [70] (comparative study between ultrathin graphene and CNT based membranes). On the other hand, $\mathbf{C_I(t)}$ for H bond between water and GO decays slower for pristine GO membranes as compared to cation intercalated membrane (Figure 6-5b). So, the H bond network between water and GO is more stable in pristine GO membrane as compared to cation intercalated membrane. This leads to slow permeation of water molecules through the interlayer gallery of pristine GO membrane as compared to cation intercalated one, which is also in accordance with the observations of Figure 6-4a and 6-4b. The plots for continuous H bond autocorrelation function ($\mathbf{C_C(t)}$) follow the same trend as $\mathbf{C_I(t)}$ and are reported in Figure 6-6.

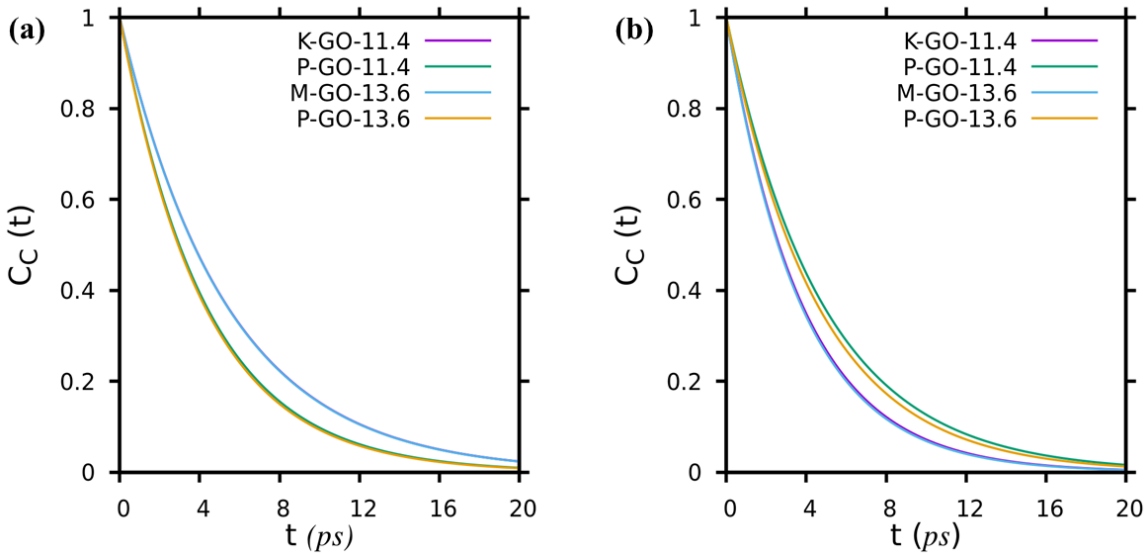

Figure 6-6: Continuous H bond autocorrelation function between (a) water molecules (b) water and GO.

The reorientability of water molecules [381, 382] inside the interlayer gallery of layered GO membranes is calculated based on the following autocorrelation functions for water dipole:

$$\mathbf{C_e} = < P_2[\, e(t)\, e(0)\,] > \tag{6.2}$$

where e is an unit vector along the dipole vector, $P_2(x) = (3x^2 - 1)/2$ is the second order Legendre polynomial and $\mathbf{C_e}$ is the dipole relaxation function. The variation of

$\mathbf{C_e}$ with time gives us an idea on "how fast" the water molecules are rotating/changing directions. If $\mathbf{C_e}$ decays very fast, we can assume that the water molecules are rotating/changing directions very fast. On the other hand, if $\mathbf{C_e}$ is stable, we can assume that the water molecules are rotating/changing directions very slowly. As shown in Figure 6-5c, $\mathbf{C_e}$ decays at a faster rate for pristine layered GO membranes as compared to the corresponding cation intercalated layered GO membranes. So, for cation intercalated layered GO membranes, water molecules inside the interlayer gallery rotate/change direction slowly as compared to the water molecules inside the interlayer gallery of pristine layered GO membranes. The frequent rotation/change in directions of the water molecules can lead to the disruption of the H bond network among the water molecules. This in turn reduces the water permeability through the layered GO membranes. Because of this, the cation intercalated layered GO membranes show higher water permeability as compared to the corresponding pristine layered GO membranes as reported in Figure 6-4a and 6-4b.

The slow reorientability of the water molecules inside the interlayer gallery of the cation intercalated layered GO membranes also reflects on the more compact arrangement of water molecules inside the interlayer gallery as depicted in Figure 6-7a and 6-7b.

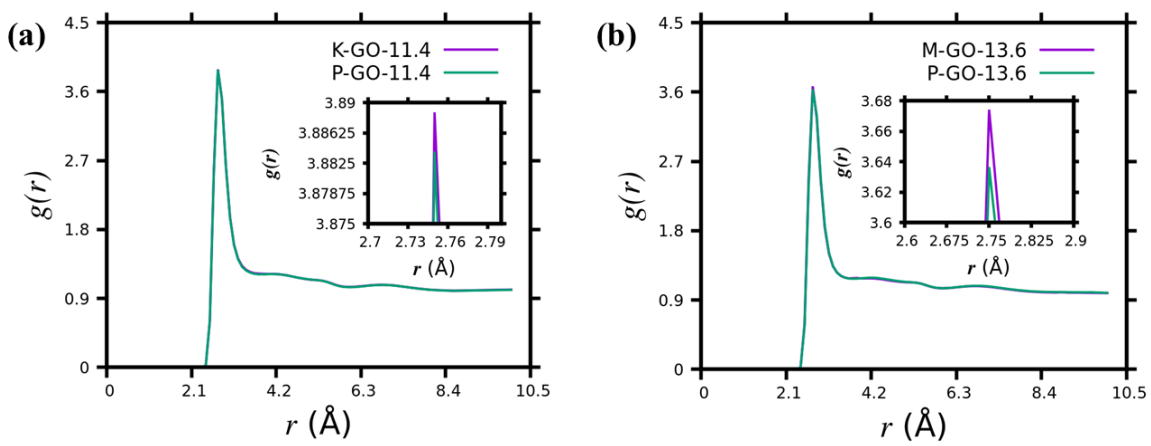

Figure 6-7: Radial distribution function ($g(r)$) between the oxygen atoms of water inside the layered GO membranes (a) K-GO-11.4 and P-GO-11.4 and (b) M-GO-13.6 and P-GO-13.6.

Figure 6-7a and 6-7b show the radial distribution function between the oxygen atoms of water inside the layered GO membranes. For all the cases shown in Figure 6-7a and 6-7b, the first peak of $g(r)$ is observed at 2.75 Å. However, for cation intercalated layered GO membranes (K-GO-11.4 and M-GO-13.6), the intensity of this peak slightly increases as depicted in the insets of Figure 6-7a and 6-7b. This indicates that the water molecules inside the layered GO membranes have slightly higher compact arrangement in the presence of the cations.

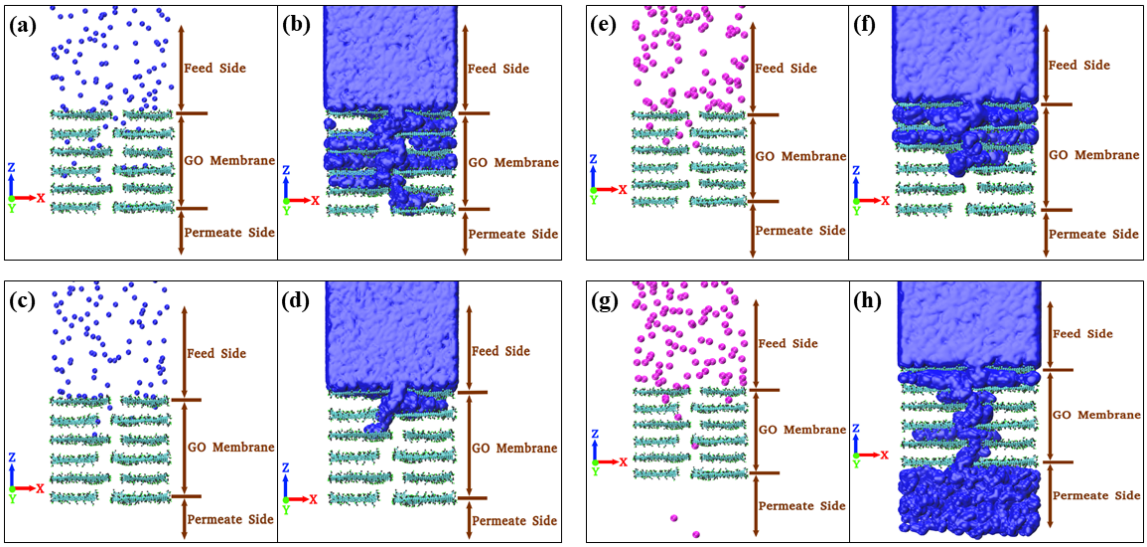

Figure 6-8: Permeability of Na^+ and Cl^- ions through layered GO membranes. (a) Distribution of Cl^- ions at the end of the simulation for K-GO-11.4 membrane system. (b) Spatial distribution of Cl^- ions for K-GO-11.4 membrane system. (c) Distribution of Cl^- ions at the end of the simulation for P-GO-11.4 membrane system. (d) Spatial distribution of Cl^- ions for P-GO-11.4 membrane system. (e) Distribution of Na^+ ions at the end of the simulation for K-GO-11.4 membrane system. (f) Spatial distribution of Na^+ ions for K-GO-11.4 membrane system. (g) Distribution of Na^+ ions at the end of the simulation for P-GO-11.4 membrane system. (h) Spatial distribution of Na^+ ions for P-GO-11.4 membrane system.

Considering the thickness of the membrane used in the simulation and the timescale of the simulation, the salt rejection ability of the layered GO membranes in this present study is compared to one another based on "*the number of salt ions intercalated inside the membrane from the feed solution and how far these ions have intercalated inside the membrane*". Figure 6-8a shows the distribution of Cl^- ions for

K-GO-11.4 membrane system at the end of the simulation and Figure 6-8b shows the spatial distribution of Cl^- ions for K-GO-11.4 membrane system. Similarly, Figure 6-8c and 6-8d depict the distribution of Cl^- ions for P-GO-11.4 membrane system at the end of the simulation and the spatial distribution of Cl^- ions for P-GO-11.4 membrane system respectively. The distribution of ions at the end of the simulation (its a snapshot at the end of the simulation) gives an idea on the number of ions intercalated inside the membrane. On the other hand, the spatial distribution of the ions gives an idea on how far the ions have intercalated inside the membrane and the path the ions have traversed through the membrane during the entire course of the simulation. It is observed that K-GO-11.4 membrane is more permeable for Cl^- ions as compared to P-GO-11.4 membrane. For K-GO-11.4 membrane system 17 Cl^- ions intercalated inside the membrane and these ions traversed to the end of the membrane (towards permeate side) as shown in Figure 6-8b. On the other hand, for P-GO-11.4 membrane system 5 Cl^- ions entered inside the membrane and the movement of these ions are restricted to the second layer (from the feed side) of the interlayer gallery as shown in Figure 6-8d. Figure 6-8e and 6-8f show the distribution of Na^+ ions and spatial distribution for Na^+ ions for K-GO-11.4 membrane system respectively. Similarly, Figure 6-8g and 6-8h show the distribution of Na^+ ions and spatial distribution of Na^+ ions respectively for P-GO-11.4 membrane system. For K-GO-11.4 membrane system, 5 Na^+ ions intercalated inside the membrane but the movement of these ions are restricted to only third layer (from the feed side) of the interlayer gallery of the membrane (Figure 6-8f). On the other hand, for P-GO-11.4 membrane system 7 Na^+ ions intercalated inside the membrane out of which 2 Na^+ ions completely permeated through the membrane. As can be seen from Figure 6-8h, Na^+ ions from the feed solution traverse the complete permeation length through the interlayer gallery of P-GO-11.4 membrane system. So, Na^+ ion is more permeable for P-GO-11.4 membrane system as compared to K-GO-11.4 membrane system. This may be attributed to the K^+ ions located in the interlayer gallery of K-GO-11.4 membrane system, which repel (electrostatic repulsion) the invading Na^+ ions from the feed solution, thereby making K-GO-11.4 membrane system less permeable to Na^+

ions as compared to P-GO-11.4 membrane system. The distribution of Na^+ and Cl^- ions and their spatial distribution for M-GO-13.6 and P-GO-13.6 membrane systems are reported in Figure 6-9.

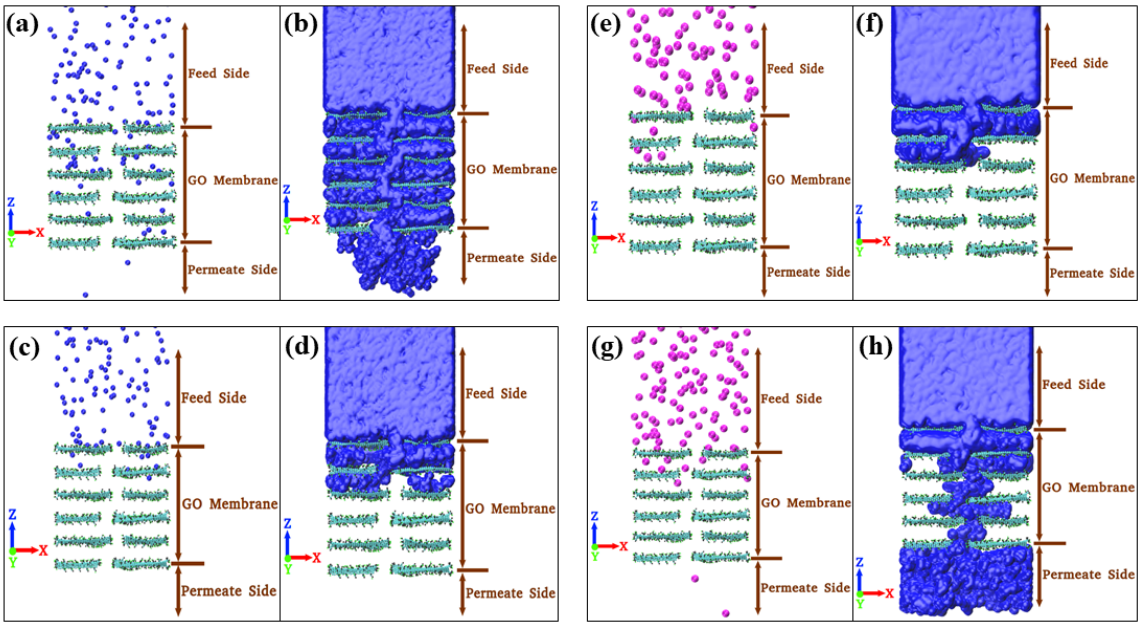

Figure 6-9: (a) Distribution of Cl^- ions at the end of the simulation for M-GO-13.6 membrane system. (b) Spatial distribution function of Cl^- ions for M-GO-13.6 membrane system. (c) Distribution of Cl^- ions at the end of the simulation for P-GO-13.6 membrane system. (d) Spatial distribution function of Cl^- ions for P-GO-13.6 membrane system. (e) Distribution of Na^+ ions at the end of the simulation for M-GO-13.6 membrane system. (f) Spatial distribution function of Na^+ ions for M-GO-13.6 membrane system. (g) Distribution of Na^+ ions at the end of the simulation for P-GO-13.6 membrane system. (h) Spatial distribution function of Na^+ ions for P-GO-13.6 membrane system.

To get an insight into the ease of permeation of the ions (Na^+ and Cl^-) and water molecules through the layered GO membranes, PMF calculations are performed using umbrella sampling method [307] with replica exchange molecular dynamics (REMD-US). The relative z distance between the permeating species and center of the membrane (GO laminates) along the membrane axis (i.e. along the permeation direction) is chosen as the reaction coordinate. The width of the umbrella window is 1 Å for the reaction coordinate. The data obtained through REMD-US are analyzed via weighted histogram analysis method [308] to generate the PMF. However, the

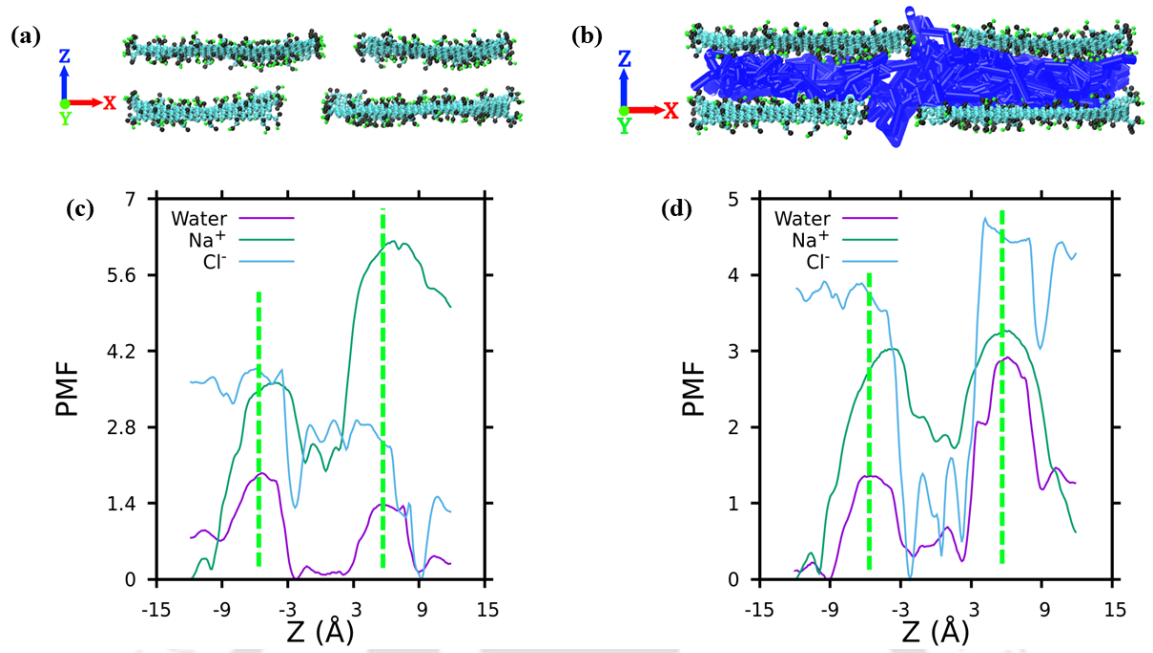

Figure 6-10: (a) GO laminates considered for PMF calculations. (b) Representative trajectory of a permeating molecule for which PMF is being calculated. (c) PMF for K-GO-11.4 membrane system. (d) PMF for P-GO-11.4 membrane system. The entry and exit points of the permeating species through the GO laminates are shown with a pair of dotted green lines.

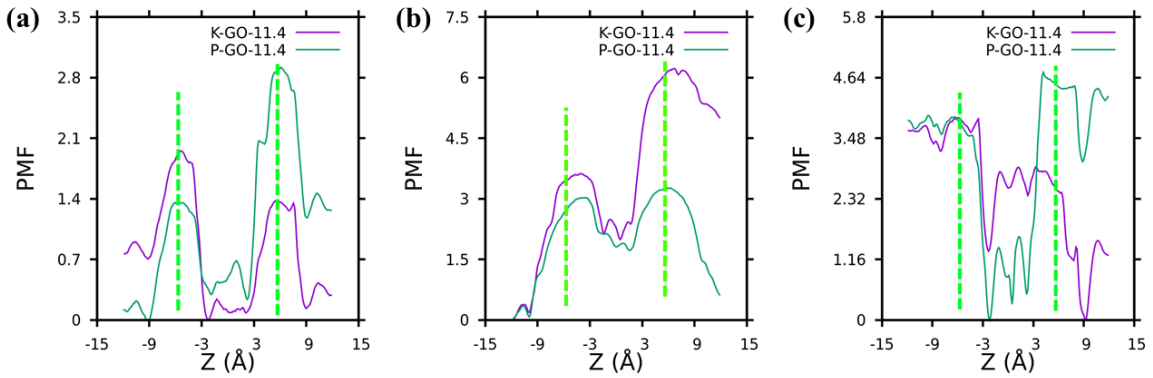

Figure 6-11: Comparison of PMF between K-GO-11.4 and P-GO-11.4 membrane systems for (a) Water, (b) Na^+ ions and (c) Cl^- ions. The entry and exit points of the permeating species through the GO laminates are shown with a pair of dotted green lines.

calculation of PMF (in particular with umbrella sampling) is a computationally very expensive process. So, to comply with the computational cost, in the present study,

a two layered structure of the GO laminates is used for PMF calculations as shown in Figure 6-10a. This two layer structure of GO laminates can be considered as the minimum repeating unit of the layered GO membrane shown in Figure 6-1b. The representative trajectory of a permeating molecule (for which PMF is being calculated) through this two layered structure of GO laminates is shown in Figure 6-10b. Figure 6-10c and 6-10d show the PMF for water, Na^+ ion and Cl^- ion for K-GO-11.4 membrane system and P-GO-11.4 membrane system respectively. For both the membrane system (K-GO-11.4 and P-GO-11.4) water can easily permeate through the interlayer gallery of the layered GO membranes as compared to Na^+ and Cl^- ions. For K-GO-11.4 membrane system, Na^+ ions face higher barrier to permeate through the membrane as compared to Cl^- ions and water as shown in Figure 6-10c. On the other hand, for P-GO-11.4 membrane system Cl^- ions find it more difficult to permeate through the interlayer gallery of layered GO membrane as compared to Na^+ ions and water (Figure 6-10d).

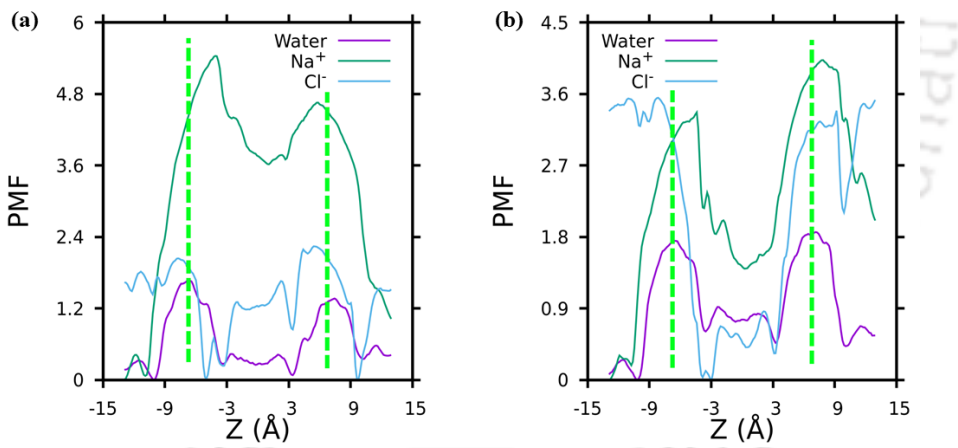

Figure 6-12: (a) PMF for M-GO-13.6 membrane system. (b) PMF for P-GO-13.6 membrane system. The entry and exit points of the permeating species through the GO laminates are shown with a pair of dotted green lines.

The location of minima and maxima of the PMF plots for water and Na^+ ions follow more or less the same trend as shown in Figure 6-11a and 6-11b respectively. As observed in Figure 6-11a, the water molecules find it more difficult to permeate through P-GO-11.4 membrane system as compared to K-GO-11.4 membrane system.

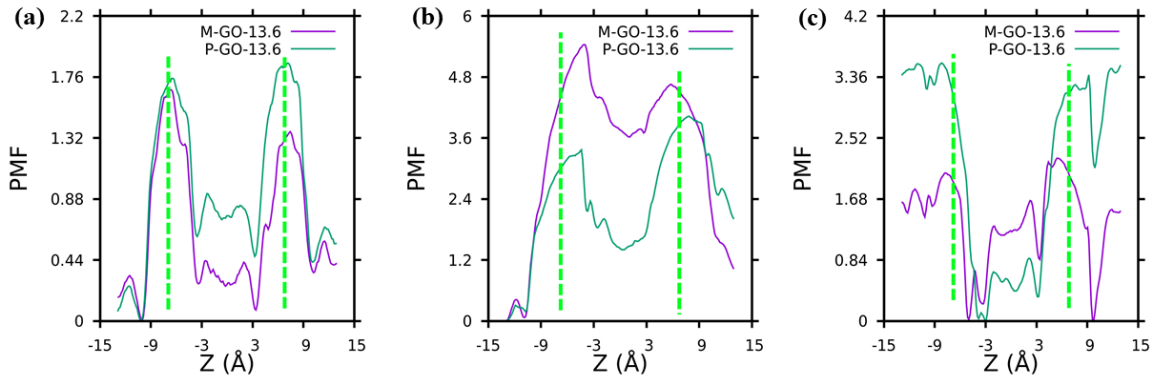

Figure 6-13: Comparison of PMF between M-GO-13.6 and P-GO-13.6 membrane system for (a) Water, (b) Na^+ ions and (c) Cl^- ions. The entry and exit points of the permeating species through the GO laminates are shown with a pair of dotted green lines.

On the other hand, Figure 6-11b shows that Na^+ ions can permeate through P-GO-11.4 membrane system with relative ease as compared to K-GO-11.4 membrane system. Figure 6-11c shows the PMF plots for Cl^- ions for K-GO-11.4 and P-GO-11.4 membrane system. A careful observation of the PMF plots for Cl^- ions will reveal that, although Cl^- ions cross the entrance barrier of the GO laminates with relative ease, inside the interlayer gallery there exist certain significant minima where they prefer to inhabit for a longer duration of time. For K-GO-11.4 membrane system, one such minima is located at -2.33 Å which lies within the interlayer gallery of the GO laminates. For the same membrane another such minima is located at 9.13 Å which lies outside the interlayer gallery. On the other hand, for P-GO-11.4 membrane system these minima are observed at -2.06 Å, 0.47 Å, 2.33 Å which are located inside the interlayer gallery of the two GO laminates. Another such minima is observed at 8.87 Å which lies outside the interlayer gallery. The more number of these minima in P-GO-11.4 membrane system makes it difficult for the Cl^- ions to permeate through the membrane as compared to K-GO-11.4 membrane system. Another important observation from the PMF plots for water, Na^+ and Cl^- ions is that while water and Na^+ ions find the permeation barrier at the entrance of the GO laminates (Figure 6-11a and 6-11b), the Cl^- ions find the permeation barrier predominantly inside the

interlayer gallery (Figure 6-11c) of the GO laminates. The PMF plots for M-GO-13.6 and P-GO-13.6 membrane systems are reported in Figure 6-12 and 6-13.

6.4 Conclusions

In summary we have investigated the effect of the presence of cations in the interlayer gallery of layered GO membrane on its performance with MD simulations. The presence of the cations increases the compact arrangement of water molecules inside the interlayer gallery of layered GO membranes. It also improves the stability in the hydrogen bond network among the water molecules located inside the interlayer gallery of layered GO membranes. This can be attributed to the slow reorientability of the water molecules inside the GO membrane in the presence of cations. All these changes synergistically lead to the increase in water flux through cation intercalated layered GO membranes as compared to corresponding pristine layered GO membranes. The pristine layered GO membranes have higher rejection towards Cl^- ions as compared to Na^+ ions. On the other hand, the cation intercalated (K^+ or Mg^{2+}) layered GO membranes have higher rejection towards Na^+ ions as compared to Cl^- ions. This observation can be attributed to the distinct electrostatic interactions between the cations present inside the membrane and the invading ions. The presence of the functional groups may also play an important role in the rejection of Na^+ and Cl^- ions through layered GO membranes. The amount of cations intercalated inside the layered GO membranes may also be crucial in determining membrane performance and will be investigated in near future. We believe that the observations reported in this present study would encourage further research on the applicability of layered GO membrane in various separation applications and would aid to the experimental investigations on the same.

भारतीय प्रौद्योगिकी संस्थान गुवाहाटी
Indian Institute of Technology Guwahati

Chapter 7

Electroosmotic Flow through Nanochannel with Patterned Surface Charge Distribution: A Molecular Dynamics Study

7.1 Introduction

Liquid transport in micro/nanoscale gained considerable attention from research community owing to its potential applicability in various critical applications ranging from water desalination to drug delivery, energy storage, micro/nanopumping, separation and identifications of biological and chemical species [15, 191, 200, 383, 384, 385, 386, 387, 388]. Transport in the micro/nanoscale can be induced by various means viz. temperature gradient, pressure gradient, surface tension gradient, concentration gradient, applying an electric field etc. [389, 390]. Out of these transport processes, electrokinetic transport has gained considerable research interest owing to its easy controllability in the micro and nanoscale transport processes. When an electrolyte solution comes in contact with a charged surface an electric double layer (EDL) forms near the surface. Depending on the charge type (positive or negative) of the surface,

the EDL has a net positive or negative charge. Now, if an external electric filed is applied in a direction tangential to a surface, the ions in the EDL start to flow in a certain direction (depends on the net charge of the EDL). These flowing ions also drag the fluid molecules along with them which in turn results in electro-osmotic transport.

In the present study, the electro-osmotic flow behaviour through nanochannel with striped charge distribution is studied using non-equilibrium molecular dynamics (MD) simulations. As mentioned earlier, the interfacial hydrodynamics and interactions between the wall and ion species/water molecules in the presence of patterned surface charge distribution is far from being trivial and classical continuum approaches may not be sufficient enough to capture the flow behaviour for the same. In that aspect MD simulations may prove to be handy where all the atomistic interactions are considered explicitly. To the best of the author's knowledge, the atomistic investigations of electro-osmotic flow behaviour in nanochannel with stripe patterned charge distribution has not been reported previously in the literature. The present study focuses on various interactions between the surface of the nanochannel and the water molecules/ion species for different surface charge densities. The role of these interactions and the distribution of the ionic species on the charge density profile (also on the electric double layer) of the nanochannel is being addressed in detail in the following sections.

7.2 Methodology

For the construction of the simulation system, first a graphene sheet of size 100×100 Å^2 is constructed using Visual Molecular Dynamics (VMD) [293]. Then the carbon atoms of the graphene sheet are assigned a certain amount of partial charge to get the desired surface charge density (σ). In this present study 6 different values of σ are considered, viz. 0.005 C/m^2, 0.01 C/m^2, 0.025 C/m^2, 0.05 C/m^2, 0.1 C/m^2 and 0.2 C/m^2 [155, 205, 209, 215, 391, 392]. The charge is distributed in a striping pattern on the graphene surface. So, only a selected number of carbon atoms are assigned

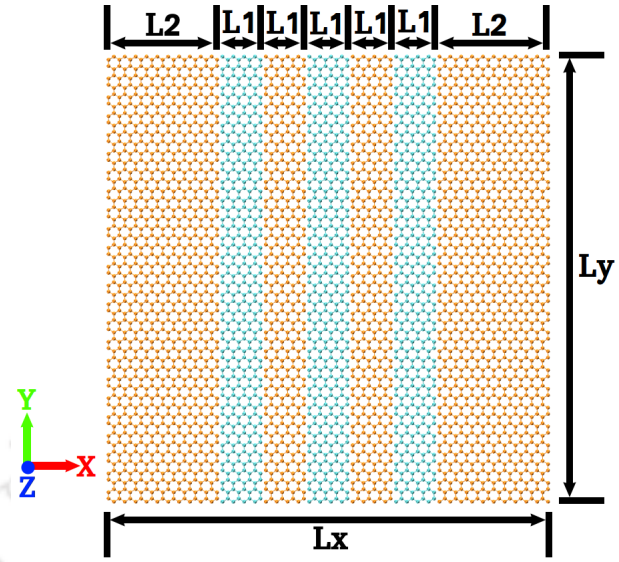

Figure 7-1: Graphene sheet with charged stripes. The orange color is for charged atoms, cyan color is for neutral atoms.

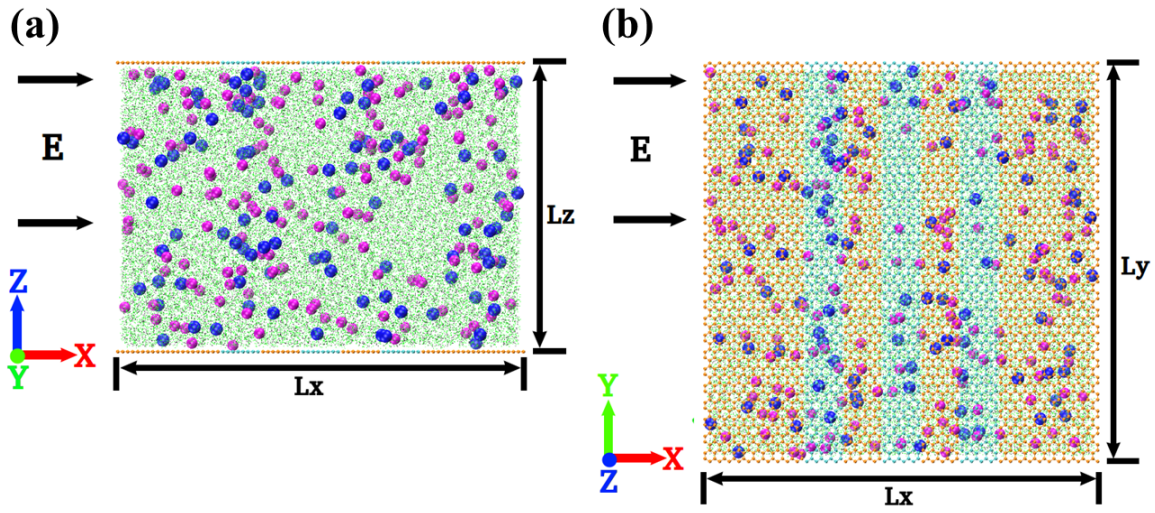

Figure 7-2: Simulation setup. (a) Front view. (b) Top view. The green color is for hydrogen atoms, black color is for oxygen atoms, blue color is for Cl^- ions, magenta color is for Na^+ ions. On the graphene sheet orange color is for charged atoms and cyan color is for neutral atoms.

a certain partial charge to get the striping pattern of charge distribution with the desired σ. Figure 7-1 shows a graphene sheet with striping patterned surface charge distribution. Here, **Lx** and **Ly** both are 100 Å. The value of the parameter **L1** is 10 Å and **L2** is 25 Å.

After the construction of the charged graphene sheets, a rectangular nanochannel is constructed by placing two graphene sheets 71 Å apart i.e. **Lz**= 71 Å in Figure 7-2(a). The simulation setup is constructed by placing a 0.46 M NaCl solution inside the rectangular nanochannel as shown in Figure 7-2. This solution contains 20000 water molecules and 164 Na^+ and Cl^- ions. Additional number of Na^+ ions are added to the system based on the corresponding σ to make the system electrically neutral. Based on the value of σ, each of the simulation setup is assigned a particular abbreviation as tabulated in Table 7.1.

Table 7.1: Surface charge density considered in this present study and corresponding abbreviations

Surface Charge Density (σ) (Cm^{-2})	Abbreviations
0.005	$P_{0.005}$
0.01	$P_{0.01}$
0.025	$P_{0.025}$
0.05	$P_{0.05}$
0.1	$P_{0.1}$
0.2	$P_{0.2}$

The non-equilibrium molecular dynamics (MD) simulations reported in the present study are performed with NAMD 2.11 [285]. All the atomistic interactions are computed using OPLS-AA force field [45]. The water molecules are modeled with SPC water model [286] and their bond lengths are constrained using SETTLE algorithm [287]. The non-bonded interactions have two components: van der Waals interactions and electrostatic interactions. The van der Waals interactions are computed with Lennard-Jones potential with a cut-off distance of 12 Å. The long range electrostatic interactions are computed with particle mesh Ewald (PME) method [288].

Before performing the MD simulations, the system is first energy minimized. The system is then equilibrated for 1 ns at a constant temperature of 300 K and 1 atm pressure. For controlling the pressure, modified Nosé-Hoover method is used with a barostat oscillation time and damping factor of 0.3 ps. Temperature is kept constant with Langevin dynamics with a damping factor of 5 ps^{-1}. During the equilibration

of the simulation system no external electric field is applied. After equilibration, the production runs are performed for 50 ns with a time step of 1 fs. In the production run an external electric field of strength $\mathbf{E}$ is applied along the $+X$ direction as shown in Figure 7-2. In this present study the value of $\mathbf{E}$ is 12.5×10^6 V/m. Such a high electric field may seem to be unrealistic in experiments but is essential in MD simulations to obtain a high velocity signal to noise ratio [155, 209, 393, 394, 395]. During the production run the Langevin dynamics is applied only to the wall atoms (C atoms of the graphene sheets) to maintain a constant temperature of 300 K at the walls. All other molecules and atoms (water and ions) of the simulation system are allowed to move freely under the influence of external electric field to get a more realistic insight into their dynamics in electro-kinetic transport. Simulation data are recorded at every 20 ps for analysis. Periodic boundary conditions are applied along all directions. An empty space of 50 Å is applied along Z direction both at the top and bottom of the simulation system.

7.3 Results and Discussion

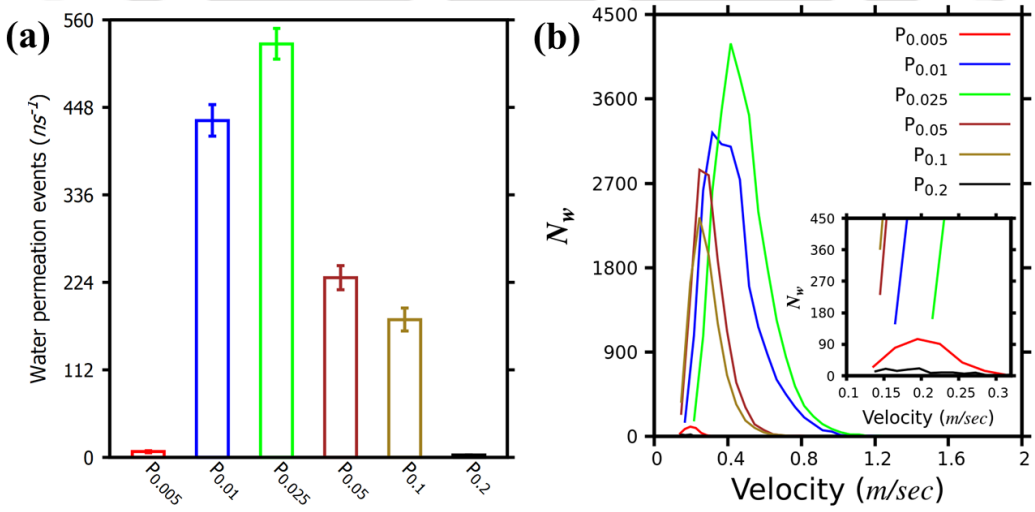

Figure 7-3: (a) Water permeation events through nano-channels. (b) Number distribution of the velocities of the permeating water molecules through the nano-channel.

From the non-equilibrium MD simulations, first we computed the water perme-

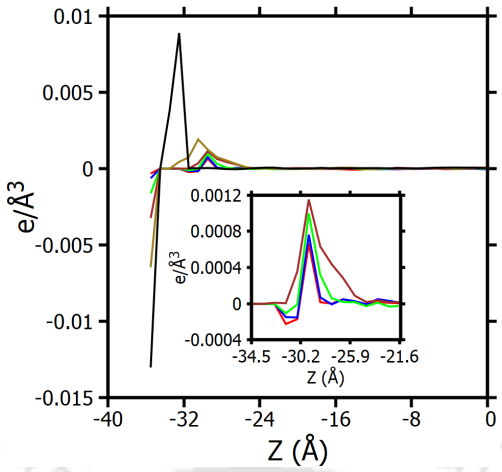

Figure 7-4: Charge distribution along the Z direction for nanochannel with different σ.

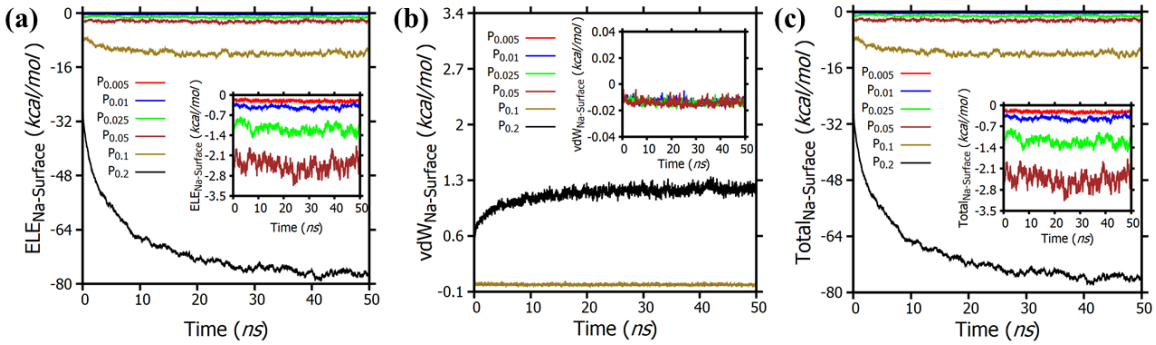

Figure 7-5: Interaction Energy between the wall and the Na^+ ions. (a) Electrostatic interactions. (b) van der Waals interactions. (c) Total interactions.

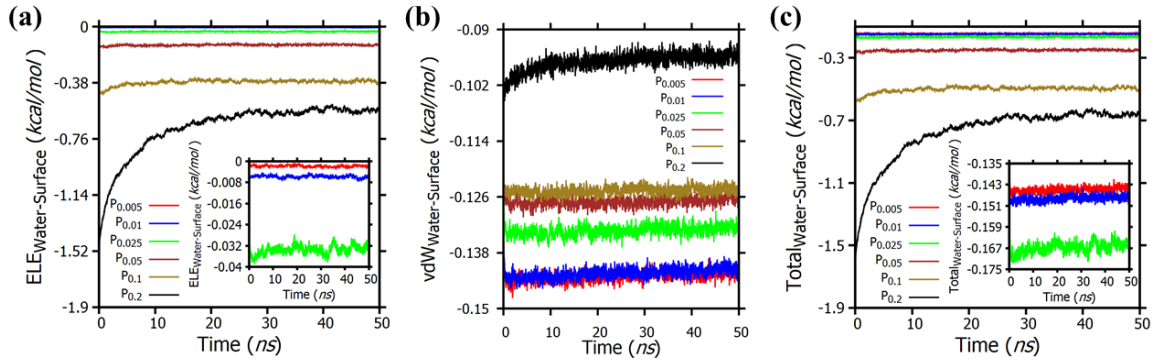

Figure 7-6: Interaction Energy between the wall and water. (a) Electrostatic interactions. (b) van der Waals interactions. (c) Total interactions.

ation events through the nanochannel. If a water molecule permeate through the nanochannel from the extreme left end (i.e. extreme end of the nanochannel along the

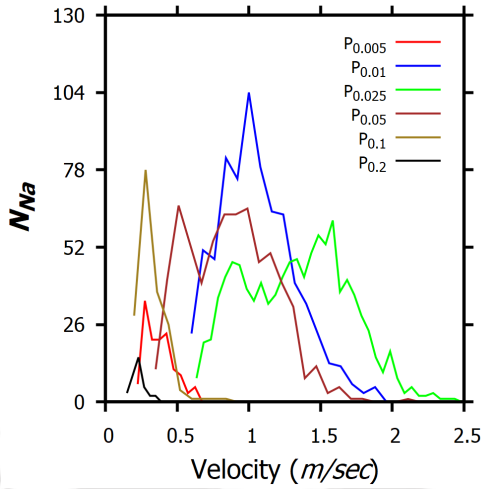

Figure 7-7: Distribution of velocity of the counterions (Na^+ ions) for systems with different σ.

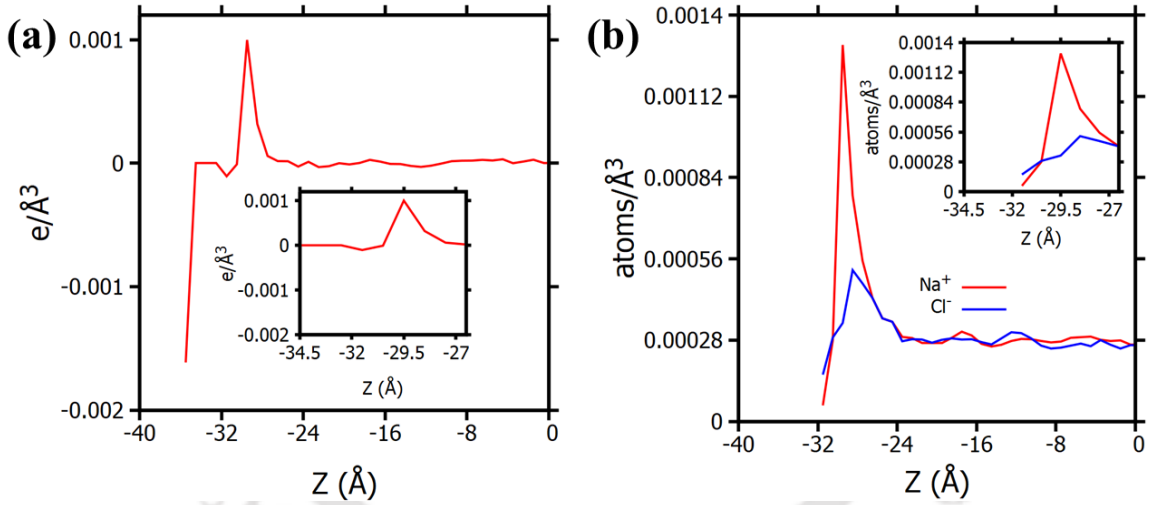

Figure 7-8: Charge density and corresponding ion density profile for $P_{0.025}$ system. (a) Charge density profile. (b) Ion density profile.

$-X$ direction) towards the extreme right (i.e. extreme end of the nanochannel along the $+X$ direction), then a water permeation event is counted. Figure 7-3(a) shows the water permeation events per nanosecond through the nanochannel for different σ. The water permeation events through the nanochannel increases as σ increases from 0.005 C/m^{-2} to 0.025 C/m^{-2}. However, with the further increase in σ beyond 0.025 C/m^{-2}, the water permeation events through the nanochannel decreases.

To get an insight into the relation between water permeation events and σ, we

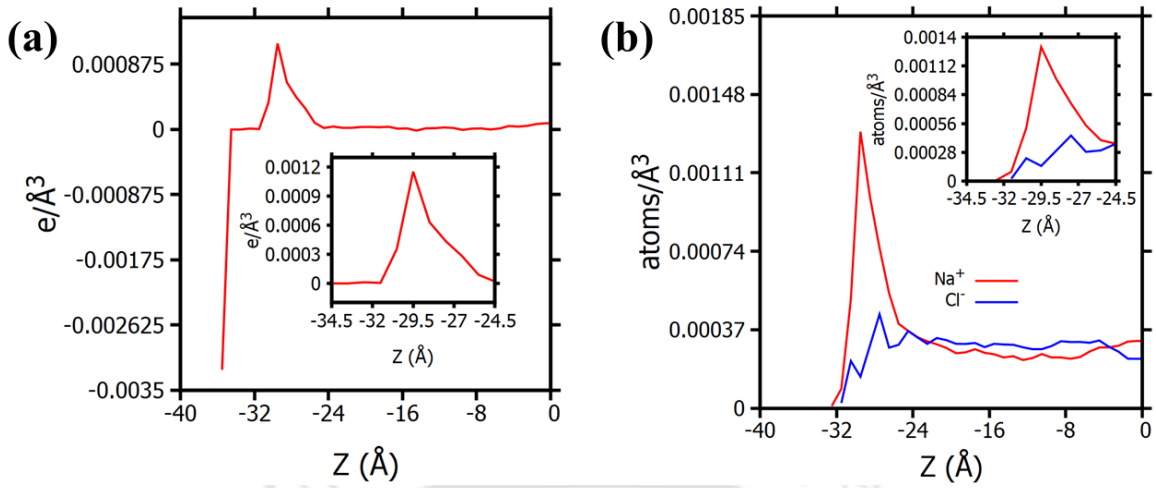

Figure 7-9: Charge density and corresponding ion density profile for $P_{0.05}$ system. (a) Charge density profile. (b) Ion density profile.

computed the number distribution of the velocities of the water molecules permeating through the nanochannel. All the velocities reported in this present study are along the direction of applied electric field. So, with reference to Figure 7-2, the velocities reported in this present study are along the $+X$ direction. Figure 7-3(b) shows the distribution of the velocities of the water molecules permeating through the nanochannel for different σ. Here $\boldsymbol{N_w}$ is the number of water molecules permeating through the nanochannel. As can be seen from Figure 7-3(b), the velocity of the water molecules increases as the σ increases from 0.005 Cm^{-2} to 0.025 Cm^{-2}. Because of the increase in water velocity inside the nanochannel, water permeation events through the nanochannel also increases as the σ increases from 0.005 Cm^{-2} to 0.025 Cm^{-2} (Figure 7-3(a)). With further increase in σ beyond 0.025 Cm^{-2}, the velocity of the water molecules inside the nanochannel gradually decreases. Consequently, the water permeation events through the nanochannel also decreases with the increase in σ beyond 0.025 Cm^{-2} as observed in Figure 7-3(a).

Figure 7-4 shows the charge distribution along the Z direction for nanochannel with different σ. As the simulation setup is symmetric about the axis $Z = 0$, only the lower portion from the symmetric line in depicted in Figure 7-4. The first peak of the charge distribution is considered as the position of the stern layer. The height of this peak increases with the increase in σ. In other words the charge intensity of the

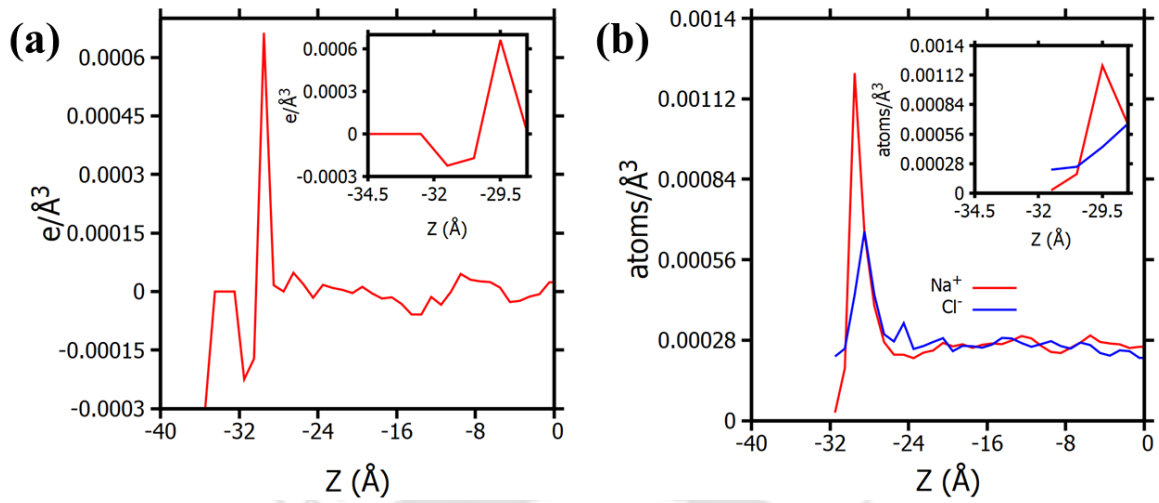

Figure 7-10: Charge density and corresponding ion density profile for $P_{0.005}$ system. (a) Charge density profile. (b) Ion density profile.

stern layer increases with the increase in σ. The distance (along the Z direction) of the stern layer from the wall is also dependent on the σ. The position of the wall of the rectangular nanochannel is +35.5 Å at the top and −35.5 Å at the bottom. For $P_{0.2}$, the position of the stern layer is +32.5 Å at the top and −32.5 Å at the bottom. On the other hand, for $P_{0.1}$, the position of the stern layer is +30.5 Å at the top and −30.5 Å at the bottom. For $P_{0.05}$, $P_{0.025}$, $P_{0.01}$ and $P_{0.005}$, the position of the stern layer is +29.5 Å at the top and −29.5 Å at the bottom. So, for $P_{0.2}$, the distance of the stern layer from the wall is 3 Å, for $P_{0.1}$, the distance of the stern layer from the wall is 5 Å, and for all other remaining systems ($P_{0.005}$, $P_{0.01}$, $P_{0.025}$ and $P_{0.05}$) the the distance of the stern layer from the wall is 6 Å.

The distance from the stern layer (the peak of the charge distribution) to the charge neutral position of the charge density profile along the Z direction is considered as the thickness of the diffuse layer. The thickness of the diffuse layer for the systems with different σ is tabulated in Table 7.2. As can be seen from Table 7.2, as the σ increases from 0.005 Cm^{-2} to 0.1 Cm^{-2}, the thickness of the diffuse layer gradually increases. However, at a very high value of σ (at 0.2 Cm^{-2}), the thickness of the diffuse layer sharply decreases. For $\sigma <= 0.025\ Cm^{-2}$, a drop in the charge density profile before the stern layer is observed which will be discussed in detail later in this section.

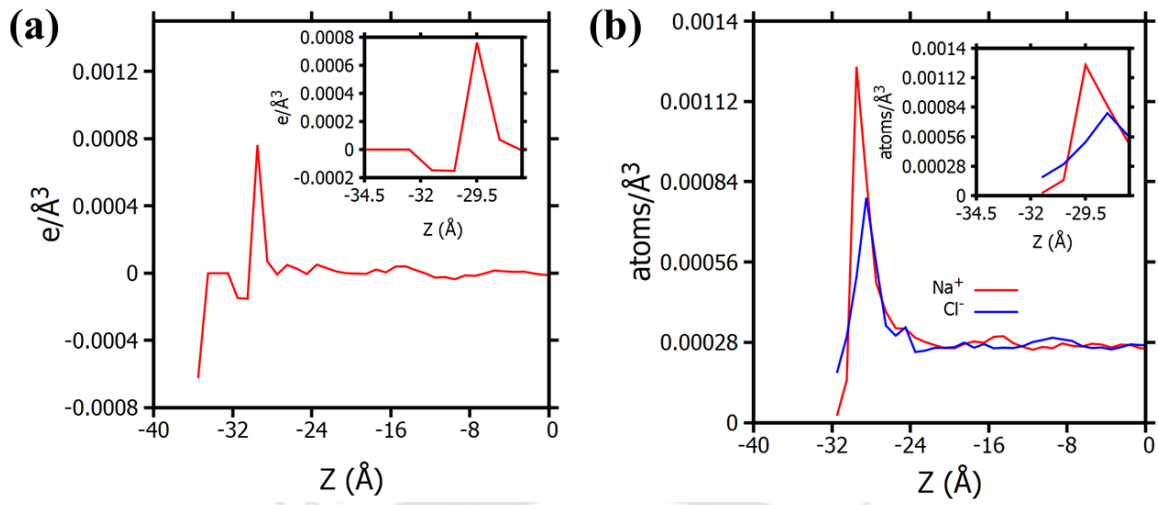

Figure 7-11: Charge density and corresponding ion density profile for $P_{0.01}$ system. (a) Charge density profile. (b) Ion density profile.

Table 7.2: Thickness of the diffuse layer and distance of the stern layer from the wall for systems with different σ

System	Thickness of the diffuse layer (Å)	Distance of the stern layer from the wall Å
$P_{0.005}$	1	6
$P_{0.01}$	2	6
$P_{0.025}$	3	6
$P_{0.05}$	5	6
$P_{0.1}$	6	5
$P_{0.2}$	1	3

Figure 7-5, shows the interaction energy between the graphene surface and the Na^+ ions. As can be seen from Figure 7-5(a), with the increase in σ the electrostatic interaction (ELE) between the wall and the Na^+ ions gradually increases. In the present study a negative interaction energy refers to an attractive interaction and a positive interaction energy refers to an repulsive interaction. The van der Waals (vdW) interaction between the wall and the Na^+ ions is shown in Figure 7-5(b). For $P_{0.2}$, the vdW interaction is repulsive in nature and for $P_{0.1}$, the vdW interaction slightly fluctuate between positive and negative vales around 0. For the remaining systems ($P_{0.005}$, $P_{0.01}$, $P_{0.025}$ and $P_{0.05}$) the vdW interactions are almost same and

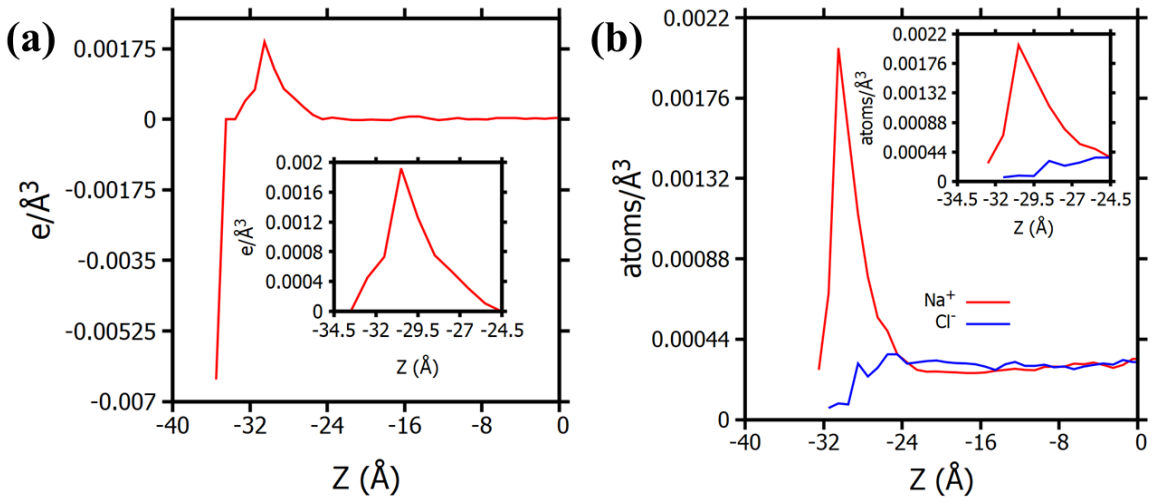

Figure 7-12: Charge density and corresponding ion density profile for $P_{0.1}$ system. (a) Charge density profile. (b) Ion density profile.

attractive in nature. Figure 7-5(c) shows the overall or total interaction energy (overall interaction or total interaction is the summation of electrostatic interaction and the vdW interaction) between the wall and Na^+ ions and it is observed that the overall interaction between the wall and the Na^+ ions is dictated by the electrostatic interactions.

The interactions between the wall and the water molecules are shown in Figure 7-6. For water, both electrostatic interactions (Figure 7-6(a)) and the van der Waals interactions (Figure 7-6(b)) are attractive in nature. With the increase in σ the electrostatic interactions between the wall and the water molecules gradually increases as observed in Figure 7-6(a). For the systems with σ equal to 0.005 Cm^{-2} and 0.01 Cm^{-2} the vdW interaction is almost same (Figure 7-6(b)). However, with further increase in σ, the vdW interaction between the wall and the water molecules gradually decreases. Figure 7-6(c), shows the overall interaction between the wall and the water molecules. The overall interaction between the wall the water molecules is attractive in nature and it increases with the increase in σ. For, $\sigma <= 0.025\ Cm^{-2}$, the overall interaction between the wall and the water molecules is dominated by the vdW interactions. However, for systems with $\sigma >= 0.05\ Cm^{-2}$, the overall interaction between the wall and the water molecules is dominated by the electrostatic interaction.

In an electro-osmotic transport, the electro-osmotic velocity is the result of the

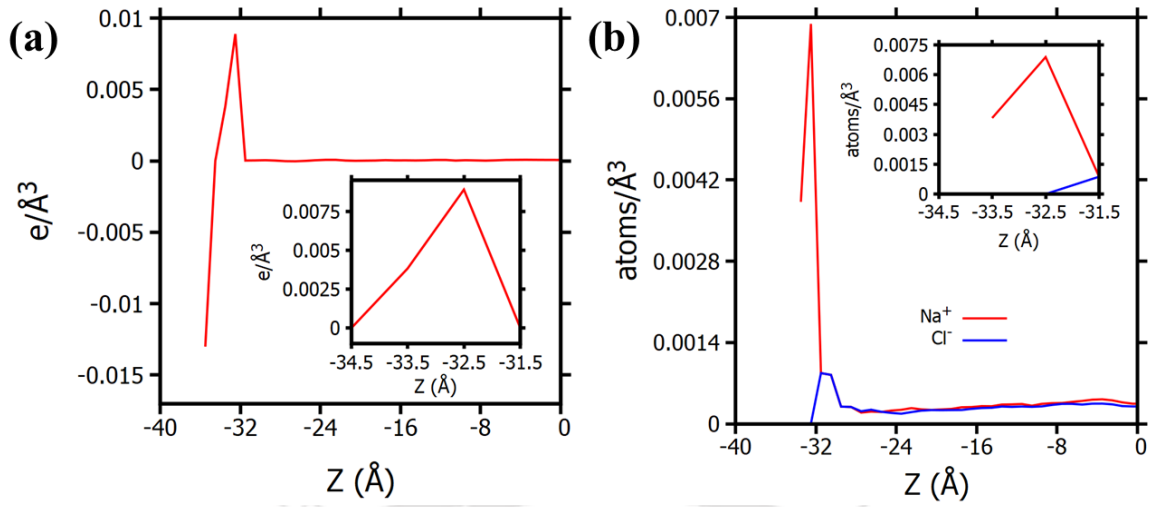

Figure 7-13: Charge density and corresponding ion density profile for $P_{0.2}$ system. (a) Charge density profile. (b) Ion density profile.

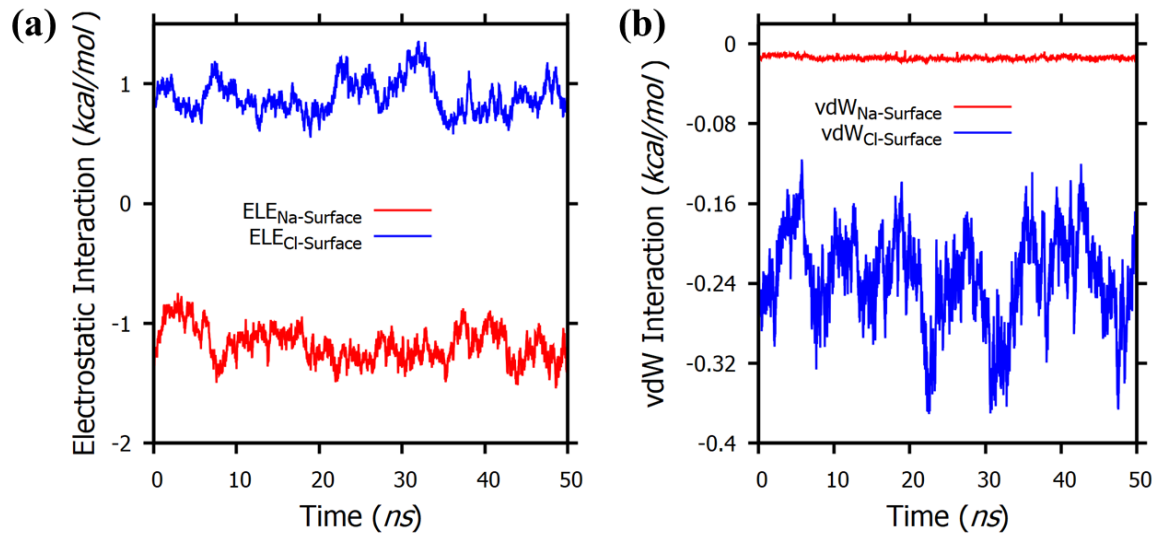

Figure 7-14: Interaction of Na^+ and Cl^- ions with the wall for $P_{0.025}$ system. (a) Electrostatic interaction. (b) van der Waals interaction.

motion of the counterions (Na^+ ions in this present study). A system with thicker diffuse layer can accommodate more number of counterions and has a greater potential to generate higher electro-osmotic velocity. However, on the same note, the interactions between the wall and the counterions/water are also crucial in determining the electro-osmotic velocity. A higher interactions (attractive interactions) between the wall and the counterions/water leads to more restriction on the movement of the species, which leads to reduction in the electro-osmotic velocity. As the σ increases

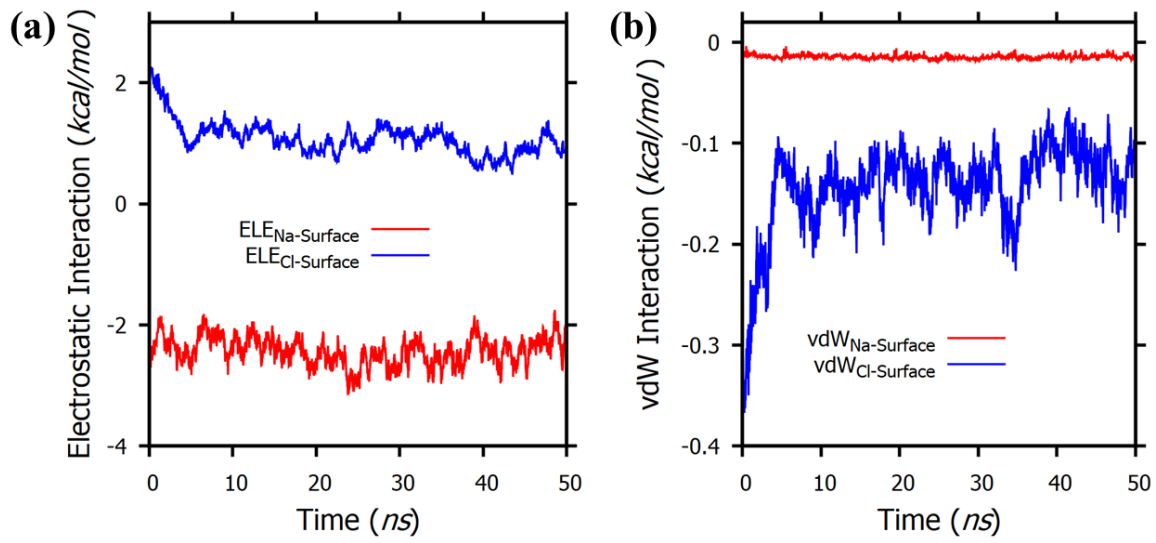

Figure 7-15: Interaction of Na^+ and Cl^- ions with the wall for $P_{0.05}$ system. (a) Electrostatic interaction. (b) van der Waals interaction.

from 0.005 Cm^{-2} to 0.025 Cm^{-2}, the velocity of the Na^+ ions increases and beyond 0.025 cm^{-2}, with the further increase in σ, the velocity of the Na^+ ions gradually decreases as observed in Figure 7-7. Here, $\boldsymbol{N_{Na}}$ is the number of Na^+ ions permeating through the nanochannel from the extreme left to the extreme right through the nanochannel. This observation is in accordance with the observation reported in Figure 7-3(b). As the σ increases from 0.005 Cm^{-2} to 0.025 Cm^{-2}, the thickness of the diffuse layer increases (Figure 7-4 and Table 7.2). This leads to increase in velocity of the Na^+ ions (Figure 7-7), which in turn increases the velocity of the water molecules(Figure 7-3(b)). As a consequence, water permeation events through the nanochannel also increases accordingly (Figure 7-3(a)). As σ increases beyond 0.025 Cm^{-2}, the interaction between the wall and the Na^+ ion/water increases significantly as observed in Figure 7-5 and Figure 7-6 respectively. Because of this, the velocity of the Na^+ ions and water molecules reduces gradually as σ increases beyond 0.025 Cm^{-2} as depicted in Figure 7-7 and Figure 7-3(b) respectively. This leads to lower water permeation events through the nanochannel as σ increases beyond 0.025 Cm^{-2} (Figure 7-3(a)).

In the charge density profile reported in Figure 7-4, a drop in the density profile before the stern layer is observed for $\sigma <= 0.025\ Cm^{-2}$. Figures 7-8(a) and 7-8(b)

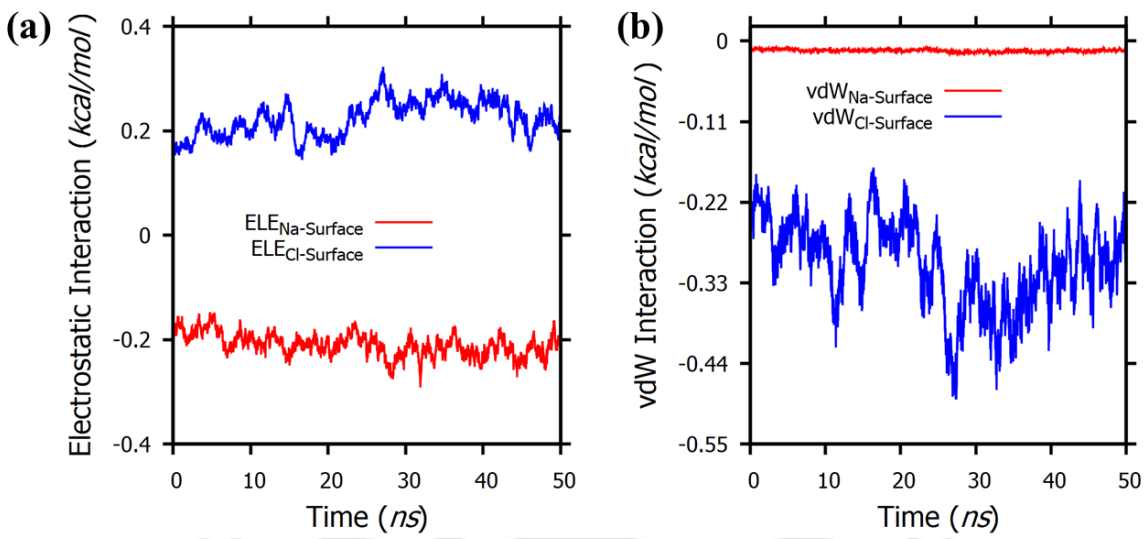

Figure 7-16: Interaction of Na^+ and Cl^- ions with the wall for $P_{0.005}$ system. (a) Electrostatic interaction. (b) van der Waals interaction.

show the charge and ion density profile for $P_{0.025}$ system. For this system, the peaks in the charge density profile and Na^+ ion density profiles are observed at $\pm$ 29.5 Å which correspond to the position of the stern layers. At around $\pm$ 26.5 Å, the density of Na^+ and Cl^+ ions become almost equal and the net charge become zero which signifies the end position of the diffuse layer. So, the thickness of the diffuse layer is 3 Å (29.5 – 26.5 Å) as reported in Table 7.2. The two extreme points at the ends of the charge density profile (Figure 7-8) are the positions of the wall which are located at $\pm$ 35.5 Å. The value of the charge density at these two extreme points is -0.001614 e/Å^3. After these two extreme ends, there is a vacant space from $\pm$ 34.5 Å to $\pm$ 32.5 Å without any water molecules or ion species. In the charge density profile, this region is the charge neutral region just after the wall as observed in Figure 7-8(a). After this charge neutral region, a drop in the charge density profile (i.e. negative charge density) is observed. In this region ($\pm$ 31.5 Å to $\pm$ 30.5 Å), the number density of Cl^- ion is greater than the number density of Na^+ ion as reported in Figure 7-8(b). As a consequence, in this region, the charge density is negative in nature. After this region, the peak in the Na^+ ion density profile is observed at $\pm$ 29.5 Å (Figure 7-8(b)) which is also the position of the peak of the charge density profile (Figure 7-8(a)) i.e. the stern layer. After the diffuse layer (i.e. after $\pm$ 26.5 Å) towards the bulk, the charge

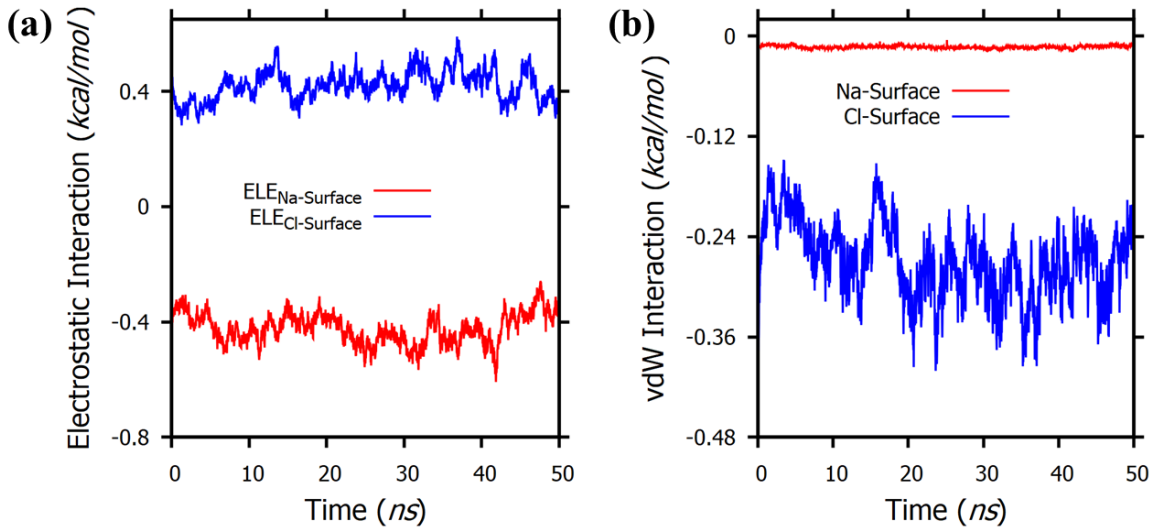

Figure 7-17: Interaction of Na^+ and Cl^- ions with the wall for $P_{0.01}$ system. (a) Electrostatic interaction. (b) van der Waals interaction.

density is neutral although little fluctuations are observed due to small fluctuations in the number density of the ion species.

Figures 7-9(a) and 7-9(b) show the charge density and ion density profiles respectively for $P_{0.05}$ system. As observed in Figure 7-9(a), this system (and all other system with $\sigma >= 0.05$) does not have the negative charge density region before the stern layer. Here also, the two extreme ends in the charge density profile are the positions of the wall which are located at $\pm$ 35.5 Å. The value of the charge density at the walls is -0.003228 e/Å^3. Just after the wall, there is a vacant space from $\pm$ 34.5 Å to $\pm$ 33.5 Å, which appear as a charge neutral region in the charge density profile (Figure 7-9(a)). However, this vacant space is smaller as compared to $P_{0.025}$ system. The squeezing of this vacant space occurs due to the strong electrostatic interactions between the walls and the counterions (i.e. Na^+ ions). Also owing to this strong electrostatic interactions between the counterions and the wall, the density of the counterions (i.e Na^+ ions) is greater than the co-ions (i.e. Cl^- ions) just after the wall (and before the stern layer) as observed in Figure 7-9(b). Consequently, the negative region in the charge density profile (before the stern layer) is not observed for system with $\sigma >= 0.025\ Cm^{-2}$. The charge density and ion density profile for the remaining systems ($P_{0.005}$, $P_{0.01}$, $P_{0.1}$ and $P_{0.2}$) are reported in Figure 7-10, 7-11,

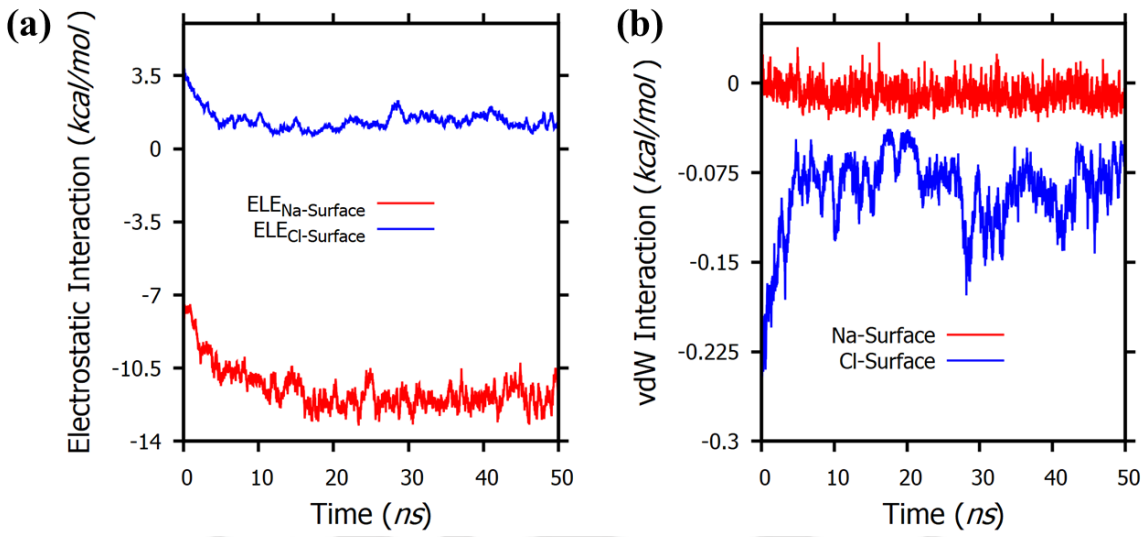

Figure 7-18: Interaction of Na^+ and Cl^- ions with the wall for $P_{0.1}$ system. (a) Electrostatic interaction. (b) van der Waals interaction.

7-12 and 7-13 respectively.

Figures 7-14(a) and 7-14(b) show the electrostatic and vdW interaction of the ion species (Na^+ and Cl^- ions) with the wall respectively for $P_{0.025}$ system. The electrostatic interaction between Na^+ ions and the wall is negative which signifies attractive interaction while the electrostatic interaction between the Cl^- ions and the wall is positive which signifies repulsive interaction as observed in Figure 7-14(a). The vdW interaction of both the ionic species with the wall is attractive in nature as can be seen from Figure 7-14(b). However, the vdW interaction of the Cl^- ions with the wall is stronger as compared to Na^+ ions. Because of this stronger vdW interaction, the density of the Cl^- ions near the wall is more as compared to Na^+ ions as vdW interaction is a short range interaction. Consequently, a drop in the charge density profile is observed before the stern layer near the wall for systems with $\sigma <= 0.025$ Cm^{-2} (Figure 7-4 and 7-8).

Figures 7-15(a) and 7-15(b) show the electrostatic and vdW interaction of the ion species with the wall respectively for $P_{0.05}$ system. For this system also the vdW interaction of the Cl^- ions with the wall is greater than the vdW interaction of the Na^+ ions with the wall as shown in Figure 7-15(b). However, this difference in vdW interaction is less as compared to the difference in $P_{0.025}$ system. Along with this, the

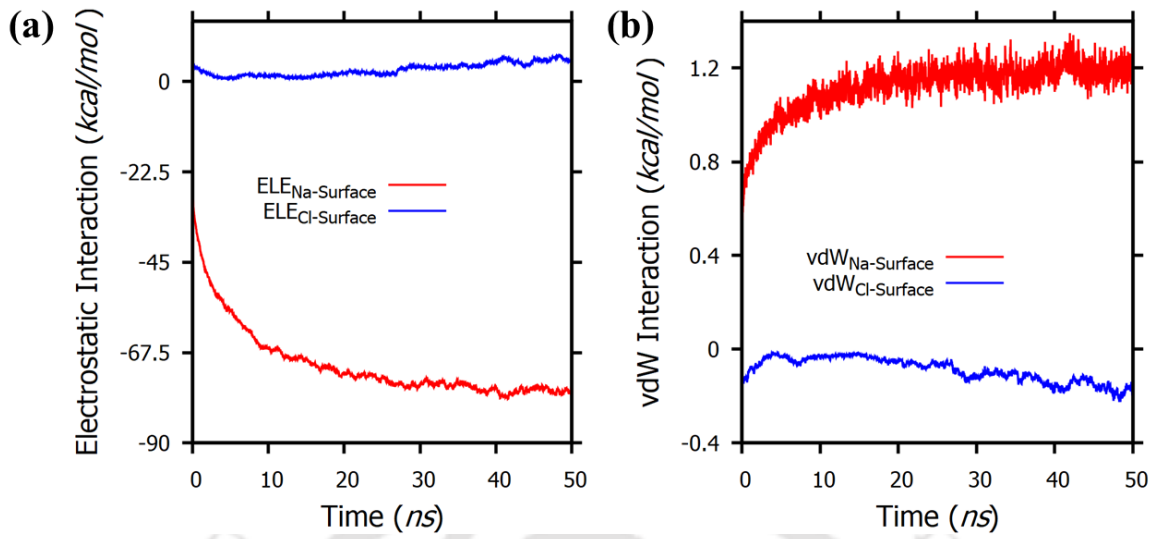

Figure 7-19: Interaction of Na^+ and Cl^- ions with the wall for $P_{0.2}$ system. (a) Electrostatic interaction. (b) van der Waals interaction.

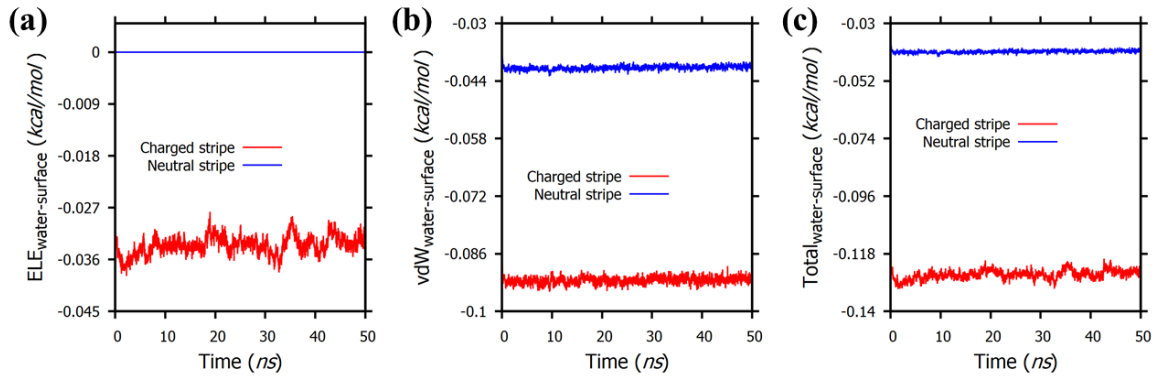

Figure 7-20: Interaction between water molecules and charged striped and neutral striped portion of the wall for $P_{0.025}$ system. (a) Electrostatic interaction. (b) vdW interaction. (c) Total interaction.

increase in electrostatic interactions between the wall and the ionic species results in higher Na^+ ion density near the wall as compared to Cl^- ions for the systems with $\sigma >= 0.05\ Cm^{-2}$. Because of this, the drop in the charge density profile before the stern layer is not observed for systems with $\sigma >= 0.5\ Cm^{-2}$ as can be seen in Figure 7-4 and 7-9. The comparison of the interactions of the ionic species with the wall for the remaining systems ($P_{0.005}$, $P_{0.01}$, $P_{0.1}$ and $P_{0.2}$) are reported in Figure 7-16, 7-17, 7-18 and 7-19 respectively.

Figures 7-20 and 7-21 show the interaction between the water molecules and the

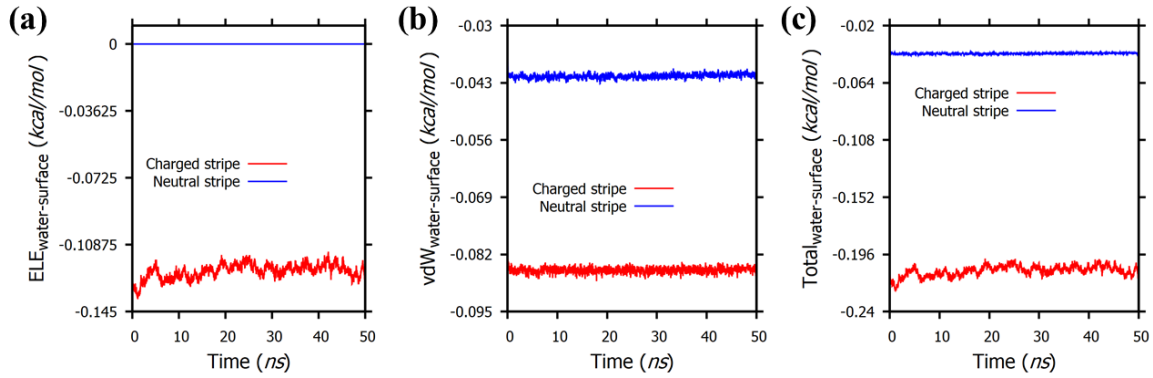

Figure 7-21: Interaction between water molecules and charged striped and neutral striped portion of the wall for $P_{0.05}$ system. (a) Electrostatic interaction. (b) vdW interaction. (c) Total interaction.

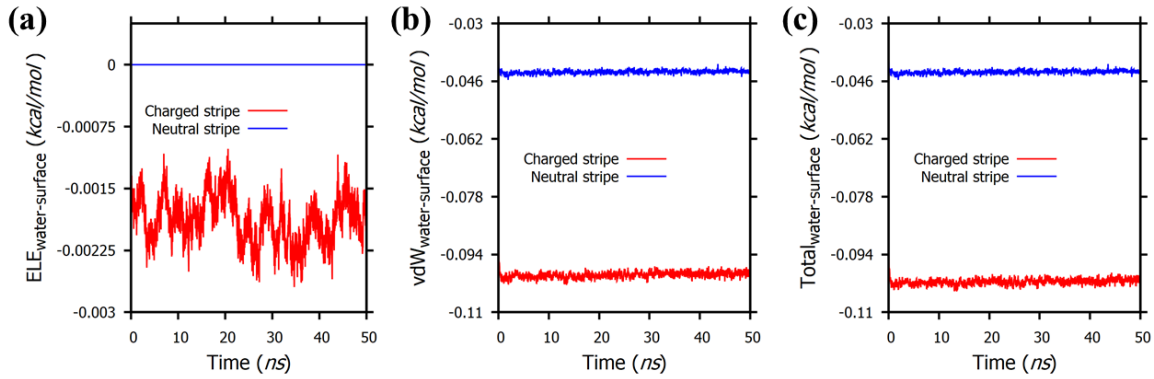

Figure 7-22: Interaction between water molecules and charged striped and neutral striped portion of the wall for $P_{0.005}$ system. (a) Electrostatic interaction. (b) vdW interaction. (c) Total interaction.

charged and neutral striped portion of the wall for $P_{0.025}$ and $P_{0.05}$ system respectively. There is no electrostatic interactions between the neutral striped potion of the wall and the water molecules. The charged striped portion of the wall has stronger interactions with the water molecules as compared to the neutral striped one. The interactions between the water molecules and the charged/neutral striped portions of the wall for $P_{0.005}$, $P_{0.01}$, $P_{0.1}$ and $P_{0.2}$ systems are reported in Figure 7-22, 7-23, 7-24 and 7-25 respectively. For system with $\sigma <= 0.025\ Cm^{-2}$, the overall interactions (or total interactions) between the charged stripe and the water molecules are dominated by the vdW interactions. On the other hand for systems with $\sigma >= 0.05$ Cm^{-2} the overall interactions between the charged stripe and the water molecules

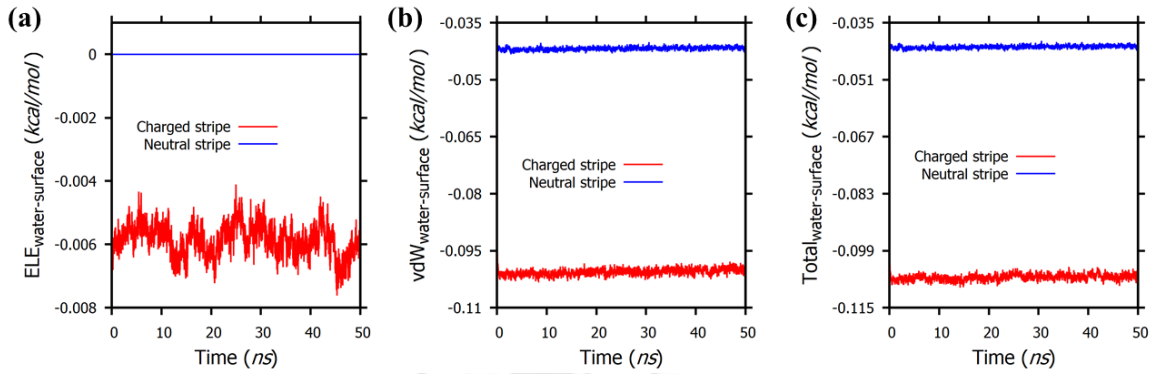

Figure 7-23: Interaction between water molecules and charged striped and neutral striped portion of the wall for $P_{0.01}$ system. (a) Electrostatic interaction. (b) vdW interaction. (c) Total interaction.

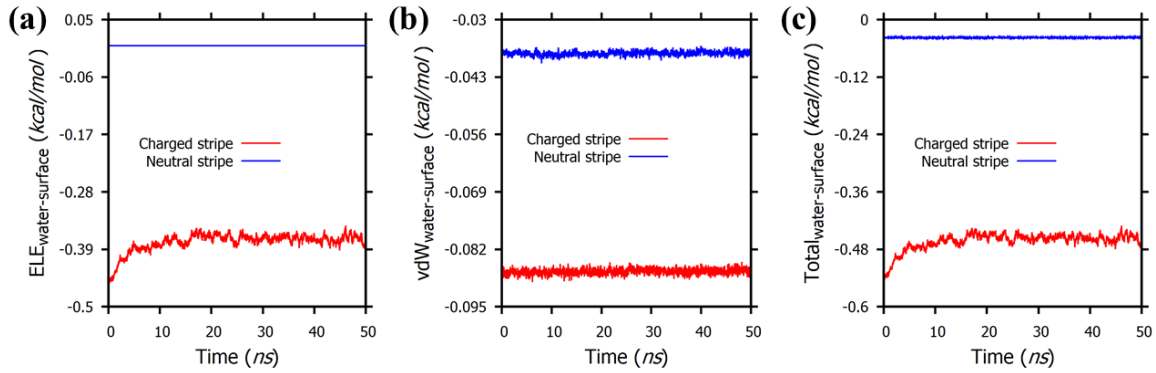

Figure 7-24: Interaction between water molecules and charged striped and neutral striped portion of the wall for $P_{0.1}$ system. (a) Electrostatic interaction. (b) vdW interaction. (c) Total interaction.

are dominated by the electrostatic interactions.

We have also computed the velocity profiles of water. The electro-osmotic velocity profiles along the Z direction (perpendicular to the flow) is calculated using the binning method where the flow domain in divided into large number of bins stacked one over another along the Z direction. The spatial velocity distribution (along Z direction) thus obtained is then curve fitted with polynomial curve fitting approach. The velocity at 3 Å from the wall is considered as the slip velocity. Fig. 7-26 shows the velocity profiles of water for systems with different σ. As σ increases from 0.005 C/m^2 to 0.025 C/m^2, the difference in the slip velocity between the charged and neutral striped portion of the wall increase where the slip velocity in the charged

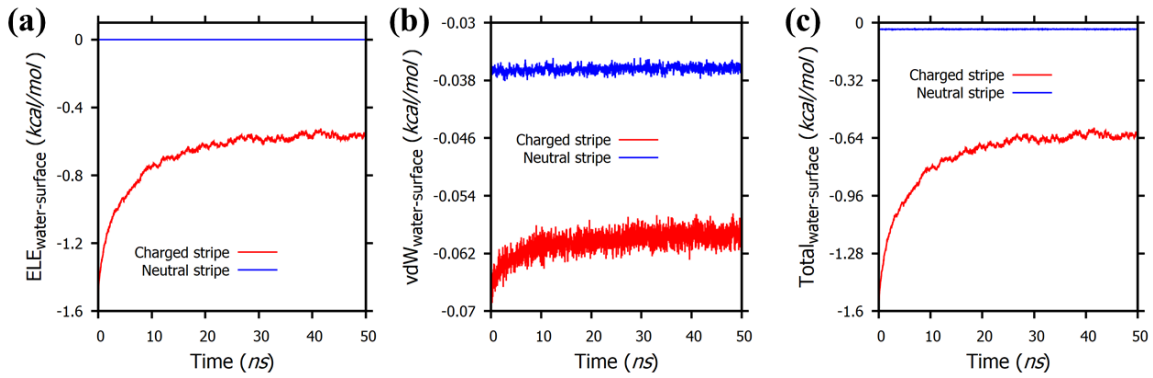

Figure 7-25: Interaction between water molecules and charged striped and neutral striped portion of the wall for $P_{0.2}$ system. (a) Electrostatic interaction. (b) vdW interaction. (c) Total interaction.

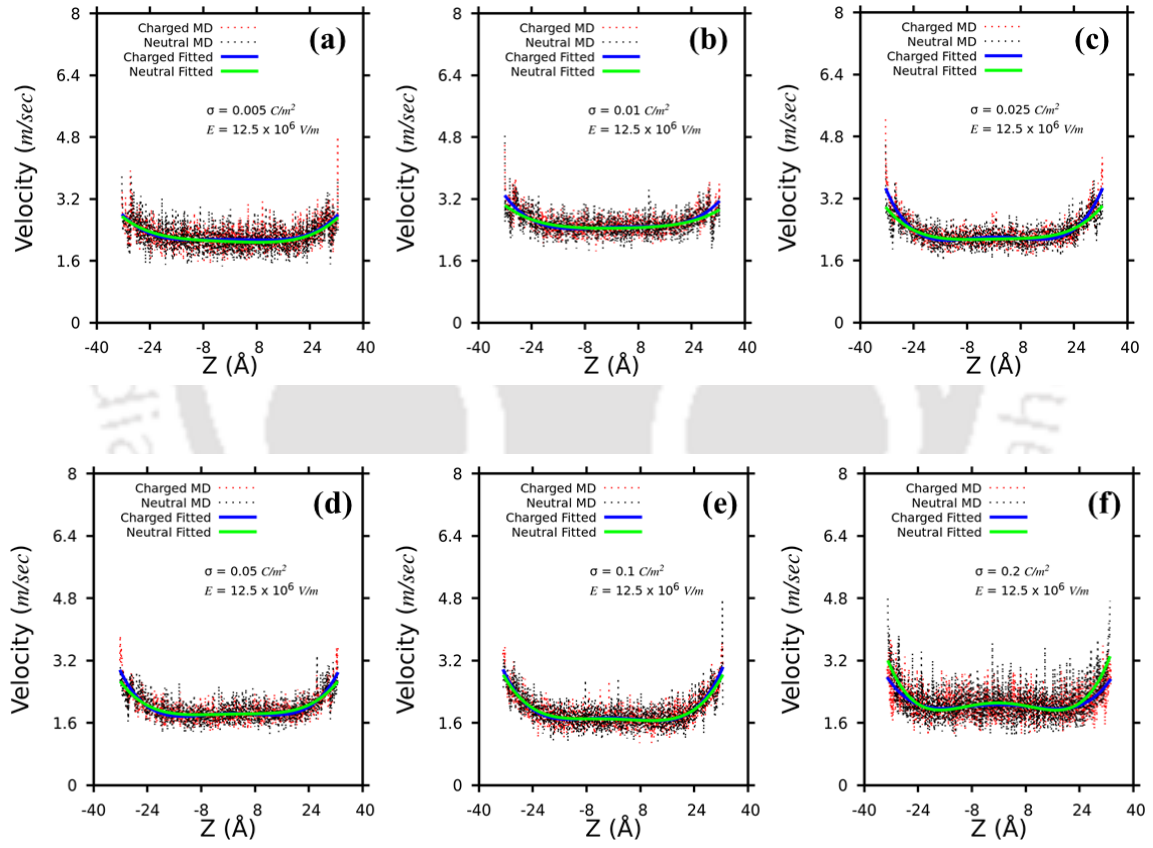

Figure 7-26: Water velocity profile along Z direction. (a) $\sigma = 0.005\ C/m^2$. (b) $\sigma = 0.01\ C/m^2$. (c) $\sigma = 0.025\ C/m^2$. (d) $\sigma = 0.05\ C/m^2$. (e) $\sigma = 0.1\ C/m^2$. (f) $\sigma = 0.2\ C/m^2$.

stripe portion is higher than the neutral one. This difference is maximum for 0.025 C/m^2. After that as σ increases to 0.05 C/m^2, the difference in the slip velocity

between charged and neutral stripe portion of the wall reduces. With $\sigma = 0.1\ C/m^2$, this difference further reduces and at $\sigma = 0.2\ C/m^2$, the slip velocity in the neutral striped portion of the wall is higher than the charged stripe portion. This observation is interesting, considering the similar trend which is observed for number of water permeation events and electro-osmotic velocity. This signifies the importance of slip velocity in nanochannel electro-osmotic flow.

7.4 Conclusions

In this present study the electro-osmotic flow behaviour through nanochannel with patterned surface charge distribution is studied using non-equilibrium MD simulations. The electro-osmotic velocity and the water permeance through the nanochannel increases as the surface charge density increases from 0.005 Cm^{-2} to 0.025 Cm^{-2}. This is primarily due to the increase in thickness of the diffuse layer. As the surface charge density increases beyond 0.025 Cm^{-2}, the electro-osmotic velocity and the water permeance through the nanochannel decreases due to strong interactions between the wall and the counterions/water molecules. With the increase in surface charge density, the charge intensity of the stern layer increases. However, at a very high value of surface charge density (0.1 Cm^{-2} and 0.2 Cm^{-2}) the stern layer becomes closer to the surface of the nanochannel. Near the wall of the nanochannel and before the stern layer, a drop in the charge density profile is observed for lower values of surface charge density ($\sigma <= 0.025\ Cm^{-2}$). This is because of stronger vdW interactions of the Cl^- ions with the wall as compared to the vdW interactions between Na^+ ions and the wall. However, at a higher value of surface charge density ($\sigma >= 0.05\ Cm^{-2}$) this drop in the charge density profile diminishes due to strong electrostatic interactions between Na^+ ions and the wall. The interactions between the water molecules and the charged striped portion of the wall is stronger as compared to the interactions between the water molecules and the neutral striped portion of the wall. At a lower value of surface charge density ($\sigma <= 0.025\ Cm^{-2}$), the interaction between the water molecules and the charged striped portion of the

wall is dictated by the vdW interaction whereas at a higher value of surface charge density ($\sigma >= 0.05\ Cm^{-2}$), this interaction is dominated by the electrostatic interaction. We believe that the observations reported in this present study will be helpful to the future investigations on various potential applicability of electro-osmotic flow and would aid in the experimental investigations on the same.

Chapter 8

Conclusions and Future Scope

8.1 Conclusions

From the non-equilibrium MD simulations performed in this PhD dissertation study, following conclusions are made:

- In a layered GO membrane, the geometric parameters like pore offset distance (**W**) and interlayer distance (**H**) significantly influence the performance of the membrane. In a layered GO membrane, the parameter **W** is a measure of the size of the constituting GO nanosheets of the membrane. A higher value of **W** signifies layered GO membrane composed of GO nanosheets of larger lateral dimensions. With the increase in the parameter **W**, the water permeance through the membrane decreases while the salt rejection increases. In other words, as the size of the constituting GO nanosheets increases, the water permeance through layered GO membrane decreases while the salt rejection increases. This is because of the increase in permeation pathways through layered GO membranes as the size of the constituting GO nanosheets increases (or **W** increases). As the size of the constituting GO nanosheets increases, the water molecules and the other species have to traverse a "zig zag" pathway through the layered GO membrane, which in turn decreases the water permeance through the membrane and increases the salt rejection. Apart from this, the increase in **W** (or the size of the

constituting GO nanosheets) also leads to the blockage of the pathways of the permeate through the layered GO membrane due to the movement of the GO nanosheets. This severely affects the performance of the layered GO membrane during the FO process. On the other hand, the variation water permeance and salt rejection with **H** is not unidirectional in nature. As **H** increases from 8.0 Å to 12.0 Å, the water permeance increases and salt rejection decreases. However, beyond 12.0 Å, with further increase in **H**, the water permeance through layered GO membrane decreases and salt rejection increases. Here factors like water permeation distance through the membrane and the diffusivity of water and other ionic species inside the membrane play a vital role in determining the performance of the membrane. The diffusivity of the species (water and ions) increases with the increase in **H**, which in turn increases the permeance of the species through the membrane. On the other hand, permeation distance through the membrane increases with the increase in **H** which leads to decrease in permeance of the species. As **H** increases from 8.0 Å to 12.0 Å, the increase in diffusivity dominates the permeance rate of the species. Because of this water permeance increases and salt rejection decreases as **H** increases from 8.0 Å to 12.0 Å. On the other hand, the permeance characteristics of the species through layered GO membrane is dominated by the increase in permeation distance as **H** increases from 12.0 Å to 18.0 Å. Because of this, water permeance decreases and salt rejection increases as **H** increases from 12.0 Å to 18.0 Å. With the appropriate tuning of the sizes of the GO nanosheets and interlayer spacings layered GO membrane can be a suitable candidate for sea water desalination, dehydration of acetic acid and various separation/purification applications through FO process. The performance of layered GO membrane is also dependent on the various functional groups located on GO nanosheets. Inside the layered GO membrane near the edges, the number of water molecules in the hydration shell of the permeating water molecules and ion species are less as compared to their values near the basal plane of the GO nanosheets. This is primarily due to the strong interaction between the water molecules and the carboxylic functional

groups located at the edges of the GO nanosheets.

- The presence of cations can also influence the performance of a membrane. In the presence of the cations, water molecules are more compactly arranged inside the interlayer gallery of layered GO membrane. Cation intercalation also increases the stability of hydrogen bond network among the water molecules inside the interlayer gallery of layered GO membrane. This is because of the slow reorientability of the water molecules inside the interlayer gallery in the presence of the cations. The synergistic effect of these changes is that the water flux through cation intercalated layered GO membrane is higher as compared to the corresponding pristine layered GO membrane. The pristine layered GO membrane has higher rejection towards Cl^- ions as compared to Na^+ ions. However, this is exactly opposite for cation intercalated layered GO membrane. This can be attributed to the distinct electrostatic interaction between the cations present inside the interlayer gallery and the invading ion species.

- Fluid flow through a graphene nanochannel can also be controlled by varying the surface charge density in an electro-osmotic flow. The electro-osmotic velocity and the water permeance through the nanochannel increases as the surface charge density increases from 0.005 Cm^{-2} to 0.025 Cm^{-2}. This is primarily because of the increase in thickness of the diffuse layer. With the further increase in surface charge density beyond 0.025 Cm^{-2}, the electro-osmotic velocity and the water permeance through the nanochannel gradually decreases. This is because of the significant increase in the interaction strength between the wall of the nanochannel and the counterions/water molecules. The charge intensity of the stern layer increases with the increase in surface charge density. At a very high value of surface charge density (0.1 Cm^{-2} and 0.2 Cm^{-2}), the position of the stern layer becomes closer to the wall of the nanochannel. For lower values of surface charge density ($\sigma <= 0.025\ Cm^{-2}$) there is a drop in the charge density profile close to the wall and just before the stern layer. This is because of the fact that the Cl^- ions have stronger van der Waals interaction with the graphene

surface as compared to the van der Waals interaction between Na^+ ions and the graphene surface. At a higher value of surface charge density ($\sigma >= 0.05\ Cm^{-2}$) this drop in the charge density profile is not observed due to strong electrostatic interactions between Na^+ ions and the wall. The slip velocity in the charged striped portion of the wall is higher than the neutral striped portion except at a very high value of surface charge density of 0.2 Cm^{-2}. For lower values of surface charge densities ($\sigma <= 0.025\ Cm^{-2}$), the interaction between the water molecules and the charged striped portion of the graphene wall is dominated by the van der Waals interaction whereas for higher values of surface charge density ($\sigma >= 0.05\ Cm^{-2}$), this interaction is dominated by the electrostatic interaction.

8.2 Scope for Future Investigations

In continuation to the study and observations reported in the present study following points would be interesting to investigate in the future:

- In an FO process, in addition to the membrane material, the facile regeneration of draw solution is also important. So, in the future one can explore the possibilities of using GO with different draw solutions and also its anti-fouling behaviour in difficult feed environment. Similarly, the feed solution considered in the study of acetic acid dehydration (in Chapter 5) is a 20.0 $wt.\%$ aqueous acetic acid solution. However, for many industrial applications the concentration of acetic acid to be dehydrated are much higher. So, it would be interesting to investigate the performance of layered GO membrane for dehydration of those concentrated acetic acid solutions using FO process provided suitable draw solutions with very high osmotic pressure are available.

- As reported in Chapter 6, the presence of cations inside the interlayer gallery can significantly influence the performance of layered GO membrane. In future one may consider to investigate the performance of the membrane by varying

the amount of cations intercalated inside the interlayer gallery of layered GO membrane.

- GO sheets parted away from GO membrane in applications may have harmful affects on the aqueous environment. So the stability of GO membrane is aqueous environment is very crucial. Some recent works pointed out the hazardous impact of the GO as nano-material on environment and human health [359, 396]. The toxic effect of GO dependent on many factors like, the sizes of the GO sheets [397], its degree of oxidation [398], the amount of exposure to the living cells ([399] etc. So, along with the potential applicability of layered GO membrane for various separation and purification applications, its environmental impact also needs critical investigations.

We are hopeful that the observations reported in this present study would be helpful to the future investigations on graphene and graphene based materials for various applications ranging from water purification and sea water desalination to various micro and nanoscale devices.

भारतीय प्रौद्योगिकी संस्थान गुवाहाटी
Indian Institute of Technology Guwahati

Bibliography

[1] F. Perrozzi, S. Prezioso, and L Ottaviano. Graphene oxide: from fundamentals to applications. *J. Phys.: Condens. Matter*, 27:1–21, 2015.

[2] R. M. Garud, S. V. Kore, V. S. Kore, and G. S. Kulkarni. A short review on process and applications of reverse osmosis. *Univers. j. environ. res. technol.*, 1(3):233–238, 2011.

[3] I. L. Alsvik and M. B. Hägg. Pressure retarded osmosis and forward osmosis membranes: Materials and methods. *Polymers*, 5:303–327, 2013.

[4] E. R. Hernández. Molecular dynamics: from basic techniques to applications (a molecular dynamics primer). *AIP Conf. Proc.*, 1077(1):95–123, 2008.

[5] H. Tang, D. Liu, Y. Zhao, X. Yang, J. Lu, and F. Cui. Molecular dynamics study of the aggregation process of graphene oxide in water. *J. Phys. Chem. C*, 119(47):26712–26718, 2015.

[6] R. W. Baker. *Membrane Technology and Applications, 2nd ed.* John Wiley & Sons, Ltd., Chichester, 2004.

[7] S. P. Nunes and K. V. Peinemann. *Membrane Technology: in the Chemical Industry.* Wiley-VCH, Weinheim, 2001.

[8] M. M. Pendergast and E. M.V. Hoek. A review of water treatment membrane nanotechnologies. *Energy Environ. Sci.*, 4:1946–1971, 2011.

[9] M. Dahanayaka, B. Liu, Z. Hu, Q. X. Pei, Z. Chen, A. W. K. Law, and K. Zhou. Graphene membranes with nanoslits for seawater desalination via forward osmosis. *Phys. Chem. Chem. Phys.*, 19:30551–30561, 2017.

[10] J. G. Gai, X. L. Gong, W. W. Wang, X. Zhang, and W. L. Kang. An ultrafast water transport forward osmosis membrane: Porous graphene. *J. Mater. Chem. A*, 2:4023–4028, 2014.

[11] M. Heiranian, A. B. Farimani, and N. R. Aluru. Water desalination with a single-layer MoS_2 nanopore. *Nat. Commun.*, 6(8616):1–6, 2015.

[12] H. W. Kim, H. W. Yoon, S. M. Yoon, B. M. Yoo, B. K. Ahn, Y. H. Cho, H. J. Shin, H. Yang, U. Paik, S. Kwon, J. Y. Choi, and H. B. Park. Selective gas transport through few-layered graphene and graphene oxide membranes. *Science*, 342(6154):91–95, 2013.

[13] R. R. Nair, H. A. Wu, P. N. Jayaram, I. V. Grigorieva, and A. K. Geim. Unimpeded permeation of water through helium-leak-tight graphene-based membranes. *Science*, 335(6067):442–444, 2012.

[14] M. Shahbabaei and D. Kim. Molecular dynamics simulation of water transport mechanisms through nanoporous boron nitride and graphene multilayers. *J. Phys. Chem. B*, 121(16):4137–4144, 2017.

[15] D. C. Tanugi and J. C. Grossman. Water desalination across nanoporous graphene. *Nano Lett.*, 12(7):3602–3608, 2012.

[16] J. Abraham, K. S. Vasu, C. D. Williams, K. Gopinadhan, Y. Su, C. T. Cherian, J. Dix, E. Prestat, S. J. Haigh, I. V. Grigorieva, P. Carbone, A. K. Geim, and R. R. Nair. Tunable sieving of ions using graphene oxide membranes. *Nat. Nanotechnol.*, 12:546–550, 2017.

[17] D. An, L. Yang, T. J. Wang, and B. Liu. Separation performance of graphene oxide membrane in aqueous solution. *Ind. Eng. Chem. Res.*, 5(17):4803–4810, 2016.

[18] A. Buchsteiner, A. Lerf, and J. Pieper. Water dynamics in graphite oxide investigated with neutron scattering. *J. Phys. Chem. B*, 110(45):22328–22338, 2006.

[19] A. Lerf, A. Buchsteiner, J. Pieper, S. Schöttl, I. Dekany, T. Szabo, and H.P. Boehm. Hydration behavior and dynamics of water molecules in graphite oxide. *J. Phys. Chem. Solids*, 67:1106–1110, 2006.

[20] F. Perreault, A. F. de Faria, and M. Elimelech. Environmental applications of graphene-based nanomaterials. *Chem. Soc. Rev.*, 44:5861–5896, 2015.

[21] S. Safaei and R. Tavakoli. On the design of graphene oxide nanosheets membranes for water desalination. *Desalination*, 422:83–90, 2017.

[22] T. Yu, Z. Xu, S. Liu, H. Liu, and X. Yang. Enhanced hydrophilicity and water-permeating of functionalized graphene-oxide nanopores: Molecular dynamics simulations. *J. Membr. Sci.*, 550:510–517, 2018.

[23] S. Zheng, Q. Tu, J. J. Urban, S. Li, and B. Mi. Swelling of graphene oxide membranes in aqueous solution: Characterization of interlayer spacing and insight into water transport mechanisms. *ACS Nano*, 11(6):6440–6450, 2017.

[24] A. Lerf, H. He, M. Forster, and J. Klinowski. Structure of graphite oxide revisited. *J. Phys. Chem. B*, 102(23):4477–4482, 1998.

[25] R. K. Joshi, P. Carbone, F. C. Wang, V. G. Kravets, Y. Su, I. V. Grigorieva, H. A. Wu, A. K. Geim, and R. R. Nair. Precise and ultrafast molecular sieving through graphene oxide membranes. *Science*, 343(6172):752–754, 2014.

[26] K. Raidongia and J. Huang. Nanofluidic ion transport through reconstructed layered materials. *J. Am. Chem. Soc.*, 134(40):16528–16531, 2012.

[27] Y. Zhu, S. Murali, W. Cai, X. Li, J. W. Suk, J. R. Potts, and R. S. Ruoff. Graphene and graphene oxide: Synthesis, properties, and applications. *Adv. Mater.*, 22:3906–3924, 2010.

[28] H. Huang, Z. Song, N. Wei, L. Shi, Y. Mao, Y. Ying, L. Sun, Z. Xu, and X. Peng. Ultrafast viscous water flow through nanostrand-channelled graphene oxide membranes. *Nat. Commun.*, 4(2979):1–9, 2013.

[29] K. Huang, G. Liu, Y. Lou, Z. Dong, J. Shen, and W. Jin. A graphene oxide membrane with highly selective molecular separation of aqueous organic solution. *Angew. Chem., Int. Ed.*, 53:6929–6932, 2014.

[30] H. Li, Z. Song, X. Zhang, Y. Huang, S. Li, Y. Mao, H. J. Ploehn, Y. Bao, and M. Yu. Ultrathin, molecular-sieving graphene oxide membranes for selective hydrogen separation. *Science*, 342(6154):95–98, 2013.

[31] L. Chen, G. Shi, J. Shen, B. Peng, B. Zhang, Y. Wang, F. Bian, J. Wang, D. Li, Z. Qian, G. Xu, G. Liu, J. Zeng, L. Zhang, Y. Yang, G. Zhou, M. Wu, W. Jin, J. Li, and H. Fang. Ion sieving in graphene oxide membranes via cationic control of interlayer spacing. *Nature*, 550:380–383, 2017.

[32] M. Hu and B. Mi. Enabling graphene oxide nanosheets as water separation membranes. *Environ. Sci. Technol.*, 47(8):3715–3723, 2013.

[33] Z. Luo, Y. Lu, L. A. Somers, and A. T. C. Johnson. High yield preparation of macroscopic graphene oxide membranes. *J. Am. Chem. Soc.*, 131(3):898–899, 2009.

[34] Y. H. Xi, J. Q. Hu, Z. Liu, R. Xie, X. J. Ju, W. Wang, and L. Y. Chu. Graphene oxide membranes with strong stability in aqueous solutions and controllable lamellar spacing. *ACS Appl. Mater. Interfaces*, 8(24):15557–15566, 2016.

[35] A. Gogoi, T. J. Konch, K. Raidongia, and K. A. Reddy. Water and salt dynamics in multilayer graphene oxide (GO) membrane: Role of lateral sheet dimensions. *J. Membr. Sci.*, 563:785–793, 2018.

[36] H. Huang, Z. Song, N. Wei, L. Shi, Y. Mao, Y. Ying, L. Sun, Z. Xu, and X. Peng. Ultrafast viscous water flow through nanostrandchannelled graphene oxide membranes. *Nat. Commun.*, 4(2979):1–9, 2013.

[37] L. Jin, Z. Wang, S. Zheng, and B. Mi. Polyamide-crosslinked graphene oxide membrane for forward osmosis. *J. Membr. Sci.*, 545:11–18, 2018.

[38] L. Shen, S. Xiong, and Y. Wang. Graphene oxide incorporated thin-film composite membranes for forward osmosis applications. *Chem. Eng. Sci.*, 143:194–205, 2016.

[39] D. R. Dreyer, S. Park, C. W. Bielawski, and R. S. Ruoff. The chemistry of graphene oxide. *Chem. Soc. Rev.*, 39:228–240, 2010.

[40] H. Kim, A. A. Abdala, and C. W. Macosko. Graphene/polymer nanocomposites. *Macromolecules*, 43(16):6515–6530, 2010.

[41] D. A. Dikin, S. Stankovich, E. J. Zimney, R. D. Piner, G. H. B. Dommett, G. Evmenenko, S. T. Nguyen, and R. S. Ruoff. Preparation and characterization of graphene oxide paper. *Nature*, 448:457–460, 2007.

[42] L. Huang, M. Seredych, T. J. Bandosz, and A. C. T. van Duin. Controllable atomistic graphene oxide model and its application in hydrogen sulfide removal. *J. Chem. Phys.*, 139:194707, 2013.

[43] B. Christie. The big idea-get the salt out. *National Geographic*, 2010.

[44] B. J. Alder and T. E. Wainwright. Phase transition for a hard sphere system. *J. Chem. Phys.*, 27:1208–1209, 1957.

[45] W. L. Jorgensen, D. S. Maxwell, and J. T. Rives. Development and testing of the opls all-atom force field on conformational energetics and properties of organic liquids. *J. Am. Chem. Soc.*, 118(45):11225–11236, 1996.

[46] C. J. Shih, S. Lin, R. Sharma, M. S. Strano, and D. Blankschtein. Understanding the ph-dependent behavior of graphene oxide aqueous solutions: A comparative experimental and molecular dynamics simulation study. *Langmuir*, 28(1):235–241, 2012.

[47] H. H. G. Savenije. Water scarcity indicators; the deception of the numbers. *Phys. Chem. Earth*, 25(3):199–204, 2000.

[48] A. Y. Hoekstra. A critique on the water-scarcity weighted water footprint in LCA. *Ecol. Indic.*, 66:564–573, 2016.

[49] A. Y. Hoekstra. Water scarcity challenges to business. *Nat. Clim. Change*, 4:318–320, 2014.

[50] F. R. Rijsberman. Water scarcity: Fact or fiction? *Agric. Water Manag*, 80:5–22, 2006.

[51] D. Seckler, R. Barker, and U. Amarasinghe. Water scarcity in the twenty-first century. *Int. J. Water Resour. Dev.*, 15(1-2):29–49, 2010.

[52] M. Elimelech. The global challenge for adequate and safe water. *J. Water Supply Res. T.*, 55(1):3–10, 2006.

[53] M. A. Shannon, P. W. Bohn, M. Elimelech, J. G. Georgiadis, B. J. Mariñas, and A. M. Mayes. Science and technology for water purification in the coming decades. *Nature*, 452:301–310, 2008.

[54] A. M. Comerton, R. C. Andrews, D. M. Bagley, and C. Hao. The rejection of endocrine disrupting and pharmaceutically active compounds by NF and RO membranes as a function of compound and water matrix properties. *J. Membr. Sci.*, 313(1-2):323–335, 2008.

[55] K. Kimura, S. Toshima, G. Amy, and Y. Watanabe. Rejection of neutral endocrine disrupting compounds (EDCs) and pharmaceutical active compounds (PhACs) by RO membranes. *J. Membr. Sci.*, 245(1-2):71–78, 2004.

[56] J. E. Gu, B. M. Jun, and Y. N. Kwon. Effect of chlorination condition and permeability of chlorine species on the chlorination of a polyamide membrane. *Water Res.*, 46(16):5389–5400, 2012.

[57] D. H. Shin, N. Kim, and Y. T. Lee. Modification to the polyamide TFC RO membranes for improvement of chlorine-resistance. *J. Membr. Sci.*, 376(1-2):302–311, 2011.

[58] Y. Liu and B. Mi. Combined fouling of forward osmosis membranes: Synergistic foulant interaction and direct observation of fouling layer formation. *J. Membr. Sci.*, 407-408:136–144, 2012.

[59] B. Mi and M. Elimelech. Gypsum scaling and cleaning in forward osmosis: Measurements and mechanisms. *Environ. Sci. Technol.*, 44(6):2022–2028, 2010.

[60] B. Mi and M. Elimelech. Organic fouling of forward osmosis membranes: Fouling reversibility and cleaning without chemical reagents. *J. Membr. Sci.*, 348(1-2):337–345, 2010.

[61] B. Mi and M. Elimelech. Silica scaling and scaling reversibility in forward osmosis. *Desalination*, 312:75–81, 2013.

[62] D. L. Shaffer, N. Y. Yip, J. Gilron, and M. Elimelech. Seawater desalination for agriculture by integrated forward and reverse osmosis: Improved product water quality for potentially less energy. *J. Membr. Sci.*, 415-416:1–8, 2012.

[63] J. R. McCutcheon and M. Elimelech. Modeling water flux in forward osmosis: Implications for improved membrane design. *AIChE J.*, 53(7):1736–1744, 2007.

[64] L. Ai, C. Zhang, and Z. Chen. Removal of methylene blue from aqueous solution by a solvothermal-synthesized graphene/magnetite composite. *J. Hazard. Mater.*, 192(3):1515–1524, 2011.

[65] Z. H. Huang, X. Zheng, W. Lv, M. Wang, Q. H. Yang, and F. Kang. Adsorption of lead(II) ions from aqueous solution on low-temperature exfoliated graphene nanosheets. *Langmuir*, 27(12):7558–7562, 2011.

[66] S. Liu, T. H. Zeng, M. Hofmann, E. Burcombe, J. Wei, R. Jiang, J. Kong, and Y. Chen. Antibacterial activity of graphite, graphite oxide, graphene oxide, and reduced graphene oxide: Membrane and oxidative stress. *ACS Nano*, 5(9):6971–6980, 2011.

[67] M. Machida, T. Mochimaru, and H. Tatsumoto. Lead(ii) adsorption onto the graphene layer of carbonaceous materials in aqueous solution. *Carbon*, 44(13):2681–2688, 2006.

[68] A. K. Mishra and S. Ramaprabhu. Functionalized graphene sheets for arsenic removal and desalination of sea water. *Desalination*, 282:39–45, 2011.

[69] K. Zhang, K. C. Kemp, and V. Chandra. Homogeneous anchoring of TiO_2 nanoparticles on graphene sheets for waste water treatment. *Mater. Lett.*, 81:127–130, 2012.

[70] M. E. Suk and N. R. Aluru. Water transport through ultrathin graphene. *J. Phys. Chem. Lett.*, 1(10):1590–1594, 2010.

[71] S. P. Koenig, L. Wang, J. Pellegrino, and J. Scott Bunch. Selective molecular sieving through porous graphene. *Nat. Nanotechnol.*, 7:728–732, 2012.

[72] W. S. Hummers and R. E. Offeman. Preparation of graphitic oxide. *J. Am. Chem. Soc.*, 80(6):1339–1339, 1958.

[73] J. Shen, M. Shi, H. Ma, B. Yan, N. Li, Y. Hu, and M. Ye. Synthesis of hydrophilic and organophilic chemically modified graphene oxide sheets. *J. Colloid Interface Sci.*, 352(2):366–370, 2010.

[74] G. Shao, Y. Lu, F. Wu, C. Yang, F. Zeng, and Q. Wu. Graphene oxide: the mechanisms of oxidation and exfoliation. *J. Mater. Sci.*, 47:4400–4409, 2012.

[75] M. Fathizadeh, W. L. Xu, F. Zhou, Y. Yoon, and M. Yu. Graphene oxide: A novel 2-dimensional material in membrane separation for water purification. *Adv. Mater. Interfaces*, 4(5):1–16, 2017.

[76] H. M. Hegab and L. Zou. Graphene oxide-assisted membranes: Fabrication and potential applications in desalination and water purification. *J. Membr. Sci.*, 484:95–106, 2015.

[77] S. Hong, C. Constans, M. V. S. Martins, Y. C. Seow, J. A. G. Carrió, and S. Garaj. Scalable graphene-based membranes for ionic sieving with ultrahigh charge selectivity. *Nano Lett.*, 17(2):728–732, 2016.

[78] B. Mi. Graphene oxide membranes for ionic and molecular sieving. *Science*, 343(6172):740–742, 2014.

[79] Q. Xu, H. Xu, J. Chen, Y. Lv, C. Dong, and T. S. Sreeprasad. Graphene and graphene oxide: Advanced membranes for gas separation and water purification. *Inorg. Chem. Front.*, 2(5):417–424, 2015.

[80] Q. Yang, Y. Su, C. Chi, C. T. Cherian, K. Huang, V. G. Kravets, F. C. Wang, J. C. Zhang, A. Pratt, A. N. Grigorenko, F. Guinea, A. K. Geim, and R. R. Nair. Ultrathin graphene-based membrane with precise molecular sieving and ultrafast solvent permeation. *Nat. Mater.*, 16:1198–1202, 2017.

[81] C. Chen, Q. H. Yang, Y. Yang, W. Lv, Y. Wen, P. X. Hou, M. Wang, and H. M. Cheng. Self-assembled free-standing graphite oxide membrane. *Adv. Mater.*, 21(29):3007–3011, 2009.

[82] J. C. Meyer, A. K. Geim, M. I. Katsnelson, K. S. Novoselov, T. J. Booth, and S. Roth. The structure of suspended graphene sheets. *Nature*, 446:60–63, 2007.

[83] Z. P. Smith and B. D. Freeman. Graphene oxide: A new platform for high-performance gas- and liquid-separation membranes. *Angew. Chem. Int. Ed.*, 53(39):10286–10288, 2014.

[84] G. Chen, S. Zhai, Y. Zhai, K. Zhang, Q. Yue, L. Wang, J. Zhao, H. Wang, J. Liu, and J. Jiac. Preparation of sulfonic-functionalized graphene oxide as ion-exchange material and its application into electrochemiluminescence analysis. *Biosens. Bioelectron.*, 26(7):3136–3141, 2011.

[85] J. Hong, Y. S. Kang, and S. W. Kang. Nanoassembly of block copolymer micelle and graphene oxide to multilayer coatings. *Ind. Eng. Chem. Res.*, 50(6):3095–3099, 2011.

[86] M. J. F. Merino, J. I. Paredes, S. V. Rodil, L. Guardia, P. S. Fernández, D. S. Torres, D. C. Amorós, E. Morallón, A. M. Alonso, and J. M. D. Tascón. Investigating the influence of surfactants on the stabilization of aqueous reduced graphene oxide dispersions and the characteristics of their composite films. *Carbon*, 50(9):3184–3194, 2012.

[87] S. Salgado, L. Pu, and V. Maheshwari. Targeting chemical morphology of graphene oxide for self-assembly and subsequent templating of nanoparticles: A composite approaching capacitance limits in graphene. *J. Phys. Chem. A*, 116(22):12124–12130, 2012.

[88] R. L. D. Whitby, A. Korobeinyk, S. V. Mikhalovsky, T. Fukuda, and T. Maekawa. Morphological effects of single-layer graphene oxide in the formation of covalently bonded polypyrrole composites using intermediate diisocyanate chemistry. *J. Nanopart. Res.*, 13(10):4829–4837, 2011.

[89] L. Q. Xu, L. Wang, B. Zhang, C. H. Lim, Y. Chen, K. G. Neoh, E. T. Kang, and G. D. Fu. Functionalization of reduced graphene oxide nanosheets via stacking interactions with the fluorescent and water-soluble perylene bisimide-containing polymers. *Polymer*, 52(11):2376–2383, 2011.

[90] M. Koinuma, C. Ogata, Y. Kamei, K. Hatakeyama, H. Tateishi, Y. Watanabe, T. Taniguchi, K. Gezuhara, S. Hayami, A. Funatsu, M. Sakata, Y. Kuwahara,

S. Kurihara, and Y. Matsumoto. Photochemical engineering of graphene oxide nanosheets. *J. Phys. Chem. C*, 116(37):19822–19827, 2012.

[91] Y. S. Choi, C. Yeo, S. J. Kim, J. Y. Lee, Y. Kim, K. R. Cho, S. Ju, B. H. Hong, and S. Y. Park. Multifunctional reduced graphene oxide-CVD graphene core-shell fibers. *Nanoscale*, 11(26):12637–12642, 2019.

[92] H. Huang, Y. Ying, and X. Peng. Graphene oxide nanosheet: an emerging star material for novel separation membranes. *J. Mater. Chem. A*, 2(34):13772–13782, 2014.

[93] P. Sun, K. Wang, and H. Zhu. Recent developments in graphene-based membranes: Structure, mass-transport mechanism and potential applications. *Adv. Mater.*, 28(12):2287–2310, 2016.

[94] K. Yang, L. Huang, Y. Wang, Y. Du, J. Tang, Y. Wang, M. Cheng, Y. Zhang, M. J. Kipper, L. A. Belfiore, and S. R. Wickramasinghe. Graphene oxide/nanometal composite membranes for nanofiltration: Synthesis, mass transport mechanism, and applications. *New J. Chem.*, 43(7):2846–2860, 2019.

[95] K. Goh, L. Setiawan, L. Wei, R. Si, A. G. Fane, R. Wang, and Y. Chen. Graphene oxide as effective selective barriers on a hollow fiber membrane for water treatment process. *J. Membr. Sci.*, 474:244–253, 2015.

[96] J. Lee, J. H. Jang, H. R. Chae, S. H. Lee, C. H. Lee, P. K. Park, Y. J. Won, and I. C. Kim. A facile route to enhance the water flux of a thin-film composite reverse osmosis membrane: Incorporating thickness-controlled graphene oxide into a highly porous support layer. *J. Mater. Chem. A*, 3(44):22053–22060, 2015.

[97] B. P. V. Nellore, R. Kanchanapally, F. Pedraza, S. S. Sinha, A. Pramanik, A. T. Hamme, Z. Arslan, D. Sardar, and P. C. Ray. Bio-conjugated CNT-bridged 3d porous graphene oxide membrane for highly efficient disinfection of pathogenic bacteria and removal of toxic metals from water. *ACS Appl. Mater. Interfaces*, 7(34):19210–19218, 2015.

[98] F. Guo, M. Creighton, Y. Chen, R. Hurt, and I. Külaots. Porous structures in stacked, crumpled and pillared graphene-based 3d materials. *Carbon*, 66:476–484, 2014.

[99] R. K. Joshi, S. Alwarappan, M. Yoshimura, V. Sahajwalla, and Y. Nishina. Graphene oxide: the new membrane material. *Appl. Mater. Today*, 1(1):1–12, 2015.

[100] W. S. Hung, Q. F. An, M. De Guzman, H. Y. Lin, S. H. Huang, W. R. Liu, C. C. Hu, K. R. Lee, and J. Y. Lai. Pressure-assisted self-assembly technique for fabricating composite membranes consisting of highly ordered selective laminate layers of amphiphilic graphene oxide. *Carbon*, 68:670–677, 2014.

[101] P. Sun, M. Zhu, K. Wang, M. Zhong, J. Wei, D. Wu, Z. Xu, and H. Zhu. Selective ion penetration of graphene oxide membranes. *ACS Nano*, 7(1):428–437, 2013.

[102] P. Sun, K. Wang, J. Wei, M. Zhong, D. Wu, and H. Zhu. Effective recovery of acids from iron-based electrolytes using graphene oxide membrane filters. *J. Mater. Chem. A*, 2:7734–7737, 2014.

[103] P. Sun, F. Zheng, M. Zhu, Z. Song, K. Wang, M. Zhong, D. Wu, R. B. Little, Z. Xu, and H. Zhu. Selective trans-membrane transport of alkali and alkaline earth cations through graphene oxide membranes based on cation-π interactions. *ACS Nano*, 8(1):850–859, 2014.

[104] H. Huang, Y. Mao, Y. Ying, Y. Liu, L. Sun, and X. Peng. Salt concentration, pH and pressure controlled separation of small molecules through lamellar graphene oxide membranes. *Chem. Commun.*, 49(53):5963–5965, 2013.

[105] Y. Su, V. G. Kravets, S. L. Wong, J. Waters, A. K. Geim, and R. R. Nair. Impermeable barrier films and protective coatings based on reduced graphene oxide. *Nat. Commun.*, 5(4843):1–5, 2014.

[106] A. Soroush, W. Ma, Y. Silvino, and Md. S. Rahaman. Surface modification of thin film composite forward osmosis membrane by silver-decorated graphene-oxide nanosheets. *Environ. Sci.: Nano*, 2:395–405, 2015.

[107] B. Chen, H. Jiang, X. Liu, and X. Hu. Observation and analysis of water transport through graphene oxide interlamination. *J. Phys. Chem. C*, 121(2):1321–1328, 2017.

[108] B. Chen, H. Jiang, X. Liu, and X. Hu. Molecular insight into water desalination across multilayer graphene oxide membranes. *ACS Appl. Mater. Interfaces*, 9:22826–22836, 2017.

[109] H. Dai, Z. Xu, and X. Yang. Water permeation and ion rejection in layer-by-layer stacked graphene oxide nanochannels: A molecular dynamics simulation. *J. Phys. Chem. C*, 120(39):22585–22596, 2016.

[110] B. Chen, H. Jiang, X. Liu, and X. Hu. Water transport confined in graphene oxide channels through the rarefied effect. *Phys. Chem. Chem. Phys.*, 20:9780–9786, 2018.

[111] S. Ban, J. Xie, Y. Wang, B. Jing, B. Liu, and H. Zhou. Insight into the nanoscale mechanism of rapid H_2O transport within a graphene oxide membrane: Impact of oxygen functional group clustering. *ACS Appl. Mater. Interfaces*, 8(1):321–332, 2016.

[112] N. Wei, X. Peng, and Z. Xu. Understanding water permeation in graphene oxide membranes. *ACS Appl. Mater. Interfaces*, 6(8):5877–5883, 2014.

[113] D. Qin, Z. Liu, D. D. Sun, X. Song, and H. Bai. A new nanocomposite forward osmosis membrane custom-designed for treating shale gas wastewater. *Sci. Rep.*, 5(14530):1–13, 2015.

[114] C. Klaysom, T. Y. Cath, T. Depuydt, and I. F. J. Vankelecom. Forward and pressure retarded osmosis: Potential solutions for global challenges in energy and water supply. *Chem. Soc. Rev.*, 42:6959–6989, 2013.

[115] Z. Wang, J. Zheng, J. Tang, X. Wang, and Z. Wu. A pilot-scale forward osmosis membrane system for concentrating low-strength municipal wastewater: Performance and implications. *Sci. Rep.*, 6(21653):1–11, 2016.

[116] Q. Saren, C. Q. Qiu, and C. Y. Tang. Synthesis and characterization of novel forward osmosis membranes based on layer-by-layer assembly. *Environ. Sci. Technol.*, 45:5201–5208, 2011.

[117] S. You, C. Tang, C. Yu, X. Wang, J. Zhang, J. Han, Y. Gan, and N. Ren. Forward osmosis with a novel thin-film inorganic membrane. *Environ. Sci. Technol.*, 47:8733–8742, 2013.

[118] S. Qi, Y. Li, Y. Zhao, W. Li, and C. Y. Tang. Highly efficient forward osmosis based on porous membranes applications and implications. *Environ. Sci. Technol.*, 49:4690–4695, 2015.

[119] Y. Wang, F. Wicaksana, C. Y. Tang, and A. G. Fane. Direct microscopic observation of forward osmosis membrane fouling. *Environ. Sci. Technol.*, 44(18):7102–7109, 2010.

[120] E. A. Bell, R. W. Holloway, and T. Y. Cath. Evaluation of forward osmosis membrane performance and fouling during long-term osmotic membrane bioreactor study. *J. Membr. Sci.*, 517:1–13, 2016.

[121] H. Q. Liang, W. S. Hung, H. H. Yu, C. C. Hu, K. R. Lee, J. Y. Lai, and Z. K. Xu. Forward osmosis membranes with unprecedented water flux. *J. Membr. Sci.*, 529:47–54, 2017.

[122] D. Emadzadeh, W. J. Lau, T. Matsuura, N. Hilal, and A. F. Ismail. The potential of thin film nanocomposite membrane in reducing organic fouling in forward osmosis process. *Desalination*, 348:82–88, 2014.

[123] Y. Han, Z. Xu, and C. Gao. Ultrathin graphene nanofiltration membrane for water purification. *Adv. Funct. Mater.*, 23(29):3693–3700, 2013.

[124] L. Garwin and K. E. Hutchison. Separation of acetic acid and water by distillation. *Ind. Eng. Chem.*, 42(4):727–730, 1950.

[125] H. P. Huang, H. Y. Lee, , and T. K. Gau. Design and control of acetic acid dehydration column with p-xylene or m-xylene feed impurity. 1. importance of feed tray location on the process design. *Ind. Eng. Chem. Res.*, 46:505–517, 2007.

[126] X. Huang, W. Zhong, W. Du, and F. Qian. Thermodynamic analysis and process simulation of an industrial acetic acid dehydration system via heterogeneous azeotropic distillation. *Ind. Eng. Chem. Res.*, 52:2944–2957, 2013.

[127] Z. Lei, C. Li, Y. Li, and B. Chen. Separation of acetic acid and water by complex extractive distillation. *Sep. Purif. Technol.*, 36:131–138, 2004.

[128] D. F. Othmer. Separation of water from acetic acid by azeotropic distillation. *Ind. Eng. Chem.*, 27(3):250–255, 1935.

[129] W. Zhang, Y. Xu, Z. Yu, S. Lu, and X. Wang. Separation of acetic acid/water mixtures by pervaporation with composite membranes of sodium alginate active layer and microporous polypropylene substrate. *J. Appl. Sci.*, 451:135–147, 2014.

[130] T. Sano, S. Ejiri, K. Yamada, Y. Kawakami, and H. Yanagishita. Separation of acetic acid-water mixtures by pervaporation through silicalite membrane. *J. Membr. Sci.*, 123:225–233, 1997.

[131] D. L. Grzenia, D. J. Schell, and S. R. Wickramasinghe. Membrane extraction for removal of acetic acid from biomass hydrolysates. *J. Membr. Sci.*, 322:189–195, 2008.

[132] S. C. Huang, I. J. Ball, and R. B. Kaner. Polyaniline membranes for pervaporation of carboxylic acids and water. *Macromolecules*, 31(16):5456–5464, 1998.

[133] N. Jullok, S. Darvishmanesh, P. Luis, and B. V. der Bruggen. The potential of pervaporation for separation of acetic acid and water mixtures using polyphenylsulfone membranes. *Chem. Eng. Sci.*, 175:306–315, 2011.

[134] N. Jullok, T. Deforche, P. Luis, and B. V. der Bruggen. Sorption and diffusivity study of acetic acid and water in polymeric membranes. *Chem. Eng. Sci.*, 70:14–20, 2012.

[135] N. Jullok, R. V. Hooghten, P. Luis, A. Volodin, C. V. Haesendonck, J. Vermant, and B. V. der Bruggen. Effect of silica nanoparticles in mixed matrix membranes for pervaporation dehydration of acetic acid aqueous solution: Plant-inspired dewatering systems. *J. Cleaner Prod.*, 112:4879–4889, 2016.

[136] N. Alghezawi, O. Şanlı, L. Aras, and G. Asman. Separation of acetic acid-water mixtures through acrylonitrile grafted poly(vinyl alcohol) membranes by pervaporation. *Chem. Eng. Process.*, 44(1):51–58, 2005.

[137] Y. C. Wang, C. L. Li, P. F. Chang, S. C. Fan, K. R. Lee, and J. Y. Lai. Separation of water-acetic acid mixture by pervaporation through plasma-treated asymmetric poly(4-methyl-1-pentene) membrane and dip-coated with polyacrylic acid. *J. Membr. Sci.*, 208(1-2):3–12, 2002.

[138] Z. Chen, D. Yin, Y. Li, J. Yang, J. Lu, Y. Zhang, and J. Wang. Functional defect-patching of a zeolite membrane for the dehydration of acetic acid by pervaporation. *J. Membr. Sci.*, 369(1-2):506–513, 2011.

[139] M. D. Afonso. Assessment of NF and RO for the potential concentration of acetic acid and furfural from the condensate of eucalyptus spent sulphite liquor. *Sep. Purif. Technol.*, 99:86–90, 2012.

[140] A. Teella, G. W. Huber, and D. M. Ford. Separation of acetic acid from the aqueous fraction of fast pyrolysis bio-oils using nanofiltration and reverse osmosis membranes. *J. Membr. Sci.*, 378:495–502, 2011.

[141] R. L. G. Lecaros, G. E. J. Mendoza, W. S. Hung, Q. F. An, A. R. Caparanga, H. A. Tsai, C. C. Hu, K. R. Lee, and J. Y. Lai. Tunable interlayer spacing of composite graphene oxide-framework membrane for acetic acid dehydration. *Carbon*, 123:660–667, 2017.

[142] K. Xu, Z. Jiang, B. Feng, and A. Huang. A graphene oxide layer as an acid-resisting barrier deposited on a zeolite lta membrane for dehydration of acetic acid. *RSC Adv.*, 6:23354–23359, 2016.

[143] T. Ruprakobkit, L. Ruprakobkit, and C. Ratanatamskul. Carboxylic acid concentration by forward osmosis processes: Dynamic modeling, experimental validation and simulation. *Chem. Eng. J.*, 306:538–549, 2016.

[144] R. Qiao and N. R. Aluru. Ion concentrations and velocity profiles in nanochannel electroosmotic flows. *J. Chem. Phys.*, 118(10):4692–4701, 2003.

[145] H. A. Stone, A. D. Stroock, and A. Ajdari. Engineering flows in small devices: Microfluidics toward a lab-on-a-chip. *Annu. Rev. Fluid Mech.*, 36:381–411, 2004.

[146] P. Dutta, A. Beskok, and T. C. Warburton. Electroosmotic flow control in complex microgeometries. *J. Microelectromech. Syst.*, 11(1):36–44, 2002.

[147] P. J. Kemery, J. K. Steehler, and P. W. Bohn. Electric field mediated transport in nanometer diameter channels. *Langmuir*, 14(10):2884–2889, 1998.

[148] T. C. Kuo, L. A. Sloan, J. V. Sweedler, and P. W. Bohn. Manipulating molecular transport through nanoporous membranes by control of electrokinetic flow: Effect of surface charge density and debye length. *Langmuir*, 17(20):6298–6303, 2001.

[149] H. Ban, B. Lin, and Z. Song. Effect of electrical double layer on electric conductivity and pressure-drop in a pressure driven microchannel flow. *Biomicrofluidics*, 4(1):014104, 2010.

[150] I. C. Bourg and G. Sposito. Molecular dynamics simulations of the electrical double layer on smectitesurfaces contacting concentrated mixed electrolyte (nacl-cacl2) solutions. *J. Colloid Interface Sci.*, 360(2):701–715, 2011.

[151] E. Boyko, R. Eshel, A. D. Gat, and M. Bercovici. Nonuniform electro-osmotic flow drives fluid-structure instability. *Phys. Rev. Lett.*, 124(2):024501, 2020.

[152] G. Cassone, G. Calogero, J. Sponer, and F. Saija. Mobilities of iodide anions in aqueous solutions for applications in natural dye-sensitized solar cells. *Phys. Chem. Chem. Phys.*, 20(18):13038–13046, 2018.

[153] G. Cassone, D. Chillé, C. Foti, O. Giuffré, R. C. Ponterio, J. Sponer, and F. Saija. Stability of hydrolytic arsenic species in aqueous solutions: As^{3+} vs. As^{5+}. *Phys. Chem. Chem. Phys.*, 20(36):23272–23280, 2018.

[154] G. Cassone, F. Creazzo, P. V. Giaquinta, J. Sponer, and F. Saija. Ionic diffusion and proton transfer in aqueous solutions of alkali metal salts. *Phys. Chem. Chem. Phys.*, 19(31):20420–20429, 2017.

[155] A. T. Celebi and A. Beskok. Molecular and continuum transport perspectives on electroosmotic slip flows. *J. Phys. Chem. C*, 122(17):9699–9709, 2018.

[156] X. Chen, Y. Ren, T. Jiang, L. Hou, and H. Jiang. High-throughput and multimodal separation of microbeads using cyclical induced-charge electro-osmotic vortices and its application in size fractionation of crumpled graphene oxide balls. *Appl. Mater. Today*, 19:100545, 2020.

[157] A. V. Delgado, F. González-Caballero, R. J. Hunter, L. K. Koopal, and J. Lyklema. Measurement and interpretation of electrokinetic phenomena. *J. Colloid Interface Sci.*, 309(2):194–224, 2007.

[158] A. P. Gaiduk, C. Zhang, F. Gygi, and G. Galli. Structural and electronic properties of aqueous NaCl solutions from ab initio molecular dynamics simulations with hybrid density functionals. *Chem. Phys. Lett.*, 604:89–96, 2014.

[159] A. Haque, A. K. Nayak, B. Weigand, and A. Banerjee. Time-dependent electroosmotic flow with variable slips along microchannel. *Ind. Eng. Chem. Res.*, 59(2):942–955, 2020.

[160] D. J. Harrison, K. Fluri, K. Seiler, Z. Fan, C. S. Effenhauser, and A. Manz. Micromachining a miniaturized capillary electrophoresis-based chemical analysis system on a chip. *Science*, 261(5123):895–897, 1993.

[161] C. H. Hou, P. Taboada-Serrano, S. Yiacoumi, and C. Tsouris. Monte carlo simulation of electrical double-layer formation from mixtures of electrolytes inside nanopores. *J. Chem. Phys.*, 128:044705, 2008.

[162] L. Joly, C. Ybert, E. Trizac, and L. Bocquet. Hydrodynamics within the electric double layer on slipping surfaces. *Phys. Rev. Lett.*, 93(25):257805, 2004.

[163] L. Joly, C. Ybert, E. Trizac, and L. Bocquet. Liquid friction on charged surfaces: From hydrodynamic slippage to electrokinetics. *J. Chem. Phys.*, 125:204716, 2006.

[164] T. C. Kuo, Jr. D. M. Cannon, Y. Chen, J. J. Tulock, M. A. Shannon, J. V. Sweedler, and P. W. Bohn. Gateable nanofluidic interconnects for multilayered microfluidic separation systems. *Anal. Chem.*, 75(8):1861–1867, 2003.

[165] A. Lehmani, O. Bernard, and P. Turq. Transport of ions and solvent in confined media. *J. Stat. Phys.*, 89:379–402, 1997.

[166] I. Llorente, S. Fajardo, and J. M. Bastidas. Applications of electrokinetic phenomena in materials science. *J. Solid State Electrochem.*, 18:293–307, 2014.

[167] C. D. Lorenz, P. S. Crozier, J. A. Anderson, and A. Travesset. Molecular dynamics of ionic transport and electrokinetic effects in realistic silica channels. *J. Phys. Chem. C*, 112(27):10222–10232, 2008.

[168] L. S. Puah, R. Sedev, D. Fornasiero, J. Ralston, and T. Blake. Influence of surface charge on wetting kinetics. *Langmuir*, 26(22):17218–17224, 2010.

[169] D. R. Reyes, D. Iossifidis, P. A. Auroux, and A. Manz. Micro total analysis systems. 1. introduction, theory, and technology. *Anal. Chem.*, 74(12):2623–2636, 2002.

[170] M. Rezaei, A. R. Azimian, A. R. Pishevar, and D. J. Bonthuis. Viscous interfacial layer formation causes electroosmotic mobility reversal in monovalent electrolytes. *Phys. Chem. Chem. Phys.*, 20(35):22517–22524, 2018.

[171] M. Rezaei, A. R. Azimian, and D. Toghraie. Molecular dynamics study of an electro-kinetic fluid transport in a charged nanochannel based on the role of the stern layer. *Phys. A (Amsterdam, Neth.)*, 426:25–34, 2015.

[172] B. D. Storey and M. Z. Bazant. Effects of electrostatic correlations on electrokinetic phenomena. *Phys. Rev. E*, 86(5):056303, 2012.

[173] T. Zhou, L. Shi, C. Fan, D. Liang, S. Weng, and S. W. Joo. A novel scalable microfluidic load sensor based on electrokinetic phenomena. *Microfluid. Nanofluid.*, 21:59, 2017.

[174] C. Cameselle. Enhancement of electro-osmotic flow during the electrokinetic treatment of a contaminated soil. *Electrochim. Acta*, 181:31–38, 2015.

[175] C. Davidson and X. Xuan. Effects of stern layer conductance on electrokinetic energy conversion in nanofluidic channels. *Electrophoresis*, 29(5):1125–1130, 2008.

[176] D. Gillespie. High energy conversion efficiency in nanofluidic channels. *Nano Lett.*, 12(3):1410–1416, 2012.

[177] S. Haeberle and R. Zengerle. Microfluidic platforms for lab-on-a-chip applications. *Lab Chip*, 7(9):1094–1110, 2007.

[178] T. Kawamata, M. Yamada, M. Yasuda, and M. Seki. Continuous and precise particle separation by electroosmotic flow control in microfluidic devices. *Electrophoresis*, 29(7):1423–1430, 2008.

[179] B. Luan and A. Aksimentiev. Electro-osmotic screening of the dna charge in a nanopore. *Phys. Rev. E*, 78:021912, 2008.

[180] D. Mark, S. Haeberle, G. Roth, F. von Stetten, and R. Zengerle. Microfluidic lab-on-a-chip platforms: Requirements, characteristics and applications. *Chem. Soc. Rev.*, 39(3):1153–1182, 2010.

[181] T. Nguyen, Y. Xie, L. J. de Vreede, A. van den Berg, and J. C. T. Eijkel. Highly enhanced energy conversion from the streaming current by polymer addition. *Lab Chip*, 13(16):3210–3216, 2013.

[182] D. G. Nieto and V. M. Barragán. A comparative study of the electro-osmotic behavior of cation and anion exchange membranes in alcohol-water media. *Electrochim. Acta*, 154:166–176, 2015.

[183] A. S. Rathore. Theory of electroosmotic flow, retention and separation efficiency in capillary electrochromatography. *Electrophoresis*, 23(22-23):3827–3846, 2002.

[184] Y. Ren and D. Stein. Slip-enhanced electrokinetic energy conversion in nanofluidic channels. *Nanotechnology*, 19(19):195707, 2008.

[185] A. Revil and P. Leroy. Constitutive equations for ionic transport in porous shales. *J. Geophys. Res.*, 109:B03208, 2004.

[186] A. Revil, P. A. Pezard, and P. W. J. Glover. Streaming potential in porous media: 1. theory of the zeta potential. *J. Geophys. Res.*, 104(B9):20021–20031, 1999.

[187] A. Siria, P. Poncharal, A. L. Biance, R. Fulcrand, X. Blase, S. T. Purcell, and L. Bocquet. Giant osmotic energy conversion measured in a single transmembrane boron nitride nanotube. *Nature*, 494:455–458, 2013.

[188] F. H. J. van der Heyden, D. J. Bonthuis, D. Stein, C. Meyer, and C. Dekker. Electrokinetic energy conversion efficiency in nanofluidic channels. *Nano Lett.*, 6(10):2232–2237, 2006.

[189] S. van Dorp, U. F. Keyser, N. H. Dekker, C. Dekker, and S. G. Lemay. Origin of the electrophoretic force on dna in solid-state nanopores. *Nat. Phys.*, 5:347–351, 2009.

[190] J. Yang, F. Lu, L. W. Kostiuk, and D. Y. Kwok. Electrokinetic microchannel battery by means of electrokinetic and microfluidic phenomena. *J. Micromech. Microeng.*, 13(6):963–970, 2003.

[191] A. Angelova, B. Angelov, S. Lesieur, R. Mutafchieva, M. Ollivon, C. Bourgaux, R. Willumeit, and P. Couvreur. Dynamic control of nanofluidic channels in protein drug delivery vehicles. *J. Drug Delivery Sci. Technol.*, 18(1):41–45, 2008.

[192] C. H. Chen and J. G. Santiago. A planar electroosmotic micropump. *J. Microelectromech. Syst.*, 11(6):672–683, 2002.

[193] P. S. Crozier, D. Henderson, R. L. Rowley, and D. D.Busath. Model channel ion currents in NaCl-extended simple point charge water solution with applied-field molecular dynamics. *Biophys. J.*, 81(6):3077–3089, 2001.

[194] C. Dekker. Solid-state nanopores. *Nat. Nanotech.*, 2:209–215, 2007.

[195] M. Eikerling, Y. I. Kharkats, A. A. Kornyshev, and Y. M. Volfkovich. Phenomenological theory of electro-osmotic effect and water management in polymer electrolyte proton-conducting membranes. *J. Electrochem. Soc.*, 145(8):2684, 1998.

[196] K. Leung, S. B. Rempe, and C. D. Lorenz. Salt permeation and exclusion in hydroxylated and functionalized silica pores. *Phys. Rev. Lett.*, 96(9):095504, 2006.

[197] N. Liu, R. A. Assink, and C. J. Brinker. Synthesis and characterization of highly ordered mesoporous thin films with -COOH terminated pore surfaces. *Chem. Commun.*, 3:370–371, 2003.

[198] O. Plümper, A. Botan, C. Los, Y. Liu, A. Malthe-Sørenssen, and B. Jamtveit. Fluid-driven metamorphism of the continental crust governed by nanoscale fluid flow. *Nat. Geosci.*, 10:685–690, 2017.

[199] R. Qiao and N. R. Aluru. Transient analysis of electro-osmotic transport by a reduced-order modelling approach. *Int. J. Numer. Meth. Eng.*, 56:1023–1050, 2003.

[200] R. S. Ramsey and J. M. Ramsey. Generating electrospray from microchip devices using electroosmotic pumping. *Anal. Chem.*, 69(6):1174–1178, 1997.

[201] L. Cheng, P. Fenter, K. L. Nagy, M. L. Schlegel, and N. C. Sturchio. Molecular-scale density oscillations in water adjacent to a mica surface. *Phys. Rev. Lett.*, 87(15):156103, 2001.

[202] K. P. Travis and K. E. Gubbins. Poiseuille flow of lennard-jones fluids in narrow slit pores. *J. Chem. Phys.*, 112(4):1984–1994, 2000.

[203] K. Besteman, M. A. G. Zevenbergen, and S. G. Lemay. Charge inversion by multivalent ions: Dependence on dielectric constant and surface-charge density. *Phys. Rev. E*, 72(6):061501, 2005.

[204] C. C. Fleck and R. R. Netz. Counterion density profiles at charged flexible membranes. *Phys. Rev. Lett.*, 95(12):128101, 2005.

[205] J. B. Freund. Electro-osmosis in a nanometer-scale channel studied by atomistic simulation. *J. Chem. Phys.*, 116(5):2194–2200, 2002.

[206] H. Greberg and R. Kjellander. Charge inversion in electric double layers and effects of different sizes for counterions and coions. *J. Chem. Phys.*, 108(7):2940–2953, 1998.

[207] P. Kékicheff, S. Marčelja, T. J. Senden, and V. E. Shubin. Charge reversal seen in electrical double layer interaction of surfaces immersed in 2:1 calcium electrolyte. *J. Chem. Phys.*, 99:6098, 1993.

[208] R. Qiao and N. R. Aluru. Atypical dependence of electroosmotic transport on surface charge in a single-wall carbon nanotube. *Nano Lett.*, 3(8):1013–1017, 2003.

[209] R. Qiao and N. R. Aluru. Charge inversion and flow reversal in a nanochannel electro-osmotic flow. *Phys. Rev. Lett.*, 92(19):198301, 2004.

[210] R. Qiao and N. R. Aluru. Multiscale simulation of electroosmotic transport using embedding techniques. *Int. J. Multiscale Comput. Eng.*, 2(2):173–188, 2004.

[211] A. R. J. Silalahi, A. H. Boschitsch, R. C. Harris, and M. O. Fenley. Comparing the predictions of the nonlinear poisson-boltzmann equation and the ion size-modified poisson-boltzmann equation for a low-dielectric charged spherical cavity in an aqueous salt solution. *J. Chem. Theory Comput.*, 6(12):3631–3639, 2010.

[212] G. Tresset. Generalized poisson-fermi formalism for investigating size correlation effects with multiple ions. *Phys. Rev. E*, 78(6):061506, 2008.

[213] A. P. Thompson. Nonequilibrium molecular dynamics simulation of electro-osmotic flow in a charged nanopore. *J. Chem. Phys.*, 119(14):7503–7511, 2003.

[214] W. Zhu, S. J. Singer, Z. Zheng, and A. T. Conlisk. Electro-osmotic flow of a model electrolyte. *Phys. Rev. E*, 71(4):041501, 2005.

[215] M. Rezaei, A. R. Azimian, and D. T. Semiromi. The surface charge density effect on the electro-osmotic flow in a nanochannel: a molecular dynamics study. *Heat Mass Transfer*, 51:661–670, 2015.

[216] D. B. Yaakov, D. Andelman, D. Harries, and R. Podgornik. Beyond standard poisson-boltzmann theory: Ion-specific interactions in aqueous solutions. *J. Phys. Condens. Matter*, 21:424106, 2009.

[217] S. Ghosal. Fluid mechanics of electroosmotic flow and its effect on band broadening in capillary electrophoresis. *Electrophoresis*, 25(2):214–228, 2004.

[218] L. Bocquet and E. Charlaix. Nanofluidics, from bulk to interfaces. *Chem. Soc. Rev.*, 39(3):1073–1095, 2010.

[219] J. C. T. Eijkel. Liquid slip in micro- and nanofluidics: Recent research and its possible implications. *Lab Chip*, 7(3):299–301, 2007.

[220] S. Datta and J. N. Choudhary. Effect of hydrodynamic slippage on electroosmotic flow in zeta potential patterned nanochannels. *Fluid Dyn. Res.*, 45(5):055502, 2013.

[221] M. Majumder, N. Chopra, R. Andrews, and B. J. Hinds. Enhanced flow in carbon nanotubes. *Nature*, 438:44, 2005.

[222] O. I. Vinogradova, K. Koynov, A. Best, and F. Feuillebois. Direct measurements of hydrophobic slippage using double-focus fluorescence cross-correlation. *Phys. Rev. Lett.*, 102(11):118302, 2009.

[223] M. C. Audry, A. Piednoir, P. Joseph, and E. Charlaix. Amplification of electroosmotic flows by wall slippage: Direct measurements on OTS-surfaces. *Faraday Discuss.*, 146:113–124, 2010.

[224] C. Cottin-Bizonne, B. Cross, A. Steinberger, and E. Charlaix. Boundary slip on smooth hydrophobic surfaces: Intrinsic effects and possible artifacts. *Phys. Rev. Lett.*, 94(5):056102, 2005.

[225] D. M. Huang, C. Cottin-Bizonne, C. Ybert, and L. Bocquet. Aqueous electrolytes near hydrophobic surfaces: Dynamic effects of ion specificity and hydrodynamic slip. *Langmuir*, 24(4):1442–1450, 2008.

[226] D. M. Huang, C. Sendner, D. Horinek, R. R. Netz, and L. Bocquet. Water slippage versus contact angle: A quasiuniversal relationship. *Phys. Rev. Lett.*, 101(22):226101, 2008.

[227] U. C. Boehnke, T. Remmler, H. Motschmann, S. Wurlitzer, J. Hauwede, and T. Fischer. Partial air wetting on solvophobic surfaces in polar liquids. *J. Colloid Interface Sci.*, 211(2):243–251, 1999.

[228] Y. Zhu and S. Granick. Apparent slip of newtonian fluids past adsorbed polymer layers. *Macromolecules*, 35(12):4658–4663, 2002.

[229] A. Ajdari and L. Bocquet. Giant amplification of interfacially driven transport by hydrodynamic slip: Diffusio-osmosis and beyond. *Phys. Rev. Lett.*, 96(18):186102, 2006.

[230] N. V. Churaev, J. Ralston, I. P. Sergeeva, and V. D. Sobolev. Electrokinetic properties of methylated quartz capillaries. *Adv. Colloid Interface Sci.*, 96(1-3):265–278, 2002.

[231] P. Papadopoulos, X. Deng, D. Vollmer, and H. J. Butt. Electrokinetics on superhydrophobic surfaces. *J. Phys.: Condens. Matter*, 24(46):464110, 2012.

[232] S. Pennathur, J. C. T. Eijkel, and A. van den Berg. Energy conversion in microsystems: is there a role for micro/nanofluidics? *Lab Chip*, 7(10):1234–1237, 2007.

[233] Q. Cao. Hofmeister effect for electrokinetic transport at ordered dna layers. *Microfluid. Nanofluid.*, 20:132, 2016.

[234] R. Hartkamp, B. Siboulet, J. F. Dufrêche, and B. Coasne. Ion-specific adsorption and electroosmosis in charged amorphous porous silica. *Phys. Chem. Chem. Phys.*, 17(38):24683–24695, 2015.

[235] D. M. Huang, C. Cottin-Bizonne, C. Ybert, and L. Bocquet. Ion-specific anomalous electrokinetic effects in hydrophobic nanochannels. *Phys. Rev. Lett.*, 98(17):177801, 2007.

[236] S. Prakash, H. A. Zambrano, M. Fuest, C. Boone, E. R. Kim, N. Vasquez, and A. T. Conlisk. Electrokinetic transport in silica nanochannels with asymmetric surface charge. *Microfluid. Nanofluid.*, 19:1455–1464, 2015.

[237] N. Schwierz, D. Horinek, U. Sivan, and R. R. Netz. Reverse hofmeister series-the rule rather than the exception. *Curr. Opin. Colloid Interface Sci.*, 23:10–18, 2016.

[238] F. H. J. van der Heyden, D. Stein, K. Besteman, S. G. Lemay, and C. Dekker. Charge inversion at high ionic strength studied by streaming currents. *Phys. Rev. Lett.*, 96(22):224502, 2006.

[239] J. Lyklema. Overcharging, charge reversal: Chemistry or physics? *Colloids Surf., A*, 291(1-3):3–12, 2006.

[240] Q. Cao and R. R. Netz. Anomalous electrokinetics at hydrophobic surfaces: Effects of ionspecificity and interfacial water structure. *Electrochim. Acta*, 259:1011–1020, 2018.

[241] D. J. Bonthuis and R. R. Netz. Unraveling the combined effects of dielectric and viscosity profiles on surface capacitance, electro-osmotic mobility, and electric surface conductivity. *Langmuir*, 28(46):16049–16059, 2012.

[242] B. Jelinek, S. D. Felicelli, P. F. Mlakar, and J. F. Peters. Effects of surface charge density and distribution on the nanochannel electro-osmotic flow. *Int. J. Theor. Appl. Multiscale Mech.*, 2(2):165–183, 2011.

[243] N. Giovambattista, P. G. Debenedetti, and P. J. Rossky. Effect of surface polarity on water contact angle and interfacial hydration structure. *J. Phys. Chem. B*, 111(32):9581–9587, 2007.

[244] S. Dewan, V. Carnevale, A. Bankura, A. Eftekhari-Bafrooei, G. Fiorin, M. L. Klein, and E. Borguet. Structure of water at charged interfaces: A molecular dynamics study. *Langmuir*, 30(27):8056–8065, 2014.

[245] S. Nihonyanagi, S. Yamaguchi, and T. Tahara. Direct evidence for orientational flip-flop of water molecules at charged interfaces: A heterodyne-detected vibrational sum frequency generation study. *J. Chem. Phys.*, 130:204704, 2009.

[246] M. Osawa, M. Tsushima, H. Mogami, G. Samjeské, and A. Yamakata. Structure of water at the electrified platinum-water interface: A study by surface-enhanced infrared absorption spectroscopy. *J. Phys. Chem. C*, 112(11):4248–4256, 2008.

[247] V. Ostroverkhov, G. A. Waychunas, and Y. R. Shen. New information on water interfacial structure revealed by phase-sensitive surface spectroscopy. *Phys. Rev. Lett.*, 94(4):046102, 2005.

[248] R. Qiao and N. R. Aluru. Atomistic simulation of KCl transport in charged silicon nanochannels: Interfacial effects. *Colloids Surf., A*, 267(1-3):103–109, 2005.

[249] S. J. Suresh. Disruption of hydrogen bond structure of water near charged electrode surfaces. *J. Chem. Phys.*, 126:204705, 2007.

[250] R. Vácha, S. W. Rick, P. Jungwirth, A. G. F. de Beer, H. B. de Aguiar, J. S. Samson, and S. Roke. The orientation and charge of water at the hydrophobic oil droplet-water interface. *J. Am. Chem. Soc.*, 133(26):10204–10210, 2011.

[251] N. Nath and A. Chilkoti. Creating "Smart"surfaces using stimuli responsive polymers. *AdV. Mater.*, 14(17):1243–1247, 2002.

[252] T. P. Russell. Surface-responsive materials. *Science*, 297(5583):964–967, 2002.

[253] K. A. Mahmoud, B. Mansoor, A. Mansour, and M. Khraisheh. Functional graphene nanosheets: The next generation membranes for water desalination. *Desalination*, 356:208–225, 2015.

[254] S. Chakraborty. Order parameter modeling of fluid dynamics in narrow confinements subjected to hydrophobic interactions. *Phys. Rev. Lett.*, 99(9):094504, 2007.

[255] S. Karakare, A. Kar, A. Kumar, and S. Chakraborty. Patterning nanoscale flow vortices in nanochannels with patterned substrates. *Phys. Rev. E*, 81(1):016324, 2010.

[256] R. Karnik, K. Castelino, C. Duan, and A. Majumder. Diffusion-limited patterning of molecules in nanofluidic channels. *Nano Lett.*, 6(8):1735–1740, 2006.

[257] R. D. Piner, J. Zhu, F. Xu, S. Hong, and C. A. Mirkin. "Dip-Pen"nanolithography. *Science*, 283(5402):661–663, 1999.

[258] A. Bakhshandeh, A. P. dos Santos, A. Diehl, and Y. Levin. Interaction between random heterogeneously charged surfaces in an electrolyte solution. *J. Chem. Phys.*, 142:194707, 2015.

[259] J. M. Dempster and M. O. de la Cruz. Aggregation of heterogeneously charged colloids. *ACS Nano*, 10(6):5909–5915, 2016.

[260] C. C. Fleck and R. R. Netz. Surfaces with quenched and annealed disordered charge distributions. *Eur. Phys. J. E*, 22:261–273, 2007.

[261] S. J. Miklavic, D. Y. C. Chan, L. R. White, and T. W. Healy. Double layer forces between heterogeneous charged surfaces. *J. Phys. Chem.*, 98(36):9022–9032, 1994.

[262] R. Parthasarathy, P. A. Cripe, and J. T. Groves. Electrostatically driven spatial patterns in lipid membrane composition. *Phys. Rev. Lett.*, 95(4):048101, 2005.

[263] M. Sayin and R. Dahint. Formation of charge-nanopatterned templates with flexible geometry via layer by layer deposition of polyelectrolytes for directed self-assembly of gold nanoparticles. *Nanotechnology*, 28(13):135303, 2017.

[264] D. Velegol and P. K. Thwar. Analytical model for the effect of surface charge nonuniformity on colloidal interactions. *Langmuir*, 17(24):7687–7693, 2001.

[265] A. Ajdari. Pumping liquids using asymmetric electrode arrays. *Phys. Rev. E*, 61(1):R45(R), 2000.

[266] R. V. Craster and O. K. Matar. Electrically induced pattern formation in thin leaky dielectric films. *Phys. Fluids*, 17:032104, 2005.

[267] A. González, A. Ramos, N. G. Green, A. Castellanos, and H. Morgan. Fluid flow induced by nonuniform AC electric fields in electrolytes on microelectrodes. II. a linear double-layer analysis. *Phys. Rev. E*, 61(4):4019, 2000.

[268] W. Y. Ng, S. Goh, Y. C. Lam, C. Yang, and I. Rodríguez. Dc-biased ac-electroosmotic and ac-electrothermal flow mixing in microchannels. *Lab Chip*, 9(6):802–809, 2009.

[269] A. Ramos, A. González, A. Castellanos, N. G. Green, and H. Morgan. Pumping of liquids with ac voltages applied to asymmetric pairs of microelectrodes. *Phys. Rev. E*, 67(5):056302, 2003.

[270] E. Schäffer, T. Thurn-Albrecht, T. Russell, and U. Steiner. Electrically induced structure formation and pattern transfer. *Nature*, 403:874–877, 2000.

[271] O. Schnitzer and E. Yariv. Induced-charge electro-osmosis beyond weak fields. *Phys. Rev. E*, 86(6):061506, 2012.

[272] T. M. Squires and M. Z. Bazant. Induced-charge electro-osmosis. *J. Fluid Mech.*, 509:217–252, 2004.

[273] J. F. Dufreêhe, V. Marry, N. Malíková, and P. Turq. Molecular hydrodynamics for electro-osmosis in clays: from kubo to smoluchowski. *J. Mol. Liq.*, 118(1-3):145–153, 2005.

[274] T. A. Ho, D. Argyris, D. R. Cole, and A. Striolo. Aqueous NaCl and CsCl solutions confined in crystalline slit-shaped silica nanopores of varying degree of protonation. *Langmuir*, 28(2):1256–1266, 2012.

[275] O. Kroutil, Z. Chval, A. A. Skelton, and M. Předota. Computer simulations of quartz (101)-water interface over a range of ph values. *J. Phys. Chem. C*, 119(17):9274–9286, 2015.

[276] V. Marry, J. F. Dufrêche, M. Jardat, and P. Turq. Equilibrium and electrokinetic phenomena in charged porous media from microscopic and mesoscopic models: Electro-osmosis in montmorillonite. *Mol. Phys.*, 101(20):3111–3119, 2003.

[277] M. Předota, M. L. Machesky, and D. J. Wesolowski. Molecular origins of the zeta potential. *Langmuir*, 32(40):10189–10198, 2016.

[278] H. Zhang, A. A. Hassanali, Y. K. Shin, C. Knight, and S. J. Singer. The water-amorphous silica interface: Analysis of the stern layer and surface conduction. *J. Chem. Phys.*, 134:024705, 2011.

[279] S. Park, K. S. Lee, G. Bozoklu, W. Cai, S. B. T. Nguyen, and R. S. Ruoff. Graphene oxide papers modified by divalent ions-enhancing mechanical properties via chemical cross-linking. *ACS Nano*, 2(3):572–578, 2008.

[280] Y. Yang, L. Mu, L. Chen, G. Shi, and H. Fang. Precise control of the interlayer spacing between graphene sheets by hydrated cations. *Phys. Chem. Chem. Phys.*, 21(14):7623–7629, 2019.

[281] J. A. L. Willcox and H. J. Kim. Molecular dynamics study of water flow across multiple layers of pristine, oxidized, and mixed regions of graphene oxide. *ACS Nano*, 11(2):2187–2193, 2017.

[282] F. Perreault, H. Jaramillo, M. Xie, M. Ude, L. D. Nghiem, and M. Elimelech. Biofouling mitigation in forward osmosis using graphene oxide functionalized thin-film composite membranes. *Environ. Sci. Technol.*, 50:5840–5848, 2016.

[283] N. C. Nguyen, S. S. Chen, S. Jain, H. T. Nguyen, S. S. Ray, H. H. Ngo, W. Guo, N. T. Lam, and H. C. Duong. Exploration of an innovative draw solution for a forward osmosis-membrane distillation desalination process. *Environ. Sci. Pollut. Res.*, 25(6):5203–5211, 2018.

[284] A. V. Raghunathan and N. R. Aluru. Molecular understanding of osmosis in semipermeable membranes. *Phys. Rev. Lett.*, 97(024501):1–4, 2006.

[285] J. C. Phillips, R. Braun, W. Wang, J. Gumbart, E. Tajkhorshid, E. Villa, C. Chipot, R. D.Skeel, L. Kalé, and K. Schulten. Scalable molecular dynamics with namd. *J. Comput. Chem.*, 26(16):1781–1802, 2005.

[286] W. L. Jorgensen, J. Chandrasekhar, J. D. Madura, R. W. Impey, and M. L. Klein. Comparison of simple potential functions for simulating liquid water. *J. Chem. Phys.*, 79:926–935, 1983.

[287] S. Miyamoto and P. A. Kollman. Settle: An analytical version of the SHAKE and RATTLE algorithm for rigid water models. *J. Comput. Chem.*, 13:952–962, 1992.

[288] U. Essmann, L. Perera, M. L. Berkowitz, T. Darden, H. Lee, , and L. G. Pedersen. A smooth particle mesh ewald method. *J. Chem. Phys.*, 103(19):8577–8593, 1995.

[289] B. Liu, A. W. K. Law, and K. Zhou. Strained single-layer C_2N membrane for efficient seawater desalination via forward osmosis: A molecular dynamics study. *J. Membr. Sci.*, 550:554–562, 2018.

[290] S. B. Kuila and S. K. Ray. Dehydration of acetic acid by pervaporation using filled ipn membranes. *Sep. Purif. Technol.*, 81:295–306, 2011.

[291] B. C. Roy, M. J. Kabir, and M. S. Rahman. Ternary phase equilibrium data for acetic acid-water-solvent systems and separation of acetic acid from aqueous solution. *J. Appl. Sci.*, 5(4):720–723, 2005.

[292] P. D. Chapman, T. Oliveira, A. G. Livingston, and K. Li. Membranes for the dehydration of solvents by pervaporation. *J. Appl. Sci.*, 318:5–37, 2008.

[293] W. Humphrey, A. Dalke, and K. Schulten. Vmd: Visual molecular dynamics. *J. Mol. Graphics*, 14(1):33–38, 1996.

[294] M. D. Hanwell, D. E. Curtis, D. C. Lonie, T. Vandermeersch, E. Zurek, and G. R. Hutchison. Avogadro: An advanced semantic chemical editor, visualization, and analysis platform. *J. Cheminf.*, 4(17):1–17, 2012.

[295] O. Hod. Graphite and hexagonal boron-nitride have the same interlayer distance. Why? *J. Chem. Theory Comput.*, 8(4):1360–1369, 2012.

[296] A. Gogoi, K. A. Reddy, and P. Mondal. Multilayer graphene oxide membrane in forward osmosis: Molecular insights. *ACS Appl. Nano Mater.*, 1(9):4450–4460, 2018.

[297] A. Achilli, T. Y. Cath, and A. E. Childress. Selection of inorganic-based draw solutions for forward osmosis applications. *J. Membr. Sci.*, 364(1-2):233–241, 2010.

[298] Z. Hu, Y. Chen, and J. Jiang. Zeolitic imidazolate framework-8 as a reverse osmosis membrane for water desalination: Insight from molecular simulation. *J. Chem. Phys.*, 134:134705, 2011.

[299] D. C. Tanugi and J. C. Grossman. Water permeability of nanoporous graphene at realistic pressures for reverse osmosis desalination. *J. Chem. Phys.*, 141:074704, 2014.

[300] X. Davoy, A. Gellé, J. C. Lebreton, H. Tabuteau, A. Soldera, A. Szymczyk, and A. Ghoufı. High water flux with ions sieving in a desalination 2d sub-nanoporous boron nitride material. *ACS Omega*, 3(6):6305–6310, 2018.

[301] K. Li, L. Liu, H. Wu, S. Li, C. Yu, Y. Zhou, W. Huang, and D. Yan. Understanding the temperature effect on transport dynamics and structures in polyamide reverse osmosis system via molecular dynamics simulations. *Phys. Chem. Chem. Phys.*, 20(47):29996–30005, 2018.

[302] M. Kargar, F. K. Varnamkhasti, and A. Lohrasebi. Influence of electric fields on the efficiency of multilayer graphene membrane. *J. Mol. Model.*, 24:241, 2018.

[303] S. Sun, F. Shan, Q. Lyu, C. Li, and S. Hu. Theoretical prediction of mechanical strength and desalination performance of one-atom-thick hydrocarbon polymer in pressure-driven separation. *Polymers*, 11(8):1358, 2019.

[304] T. Yamada and R. Matsuzaki. Effects of slit width on water permeation through graphene membrane by molecular dynamics simulations. *Sci. Rep.*, 8:339, 2018.

[305] Y. Song, F. Xu, M. Wei, and Y. Wang. Water flow inside polamide reverse osmosis membranes: A non-equilibrium molecular dynamics study. *J. Phys. Chem. B*, 121(7):1715–1722, 2017.

[306] M. Shen, S. Keten, and R. M. Lueptow. Dynamics of water and solute transport in polymeric reverse osmosis membranes via molecular dynamics simulations. *J. Membr. Sci.*, 506:95–108, 2016.

[307] B. Roux. The calculation of the potential of mean force using computer simulations. *Comput. Phys. Commun.*, 91(1-2):275–282, 1995.

[308] S. Kumar, J. M. Rosenberg, D. Bouzida, R. H. Swendsen, and P. A. Kollman. Multidimensional free-energy calculations using the weighted histogram analysis method. *J. Comput. Chem.*, 16(11):1339–1350, 1995.

[309] M. W. Mahoney and W. L. Jorgensen. Diffusion constant of the TIP5P model of liquid water. *J. Chem. Phys.*, 114(1):363–366, 2001.

[310] E. Harder, D. E. Walters, Y. D. Bodnar, R. S. Faibish, and B. Roux. Molecular dynamics study of a polymeric reverse osmosis membrane. *J. Phys. Chem. B*, 113(30):10177–10182, 2009.

[311] Y. Luo, E. Harder, R. S. Faibish, and B. Roux. Computer simulations of water flux and salt permeability of the reverse osmosis FT-30 aromatic polyamide membrane. *J. Membr. Sci.*, 384(1-2):1–9, 2011.

[312] T. Wei, L. Zhang, H. Zhao, H. Ma, Md S. J. Sajib, H. Jiang, and S. Murad. Aromatic polyamide reverse-osmosis membrane: An atomistic molecular dynamics simulation. *J. Phys. Chem. B*, 120(39):10311–10318, 2016.

[313] A. P. Côté, A. I. Benin, N. W. Ockwig, M. O'Keeffe, A. J. Matzger, and O. M. Yaghi. Porous, crystalline, covalent organic frameworks. *Science*, 310(5751):1166–1170, 2005.

[314] K. Dey, M. Pal, K. C. Rout, H. S. Kunjattu, A. Das, R. Mukherjee, U. K. Kharul, and R. Banerjee. Selective molecular separation by interfacially crystallized covalent organic framework thin films. *J. Am. Chem. Soc.*, 139(37):13083–13091, 2017.

[315] S. Kandambeth, V. Venkatesh, D. B. Shinde, S. Kumari, A. Halder, S. Verma, and R. Banerjee. Self-templated chemically stable hollow spherical covalent organic framework. *Nat. Commun.*, 6(6786):1–10, 2015.

[316] Z. Kang, Y. Peng, Y. Qian, D. Yuan, M. A. Addicoat, T. Heine, Z. Hu, L. Tee, Z. Guo, and D. Zhao. Mixed matrix membranes (MMMs) comprising exfoliated 2d covalent organic frameworks (COFs) for efficient co$_2$ separation. *Chem. Mater.*, 28(5):1277–1285, 2016.

[317] H. Wang, Z. Zeng, P. Xu, L. Li, G. Zeng, R. Xiao, Z. Tang, D. Huang, L. Tang, C. Lai, D. Jiang, Y. Liu, H. Yi, L. Qin, S. Ye, X. Ren, and W. Tang. Recent progress in covalent organic framework thin films: Fabrications, applications and perspectives. *Chem. Soc. Rev.*, 48(2):488–516, 2019.

[318] R. Wang, X. Shi, A. Xiao, W. Zhou, and Y. Wang. Interfacial polymerization of covalent organic frameworks (COFs) on polymeric substrates for molecular separations. *J. Membr. Sci.*, 566:197–204, 2018.

[319] K. C. Chang, H. I. Lu, M. C. Lai, C. H. Hsu, Y. R. Hsiao, K. Y. Huang, T. L. Chuang, J. M. Yeh, and W. R. Liu. Enhancement of physical properties of electroactive polyimide nanocomposites by addition of graphene nanosheets. *Polym. Int.*, 63(6):1011–1017, 2014.

[320] W. Fei, M. Xue, H. Qiu, and W. Guo. Heterogeneous graphene oxide membrane for rectified ion transport. *Nanoscale*, 11(3):1313–1318, 2019.

[321] R. Han and P. Wu. High-performance graphene oxide nanofiltration membrane with continuous nanochannels prepared by the in situ oxidation of mxene. *J. Mater. Chem. A*, 7(11):6475–6481, 2019.

[322] Z. Li, Z. Liu, H. Sun, and C. Gao. Superstructured assembly of nanocarbons: Fullerenes, nanotubes, and graphene. *Chem. Rev.*, 115(15):7046–7117, 2015.

[323] A. Nicolaï, B. G. Sumpter, and V. Meunier. Tunable water desalination across graphene oxide framework membranes. *Phys. Chem. Chem. Phys.*, 16(18):8646–8654, 2014.

[324] J. Song, H. K. Shon, P. Wang, A. Jang, and I. S. Kim. Tuning the nanostructure of nitrogen-doped graphene laminates for forward osmosis desalination. *Nanoscale*, 11(45):22025–22032, 2019.

[325] B. Sravani, H. Maseed, Y. Chandrasekhar, Y. V. M. Reddy, V. V. S. S. Srikanth, G. Madhavi, and L. S. Sarma. A pt-free graphenaceous composite as an electrocatalyst for efficient oxygen reduction reaction. *Nanoscale*, 11(28):13300–13308, 2019.

[326] L. Valencia, S. Monti, S. Kumar, C. Zhu, P. Liu, S. Yu, and A. P. Mathew. Nanocellulose/graphene oxide layered membranes: Elucidating their behaviour during filtration of water and metal ions in real time. *Nanoscale*, 11(46):22413–22422, 2019.

[327] G. Yang, Z. Xie, M. Cran, D. Ng, C. D. Easton, M. Ding, H. Xu, and S. Gray. Functionalizing graphene oxide framework membranes with sulfonic acid groups for superior aqueous mixture separation. *J. Mater. Chem. A*, 7(34):19682–19690, 2019.

[328] M. Zhang, K. Guan, Y. Ji, G. Liu, W. Jin, and N. Xu. Controllable ion transport by surface-charged graphene oxide membrane. *Nat. Commun.*, 10(1253):1–8, 2019.

[329] W. S. Hung, C. H. Tsou, M. De Guzman, Q. F. An, Y. L. Liu, Y. M. Zhang, C. C. Hu, K. R. Lee, and J. Y. Lai. Cross-linking with diamine monomers to prepare composite graphene oxide-framework membranes with varying d-spacing. *Chem. Mater.*, 26(9):2983–2990, 2014.

[330] J. Kim, L. J. Cote, and J. Huang. Two dimensional soft material: New faces of graphene oxide. *Acc. Chem. Res.*, 45(8):1356–1364, 2012.

[331] C. D. Williams, P. Carbone, and F. R. Siperstein. In silico design and characterization of graphene oxide membranes with variable water content and flake oxygen content. *ACS Nano*, 13(3):2995–3004, 2019.

[332] C. N. Yeh, K. Raidongia, J. Shao, Q. H. Yang, and J. Huang. On the origin of the stability of graphene oxide membranes in water. *Nat. Chem.*, 7:166–170, 2015.

[333] B. Lian, S. De Luca, Y. You, S. Alwarappan, M. Yoshimura, V. Sahajwalla, S. C. Smith, G. Leslie, and R. K. Joshi. Extraordinary water adsorption characteristics of graphene oxide. *Chem. Sci.*, 9(22):5106–5111, 2018.

[334] B. Rezania, N. Severin, A. V. Talyzin, and J. P. Rabe. Hydration of bilayered graphene oxide. *Nano Lett.*, 14(7):3993–3998, 2014.

[335] A. V. Talyzin, T. Hausmaninger, S. You, and T. Szabó. The structure of graphene oxide membranes in liquid water, ethanol and water-ethanol mixtures. *Nanoscale*, 6:272–281, 2014.

[336] A. V. Talyzin, S. M. Luzan, T. Szabó, D. Chernyshev, and V. Dmitriev. Temperature dependent structural breathing of hydrated graphite oxide in H_2O. *Carbon*, 49(6):1894–1899, 2011.

[337] S. You, B. Sundqvist, and A. V. Talyzin. Enormous lattice expansion of hummers graphite oxide in alcohols at low temperatures. *ACS Nano*, 7(2):1395–1399, 2013.

[338] S. You, J. Yu, B. Sundqvist, L. A. Belyaeva, N. V. Avramenko, M. V. Korobov, and A. V. Talyzin. Selective intercalation of graphite oxide by methanol in water/methanol mixtures. *J. Phys. Chem. C*, 117(4):1963–1968, 2013.

[339] Y. Lv, H. C. Yang, H. Q. Liang, L. S. Wan, and Z. K. Xu. Nanofiltration membranes via co-deposition of polydopamine/polyethylenimine followed by cross-linking. *J. Membr. Sci.*, 476:50–58, 2015.

[340] Y. Lv, H. C. Yang, H. Q. Liang, L. S. Wan, and Z. K. Xu. Novel nanofiltration membrane with ultrathin zirconia film as selective layer. *J. Membr. Sci.*, 500:265–271, 2016.

[341] A. Akbari, P. Sheath, S. T. Martin, D. B. Shinde, M. Shaibani, P. C. Banerjee, R. Tkacz, D. Bhattacharyya, and M. Majumder. Large-area graphene-based nanofiltration membranes by shear alignment of discotic nematic liquid crystals of graphene oxide. *Nat. Commun.*, 7(10891):1–12, 2016.

[342] A. M. Gomez, R. C. Silva, H. Muramatsu, J. O. Medina, T. Araki, T. Fukuyo, S. Tejima, K. Takeuchi, T. Hayashi, M. Terrones, and M. Endo. Effective NaCl and dye rejection of hybrid graphene oxide/graphene layered membranes. *Nat. Nanotechnol.*, 12:1083–1088, 2017.

[343] J. Wang, P. Zhang, B. Liang, Y. Liu, T. Xu, L. Wang, B. Cao, and K. Pan. Graphene oxide as an effective barrier on a porous nanofibrous membrane for water treatment. *ACS Appl. Mater. Interfaces*, 8(9):6211–6218, 2016.

[344] Y. Zhang, S. Zhang, and T. S. Chung. Nanometric graphene oxide framework membranes with enhanced heavy metal removal via nanofiltration. *Environ. Sci. Technol.*, 49(16):10235–10242, 2015.

[345] G. Liu, W. Jin, and N. Xu. Graphene-based membranes. *Chem. Soc. Rev.*, 44(15):5016–5030, 2015.

[346] K. Goh, W. Jiang, H. E. Karahan, S. Zhai, L. Wei, D. Yu, A. G. Fane, R. Wang, and Y. Chen. All-carbon nanoarchitectures as high-performance separation membranes with superior stability. *Adv. Funct. Mater.*, 25:7348–7359, 2015.

[347] Z. An, O. C. Compton, K. W. Putz, L. C. Brinson, and S. B. T. Nguyen. Bio-inspired borate cross-linking in ultra-stiff graphene oxide thin films. *Adv. Mater.*, 23(33):3842–3846, 2011.

[348] L. Chen, L. Huang, and J. Zhu. Stitching graphene oxide sheets into a membrane at a liquid/liquid interface. *Chem. Commun.*, 50(100):15944–15947, 2014.

[349] Z. Jia and W. Shi. Tailoring permeation channels of graphene oxide membranes for precise ion separation. *Carbon*, 101:290–295, 2016.

[350] Z. Jia and Y. Wang. Covalently crosslinked graphene oxide membranes by esterification reactions for ions separation. *J. Mater. Chem. A*, 3(8):4405–4412, 2015.

[351] Y. Liu, J. Zhou, E. Zhu, J. Tang, X. Liu, and W. Tang. Covalently intercalated graphene oxide for oil-water separation. *Carbon*, 82:264–272, 2015.

[352] S. Park, D. A. Dikin, S. B. T. Nguyen, and R. S. Ruoff. Graphene oxide sheets chemically cross-linked by polyallylamine. *J. Phys. Chem. C*, 113(36):15801–15804, 2009.

[353] Y. Song, R. Li, F. Pan, Z. He, H. Yang, Y. Li, L. Yang, M. Wang, H. Wang, and Z. Jiang. Ultrapermeable graphene oxide membranes with tunable interlayer distances via vein-like supramolecular dendrimers. *J. Mater. Chem. A*, 7(31):18642–18652, 2019.

[354] Y. Tian, Y. Cao, Y. Wang, W. Yang, and J. Feng. Realizing ultrahigh modulus and high strength of macroscopic graphene oxide papers through crosslinking of mussel-inspired polymers. *Adv.Mater.*, 25(21):2980–2983, 2013.

[355] Y. Han, Y. Jiang, and C. Gao. High-flux graphene oxide nanofiltration membrane intercalated by carbon nanotubes. *ACS Appl. Mater. Interfaces*, 7(15):8147–8155, 2015.

[356] L. Huang, Y. Li, Q. Zhou, W. Yuan, and G. Shi. Graphene oxide membranes with tunable semipermeability in organic solvents. *Adv.Mater.*, 27(25):3797–3802, 2015.

[357] H. Liu, H. Wang, and X. Zhang. Facile fabrication of freestanding ultrathin reduced graphene oxide membranes for water purification. *Adv. Mater.*, 27(2):249–254, 2015.

[358] V. Strauss, M. Muni, A. Borenstein, B. Badamdorj, T. Heil, M. D. Kowal, and R. Kaner. Patching laser-reduced graphene oxide with carbon nanodots. *Nanoscale*, 11(26):12712–12719, 2019.

[359] Z. Zhao, S. Ni, X. Su, Y. Gao, and X. Sun. Thermally reduced graphene oxide membrane with ultrahigh rejection of metal ionsâĂŹ separation from water. *ACS Sustainable Chem. Eng.*, 7(17):14874–14882, 2019.

[360] W. Wu, J. Su, M. Jia, W. Zhong, Z. Li, and W. Li. Ultrastable sandwich graphene oxide hollow fiber membranes with confined interlayer spacing. *J. Mater. Chem. A*, 7(21):13007–13011, 2019.

[361] P. Yu, Z. Xiong, H. Zhan, K. Xie, Y. L. Zhong, G. P. Simon, and D. Li. Electrochemically-derived graphene oxide membranes with high stability and superior ionic sieving. *Chem. Commun.*, 55(28):4075–4078, 2019.

[362] C. Cheng, G. Jiang, C. J. Garvey, Y. Wang, G. P. Simon, J. Z. Liu, and D. Li. Ion transport in complex layered graphene-based membranes with tuneable interlayer spacing. *Sci. Adv.*, 2(2):1–9, 2016.

[363] J. Liu, N. Wang, L. J. Yu, A. Karton, W. Li, W. Zhang, F. Guo, L. Hou, Q. Cheng, L. Jiang, D. A. Weitz, and Y. Zhao. Bioinspired graphene membrane with temperature tunable channels for water gating and molecular separation. *Nat. Commun.*, 8(2011):1–9, 2017.

[364] B. Qi, X. He, G. Zeng, Y. Pan, G. Li, G. Liu, Y. Zhang, W. Chen, and Y. Sun. Strict molecular sieving over electrodeposited 2d-interspacing-narrowed graphene oxide membranes. *Nat. Commun.*, 8(825):1–10, 2017.

[365] P. Sun, Q. Chen, X. Li, H. Liu, K. Wang, M. Zhong, J. Wei, D. Wu, R. Ma, T. Sasaki, and H. Zhu. Highly efficient quasi-static water desalination using monolayer graphene oxide/titania hybrid laminates. *NPG Asia Mater.*, 7(e162):1–8, 2015.

[366] A. V. Talyzin, V. L. Solozhenko, O. O. Kurakevych, T. Szabó, I. Dékány, A. Kurnosov, and V. Dmitriev. Colossal pressure-induced lattice expansion of graphite oxide in the presence of water. *Angew. Chem. Int. Ed.*, 47(43):8268–8271, 2008.

[367] W. Wang, E. Eftekhari, G. Zhu, X. Zhang, Z. Yan, and Q. Li. Graphene oxide membranes with tunable permeability due to embedded carbon dots. *Chem. Commun.*, 50(86):13089–13092, 2014.

[368] W. L. Xu, C. Fang, F. Zhou, Z. Song, Q. Liu, R. Qiao, and M. Yu. Self-assembly: A facile way of forming ultrathin, high-performance graphene oxide membranes for water purification. *Nano Lett.*, 17(5):2928–2933, 2017.

[369] W. Li, W. Wu, and Z. Li. Controlling interlayer spacing of graphene oxide membranes by external pressure regulation. *ACS Nano*, 12(9):9309–9317, 2018.

[370] X. L. Xu, F. W. Lin, Y. Du, X. Zhang, J. Wu, and Z. K. Xu. Graphene oxide nanofiltration membranes stabilized by cationic porphyrin for high salt rejection. *ACS Appl. Mater. Interfaces*, 8(20):12588–12593, 2016.

[371] A. Gogoi, A. Koneru, and K. A. Reddy. Effect of graphene oxide (go) nanosheet sizes, pinhole defects and non-ideal lamellar stacking on the performance of

layered go membranes: An atomistic investigation. *Nanoscale Adv.*, 1(8):3023–3035, 2019.

[372] M. Akhavan, J. Schofield, and S. Jalili. Water transport and desalination through double-layer graphyne membranes. *Phys. Chem. Chem. Phys.*, 20(19):13607–13615, 2018.

[373] V. Prasad K., S. K. Kannam, R. Hartkamp, and S. P. Sathian. Water desalination using graphene nanopores: Influence of the water models used in simulations. *Phys. Chem. Chem. Phys.*, 20(23):16005–16011, 2018.

[374] S. J. Mahdizadeh, E. K. Goharshadi, and G. Akhlamadi. Seawater desalination using pillared graphene as a novel nano-membrane in reverse osmosis process: Nonequilibrium md simulation study. *Phys. Chem. Chem. Phys.*, 20(34):22241–22248, 2018.

[375] Y. G. Yan, W. S. Wang, W. Li, K. P. Loh, and J. Zhang. A graphene-like membrane with an ultrahigh water flux for desalination. *Nanoscale*, 9(47):18951–18958, 2017.

[376] Z. Wang, Q. Tu, S. Zheng, J. J. Urban, S. Li, and B. Mi. Understanding the aqueous stability and filtration capability of MoS_2 membranes. *Nano Lett.*, 17(12):7289–7298, 2017.

[377] E. Guàrdia, J. Martí, L. G. Tarrés, and D. Laria. A molecular dynamics simulation study of hydrogen bonding in aqueous ionic solutions. *J. Mol. Liq.*, 117(1-3):63–67, 2005.

[378] M. Matsumoto and K. E. Gubbins. Hydrogen bonding in liquid methanol. *J. Chem. Phys.*, 93(3):1981–1994, 1990.

[379] J. A. Padró, L. Saiz, and E. Guàrdia. Hydrogen bonding in liquid alcohols: A computer simulation study. *J. Mol. Struct.*, 416(1-3):243–248, 1997.

[380] D. C. Rapaport. Hydrogen bonds in water network organization and lifetimes. *Mol. Phys.*, 50(5):1151–1162, 1983.

[381] R. J. Mashl, S. Joseph, N. R. Aluru, and E. Jakobsson. Anomalously immobilized water: A new water phase induced by confinement in nanotubes. *Nano Lett.*, 3(5):589–592, 2003.

[382] Y. L. Yeh and C. Y. Mou. Orientational relaxation dynamics of liquid water studied by molecular dynamics simulation. *J. Phys. Chem. B*, 103(18):3699–3705, 1999.

[383] S. M. H. H. Amrei, G. H. Miller, and W. D. Ristenpart. Asymmetric rectified electric fields generate flows that can dominate induced-charge electrokinetics. *Phys. Rev. Fluids*, 5(1):013702, 2020.

[384] S. Hardt, J. Hartmann, S. Zhao, and A. Bandopadhyay. Electric-field-induced pattern formation in layers of dna molecules at the interface between two immiscible liquids. *Phys. Rev. Lett.*, 124(6):064501, 2020.

[385] Z. A. Kostiuchenko, J. Z. Cui, and S. G. Lemay. Electrochemistry in micro- and nanochannels controlled by streaming potentials. *J. Phys. Chem. C*, 124(4):2656–2663, 2020.

[386] C. Merlet, D. T. Limmer, M. Salanne, R. van Roij, P. A. Madden, D. Chandler, and B. Rotenberg. The electric double layer has a life of its own. *J. Phys. Chem. C*, 118(32):18291–18298, 2014.

[387] A. H. Sheik, F. Montazersadgh, V. M. Starov, A. Trybala, K. G. U. Wijayantha, and H. C. H. Bandulasena. Electrokinetic transport of a charged dye in a freely suspended liquid film: Experiments and numerical simulations. *Langmuir*, 36(5):1183–1191, 2020.

[388] K. Zhang, Y. Ren, Y. Tao, X. Deng, W. Liu, T. Jiang, and H. Jiang. Efficient particle and droplet manipulation utilizing the combined thermal buoyancy convection and temperature-enhanced rotating induced-charge electroosmotic flow. *Anal. Chim. Acta*, 1096:108–119, 2020.

[389] R. B. Schoch, J. Han, and P. Renaud. Transport phenomena in nanofluidics. *Rev. Mod. Phys.*, 80(3):839–883, 2008.

[390] T. M. Squires and S. R. Quake. Microfluidics: Fluid physics at the nanoliter scale. *Rev. Mod. Phys.*, 77(3):977–1026, 2005.

[391] H. Poppe, A. Cifuentes, and W. Th. Kok. Theoretical description of the influence of external radial fields on the electroosmotic flow in capillary electrophoresis. *Anal. Chem.*, 68(5):888–893, 1996.

[392] M. Rezaei, A. R. Azimian, and A. R. Pishevar. Surface charge-dependent hydrodynamic properties of an electroosmotic slip flow. *Phys. Chem. Chem. Phys.*, 20(48):30365–30375, 2018.

[393] P. A. Cazade, R. Hartkamp, and B. Coasne. Structure and dynamics of an electrolyte confined in charged nanopores. *J. Phys. Chem. C*, 118(10):5061–5072, 2014.

[394] A. T. Celebi, B. Cetin, and A. Beskok. Molecular and continuum perspectives on intermediate and flow reversal regimes in electroosmotic transport. *J. Phys. Chem. C*, 123(22):14024–14035, 2019.

[395] D. Kim and E. Darve. Molecular dynamics simulation of electro-osmotic flows in rough wall nanochannels. *Phys. Rev. E*, 73:051203, 2006.

[396] V. C. Sanchez, A. Jachak, R. H. Hurt, and A. B. Kane. Biological interactions of graphene-family nanomaterials: An interdisciplinary review. *Chem. Res. Toxicol.*, 25(1):15–34, 2012.

[397] H. Zhang, C. Peng, J. Yang, M. Lv, R. Liu, D. He, C. Fan, and Q. Huang. Uniform ultrasmall graphene oxide nanosheets with low cytotoxicity and high cellular uptake. *ACS Appl. Mater. Interfaces*, 5(5):1761–1767, 2013.

[398] W. Hu, C. Peng, W. Luo, M. Lv, X. Li, D. Li, Q. Huang, and C. Fan. Graphene-based antibacterial paper. *ACS Nano*, 4(7):4317–4323, 2010.

[399] M. Lv, Y. Zhang, L. Liang, M. Wei, W. Hu, X. Li, and Q. Huang. Effect of graphene oxide on undifferentiated and retinoic acid-differentiated SH-SY5Y cells line. *Nanoscale*, 4(13):3861–3866, 2012.

List of Publications

International Journal

- A. Gogoi, K. A. Reddy, and P. Mondal. Multilayer graphene oxide membrane in forward osmosis: Molecular insights. *ACS Appl. Nano Mater.*, 1(9):4450âĂŞ4460, 2018.

- A. Gogoi, K. A. Reddy, and P. Mondal. Influence of the presence of cations on the water and salt dynamics inside layered graphene oxide (GO) membranes. *Nanoscale*, 12(13):7273-7283, 2020.

- A. Gogoi, K. A. Reddy, S. Senthilmurugan and P. Mondal. Dehydration of acetic acid using layered graphene oxide (GO) membrane through forward osmosis (FO) process: a molecular dynamics study. *Mol. Simul.*, 0(0):1-9, 2020.

Papers Submitted

- A. Gogoi, K. A. Reddy, and P. Mondal. Electroosmotic Flow through Nanochannel with Patterned Surface Charge Distribution: A Molecular Dynamics Study. *Langmuir*.